

(2)

AFOSR-TR- 85 - 0082



AD-A 150 739

department of chemical engineering and fuel technology

UNIVERSITY OF SHEFFIELD
DTIC FILE COPY

Grant No. AFOSR-84-0011

Fundamental Study of Three Dimensional
Two Phase Flow in Combustion Systems

Final Report 1 Oct. 83 - 30 Sept. 84

S

DTIC
ELECTED
FEB 28 1985
S D
E

Grant No. AFOSR-84-0011

Fundamental Study of Three Dimensional
Two Phase Flow in Combustion Systems

Final Report 1 Oct. 83 - 30 Sept. 84

DTIC
ELECTED
FEB 28 1985
S E D

AIR FORCE OFFICE OF SCIENTIFIC RESEARCH AFOSR
NOTICE OF TRANSMISSION
This technical report was approved for
Distribution outside AFOSR
MATTHEW J. KERPER
Chief, Technical Information Division

Grant Number AFOSR-84-0011

FUNDAMENTAL STUDY OF THREE-DIMENSIONAL TWO PHASE FLOW IN
COMBUSTION SYSTEMS.

Professor J. Swithenbank,
Department of Chemical Engineering
and Fuel Technology,
University of Sheffield,
Sheffield, England.

20 Nov 1984

Final Report 1 Oct 1983 - 30 Sep 1984

Approved for public release;
distribution unlimited.

Prepared for
EOARD/LNB
223/231 Old Marylebone Rd.,
London NW1 5TH, U.K.

and

EUROPEAN OFFICE OF AEROSPACE RESEARCH AND DEVELOPMENT
London, England.

DTIC
COPY
INSPECTED
1

Accession For	
NTIS GRA&I	<input checked="" type="checkbox"/>
DTIC TAB	<input type="checkbox"/>
Unannounced	<input type="checkbox"/>
Justification	
By	
Distribution/	
Availability Codes	
Dist	Avail and/or Special
A-1	

UNCLASSIFIED

SECURITY CLASSIFICATION OF THIS PAGE

REPORT DOCUMENTATION PAGE

1a. REPORT SECURITY CLASSIFICATION U		1b. RESTRICTIVE MARKINGS									
2a. SECURITY CLASSIFICATION AUTHORITY		3. DISTRIBUTION/AVAILABILITY OF REPORT Approved for public release Distribution is unlimited.									
2b. DECLASSIFICATION/DOWNGRADING SCHEDULE											
4. PERFORMING ORGANIZATION REPORT NUMBER(S)		5. MONITORING ORGANIZATION REPORT NUMBER(S) AFOSR-TR. 85-0082									
6a. NAME OF PERFORMING ORGANIZATION Department of Chemical Engineering and Fuel Technology, Sheffield University	6b. OFFICE SYMBOL (if applicable)	7a. NAME OF MONITORING ORGANIZATION <i>Same as #8</i>									
6c. ADDRESS (City, State and ZIP Code) Sheffield, South Yorkshire, S1 3JD, England.		7b. ADDRESS (City, State and ZIP Code) <i>Same as #8</i>									
8a. NAME OF FUNDING/SPONSORING ORGANIZATION Air Force Office of Scientific Research	8b. OFFICE SYMBOL (if applicable) NA	9. PROCUREMENT INSTRUMENT IDENTIFICATION NUMBER AFOSR 84-0011									
8c. ADDRESS (City, State and ZIP Code) <i>Bolling AFB, DC 20332 - 6448</i>		10. SOURCE OF FUNDING NOS. <table border="1"> <tr> <th>PROGRAM ELEMENT NO.</th> <th>PROJECT NO.</th> <th>TASK NO.</th> <th>WORK UNIT NO.</th> </tr> <tr> <td><i>61102F</i></td> <td>2308</td> <td>A2</td> <td></td> </tr> </table>		PROGRAM ELEMENT NO.	PROJECT NO.	TASK NO.	WORK UNIT NO.	<i>61102F</i>	2308	A2	
PROGRAM ELEMENT NO.	PROJECT NO.	TASK NO.	WORK UNIT NO.								
<i>61102F</i>	2308	A2									
11. TITLE (Include Security Classification) Fundamental study of 3-D, Two phase flow in combustion systems.											
12. PERSONAL AUTHOR(S) Professor J. Swithenbank, S.A. Vasquez, P.N. Wild											
13a. TYPE OF REPORT F I N A L	13b. TIME COVERED FROM Oct.83 TO 30 Sept. 84	14. DATE OF REPORT (Yr., Mo., Day) 20 Nov. 1984	15. PAGE COUNT								
16. SUPPLEMENTARY NOTATION F101 Combustor, Combustion Modelling, Turbulence Modelling, Swirling Flow, Particle Sizing. <i>cont'd</i>											
17. COSATI CODES		18. SUBJECT TERMS (Continue on reverse if necessary and identify by block number) Combustion modelling, Droplet sizing, swirling flow, algebraic stress modelling.									
19. ABSTRACT (Continue on reverse if necessary and identify by block number) Combustion systems involve the complex interaction between several fundamental phenomena hence the fundamental aspects of each phenomena cannot be studied in isolation if we wish to understand the whole process. In this investigation, the basic science underlying the interactions between the two-phase flow, fluid dynamics and chemical kinetics have been investigated. The studies have required the development of new diagnostic systems and significant progress has been made in the following areas:- 1. The development of a technique for making accurate dropsize measurements in dense sprays. 2. The application of this technique to an F101 air blast atomizer. 3. The use of LDA for the precise characterization of swirl from the F101 swirler. 4. The development of shear stress mathematical modelling for non-isotropic turbulence. 5. The application of this model to the F101 swirler. 6. The development of a mercury vapour pulse tracer for residence time distribution measurement in combustors. 7. The development of a mathematical modelling technique whereby the residence time distribution can be computed. 8. Closing of the gap between stirred reactor models and finite difference models of combustion systems. 9. Proposal of a new fundamental approach to the problem of simultaneous mixing and reaction using a quantitative coalescence/dispersion eddy concept which has the potential to represent all the high order correlations of the interaction.											
20. DISTRIBUTION/AVAILABILITY OF ABSTRACT UNCLASSIFIED/U/NLIMITED <input checked="" type="checkbox"/> SAME AS RPT. <input type="checkbox"/> DTIC USERS <input type="checkbox"/>		21. ABSTRACT SECURITY CLASSIFICATION Unclassified									
22a. NAME OF RESPONSIBLE INDIVIDUAL Julian M. Tishkoff		22b. TELEPHONE NUMBER (Include Area Code) (202) 767-4935	22c. OFFICE SYMBOL AFOSR/NA								

FUNDAMENTAL STUDY OF THREE-DIMENSIONAL TWO PHASE
FLOW IN COMBUSTION SYSTEMS

Abstract

Combustion systems involve the complex interaction between several fundamental phenomena, hence the fundamental aspects of each phenomena cannot be studied in isolation if we wish to understand the whole process. In this investigation, the basic science underlying the interactions between the two-phase flow, fluid dynamics and chemical kinetics have been investigated. The studies have required the development of new diagnostic systems and significant progress has been made in the following areas:-

- (1) The development of a technique for making accurate dropsize measurements in dense sprays.
- (2) The application of this technique to an F101 air blast atomizer.
- (3) The use of LDA for the precise characterization of swirl from the F101 swirler.
- (4) The development of shear stress mathematical models for non-isotropic turbulence.
- (5) The application of this model to the F101 swirler.
- (6) The development of a mercury vapour pulse tracer for residence time distribution measurement in combustors.
- (7) The development of a mathematical modelling technique whereby the residence time distribution can be computed.
- (8) Closing of the gap between stirred reactor models and finite difference models of combustion systems.
- (9) Proposal of a new fundamental approach to the problem of simultaneous mixing and reaction using a quantitative coalescence/dispersion eddy concept which has the potential to represent all the high order correlations of the interaction. Originator Supplied Keywords include:

STUDY OF THE F101 ANNULAR GAS TURBINE COMBUSTOR.

The object of this study is to apply the Sheffield 3-D flow model to the geometry of the F101 combustion chamber. This work, together with experimental studies carried out on a 54° sector F101 chamber, will provide a useful testing ground for future model development.

To this aim, a calibration rig has been constructed to make inlet condition measurements on the F101 combustor spectacle plate. This has been used to examine the fuel spray droplet size distribution and to study the F101 counter swirling primary air inlet. L.D.A. measurements in the swirling flow have been compared with computer predictions and results are encouraging.

A combustor test facility has been installed to allow cold and hot flow measurements to be made both at atmospheric and elevated pressures. This facility has been used to obtain residence time distribution measurements using a pulsed mercury tracer.

DPA73 (Field 18)

The work is described in detail in the following three reports:

- 1) Fuel spray droplet sizing on the F101 air blast atomizer.
- 2) A study of the F101 combustor swirlers.
- 3) The F101 combustor test facility and Mercury pulse tracer measurements.

Other relevant papers included are

P.G. Felton, A.A. Hamidi and A.K. Aigal "Multiple scattering effects on particle size by laser diffraction".

B.C.R. Ewan, F. Boysan and J. Swithenbank "Closing the gap between finite difference and stirred reactor combustor modelling".

FUEL SPRAY DROPLET SIZING ON THE F101 AIR BLAST ATOMIZER.

Introduction.

Liquid fuel injected into gas turbine combustors is usually atomized by means of a pressure jet or air blast atomizer. The spray produced will consist of droplets with a wide range of diameters. Achieving the correct droplet size distribution over all operating conditions is important in combustor design since it determines the distribution of evaporated fuel in the primary zone. Too fine a droplet will not penetrate far into the air stream and too large a droplet will not evaporate rapidly enough. Earlier work at Sheffield clearly demonstrated the significance of these effects.

The FLUENT code (1) for three dimensional two phase reacting flows is able to calculate the trajectories of individual fuel droplets in a combustor and to simulate their effect on evaporated fuel distribution. It is also able to predict the effect of turbulence on these droplet trajectories. To do this the initial size distribution of the spray is divided into a number of discrete intervals each representing an average diameter. The equations for motion, heating up and evaporation are then solved for droplets representing each size group.

It is desired to model the F101 combustor using the FLUENT code and so the fuel droplet size distribution, produced by its air blast atomizer, must be determined. This report described how this is achieved using a Malvern particle sizing instrument.

The Malvern Particle Sizer, Operating Theory.

The Malvern particle sizer provides a non-intrusive optical technique for particle sizing. The optical configuration is shown in figure 5. A parallel beam of monochromatic coherent light, produced by a 1 mW He/Ne laser and beam expander, is passed through the field of droplets or particles to be measured. When a spherical particle is illuminated in this manner a Fraunhofer diffraction pattern is formed. If the particle is arranged to be within the focal length of a Fourier transform lens then undiffracted light is focused to a point on the optical axis and diffracted light forms a far field Fraunhofer pattern of rings around the central point. The diffraction pattern formed by a single particle or a field of monosized particles is shown in figure 6. The pattern will be stationary, independent of whether the particles are in motion, since light is diffracted at an angle dependent only on particle size and will give the same radial displacement in the focal plane irrespective of particle position in the illuminating beam.

For a monosized field of particles, of size a , the light energy contained within a circle, radius s , in the focal plane is given by

$$L = 1 - J_0^2 \left[\frac{2\pi a s}{\lambda F} \right] - J_1^2 \left[\frac{2\pi a s}{\lambda F} \right] \quad (1)$$

The light energy within any ring, in the focal plane, bounded by radii s_1 and s_2 is therefore given by

$$L s_1 s_2 = E [J_0^2(Kas_2/F) + J_1^2(Kas_2/F) - J_1^2(Kas_1/F) - J_0^2(Kas_1/F)] \quad (2)$$

where

$$K = 2\pi/\lambda \quad (3)$$

E is the energy incident on the particles and is proportional to their cross sectional area and their number.

$$E = C_1 \pi a^2 N \quad (4)$$

C_1 is a constant dependent on laser power and N is the number of particles, given by

$$N = 3W/4\pi a^3 \rho \quad (5)$$

Hence

$$E = C_2 W/q \quad (6)$$

If a range of particle sizes are present then the light energy, falling onto any ring in the focal plane, is the sum of the contributions from all particles.

$$L s_1 s_2 = C_2 \sum_{i=1}^m \frac{w_i}{a_i} \left[J_0^2 \left(\frac{Ka_i}{F} s_1 \right) + J_1^2 \left(\frac{Ka_i}{F} s_1 \right) - J_0^2 \left(\frac{Ka_i}{F} s_2 \right) - J_1^2 \left(\frac{Ka_i}{F} s_2 \right) \right] \quad (7)$$

The particle size distribution is classified into a number of size ranges and incident light energy is measured by means of concentric photo-detector rings placed in the focal plane. Measurements are made at radii where s is related to a_i , the mean size of the i th size range, by

$$2\pi a_i / \lambda F = 1.357 \quad (8)$$

Equation (8) is the condition for the first maximum in the diffracted energy distribution.

The total energy distribution is the sum of the products of the energy distributions for each size range and the weight fraction of particles in that range. In matrix form

$$L(I) = W(J) T(I, J) \quad (9)$$

Where $L(I)$ is the light energy falling on ring I ; $W(J)$ is the weight fraction in size range J and $T(I,J)$ contains the coefficients which define the light energy distribution for each particle size range.

A weight distribution, $W(J)$, is fitted to the measured distribution of light energy by an iterative procedure such that the error

$$\sum (L(I) - W(J)T(I,J))^2 \quad (10)$$

is minimized.

This analysis is carried out by a dedicated CBM microcomputer. The system allows any of a number of different size distribution functions to be fitted to the measured energy distribution. These include Rosin Rammller and log normal distribution as well as a model independent option.

For fuel spray studies the Rosin Rammller distribution is often employed as this has been found to fit spray size distributions particularly well.

The distribution is defined by

$$Y = 10 s (1-\text{Exp}(-x/\bar{x}))^N \quad (11)$$

Y = % of particles with diameter less than x .

\bar{x} = Rosin Rammller mean diameter.

N = Rosin Rammller exponent which measures the spread of the distribution about the mean \bar{x} .

The difference between the light intensity measured at the centre of the photodetector, before and after particles are placed in the beam gives the fraction of light obscured (or the obscuration). This is related to the total projected area of the particles by the Beer Lambert law

$$\ln \left(\frac{I}{I_0} \right) = -\zeta l \quad (12)$$

$$\zeta = 2 \sum_{i=1}^m N_i A_i \quad (13)$$

and allows determination of particle concentration.

Limitations of the Malvern Sizing Instrument.

The instrument is capable of measuring particle size down to one micron. Smaller particles cannot be measured since the light scatterers must be larger than the wavelength of light ($0.6238 \mu\text{m}$ for a He/Ne laser).

All the particles must be within the focal length of the Fourier transform lens. Fine particles which are too far from the lens will scatter light which is not focused onto the photodetectors and results will be biased towards large particles.

Reliable results can only be obtained if the light obscuration is in the range 5 to 50%. Low obscuration means that a representative sample of particles is not analysed while at obscurations over 50% multiple scattering of light becomes significant and biases results towards small particles. Hamidi and Felton (2) have recently developed a model for the latter effect which allows corrections for multiple scattering to be made.

The F101 Fuel Injector.

Figure 1(a) shows the F101 CED fuel injector nozzle. Fuel enters through four ports in the nozzle and annular openings around these surround the fuel with high velocity air. The nozzles are mounted in the spectacle plate shown in figure 1(b). Fuel from each nozzle is carried into the combustor primary zone by air from two concentric counter swirling inlets in the spectacle plate.

Sizing Experiment.

The apparatus used for this is illustrated in figure 2. Measurements cannot be made inside the combustor since geometry limits access. The spectacle plate was therefore removed and mounted on a milling machine table as shown in the figure. This provides a rigid support and also allows accurate movement of the plate in three dimensions.

Fuel and air were supplied to a single atomizer nozzle. Air was also supplied to the associated swirlers and splash plate, since it was thought that these flows might influence atomization.

Air Supply.

Air was supplied using a Metrico centrifugal fan (capable of providing up to 1299 CFM at a pressure of 2 psi). The flow rate was regulated using a sliding gate valve. Since air was fed to the nozzle assembly through a curved plastic hose, honeycomb metal flow straighteners were employed upstream of the spectacle plate inlet.

The flow rate was measured by means of an orifice plate, with corner tappings. Static pressure was measured using a mercury manometer and differential pressure using an inclined spirit manometer. Air temperature was recorded using a sheathed chromel-alumel thermocouple and an RS AD595AD thermocouple amplifier and cold junction compensator. The accuracy of flow measurement was estimated to be $\pm 2\%$.

Fuel Supply.

Fuel was supplied from a steel pressure vessel pressurised using a nitrogen cylinder. The flow rate was measured using a rotameter with an accuracy estimated to be 0.005 L/min.

Fuel Extraction.

Spray droplets were collected in a drum and fumes were extracted from this by means of a Coanda ejector supplied with compressed air.

Sizing Instrument.

The sizing instrument transmitter and detector were mounted on optical trestles either side of the fuel nozzle and were aligned as described in the Malvern particle sizer manual (3).

A 300 mm collecting lens was employed.

Results.

Size distributions were measured through the centre of the spray at two stations downstream of the injector.

The measured distributions of light energy were fitted with Rosin Rammler size distributions. Results for a range of fuel and air flow rates are shown in figures 3 and 4 and in table 1.

Nomenclature.

- a Radius of particle.
- a_i Mean particle radius in ith size range.
- A_i Cross sectional area of particles in the size range.
- E Light energy incident on particle.
- F Focal length of Fourier transform lens.
- I Light intensity with particles in beam.
- I_o Light intensity without particles in beam.
- J_0 Zero order Bessel Function.
- J_1 First order Bessel Function.
- λ Optical path length.
- m Number of size ranges.
- N Number of particles.
- N_i Number of particles in size range.
- w Weight of particles radius a.
- λ Wave length of light.
- ρ Particle density.

References

- (1) W.H. Ayers, F. Boysan and J. Swithenbank "Droplet trajectories in three dimensional gas turbine flow fields". University of Sheffield, Department of Chemical Engineering and Fuel Technology Report HIC 355, 1980.
- (2) P.G. Felton, A.A. Manidi and A.K. Aigal "Multiple scattering effects on particle sizing by laser diffraction". University of Sheffield Department of Chemical Engineering and Fuel Technology report HIC 431, 1984.
- (3) 2600/3600 Particle Sizer Handbook, version 2.0. Malvern Instruments Ltd., Malvern, England.

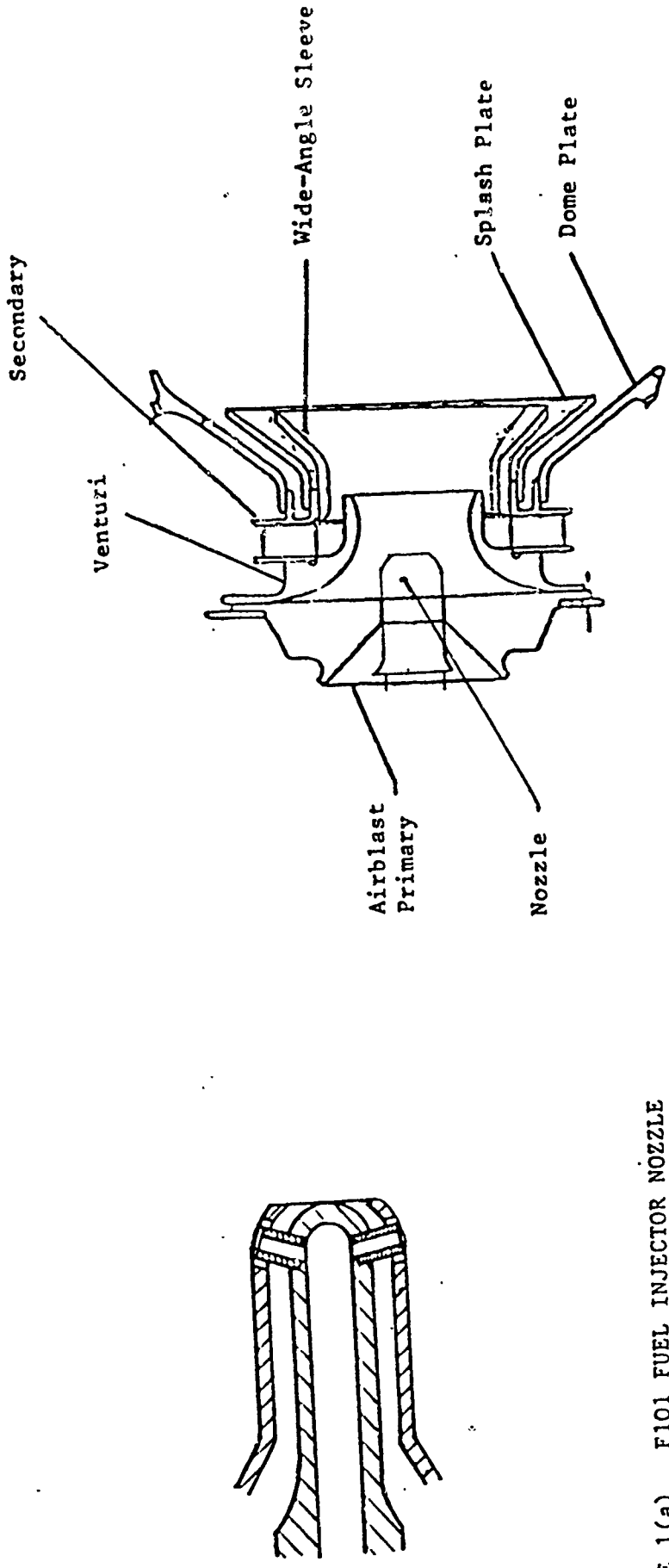


FIGURE 1(a) F101 FUEL INJECTOR NOZZLE

FIGURE 1(b) F101 SPECTACLE PLATE AND SWIRLER ASSEMBLY

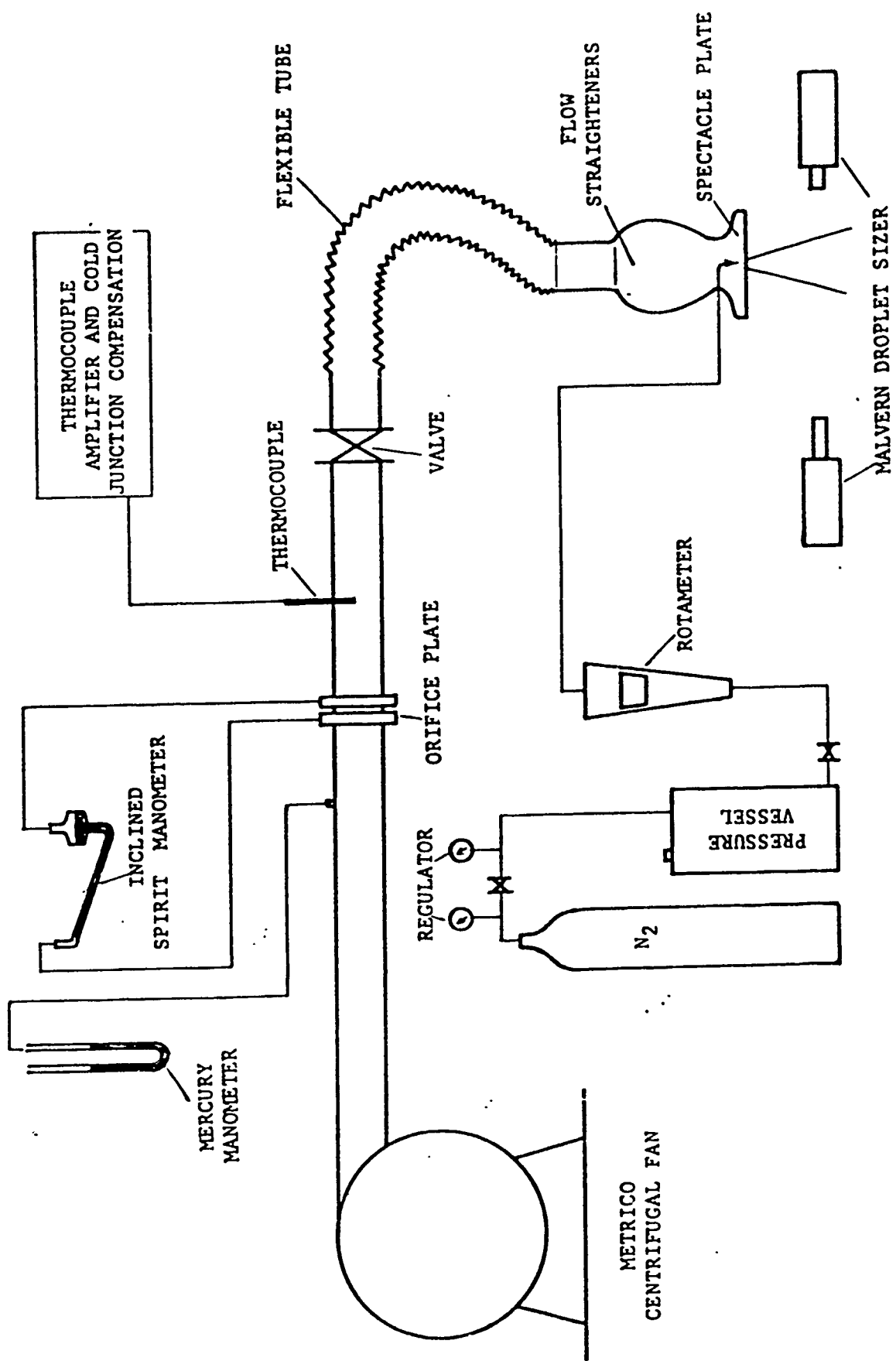


FIGURE 2 F101 INLET CALIBRATION APPARATUS

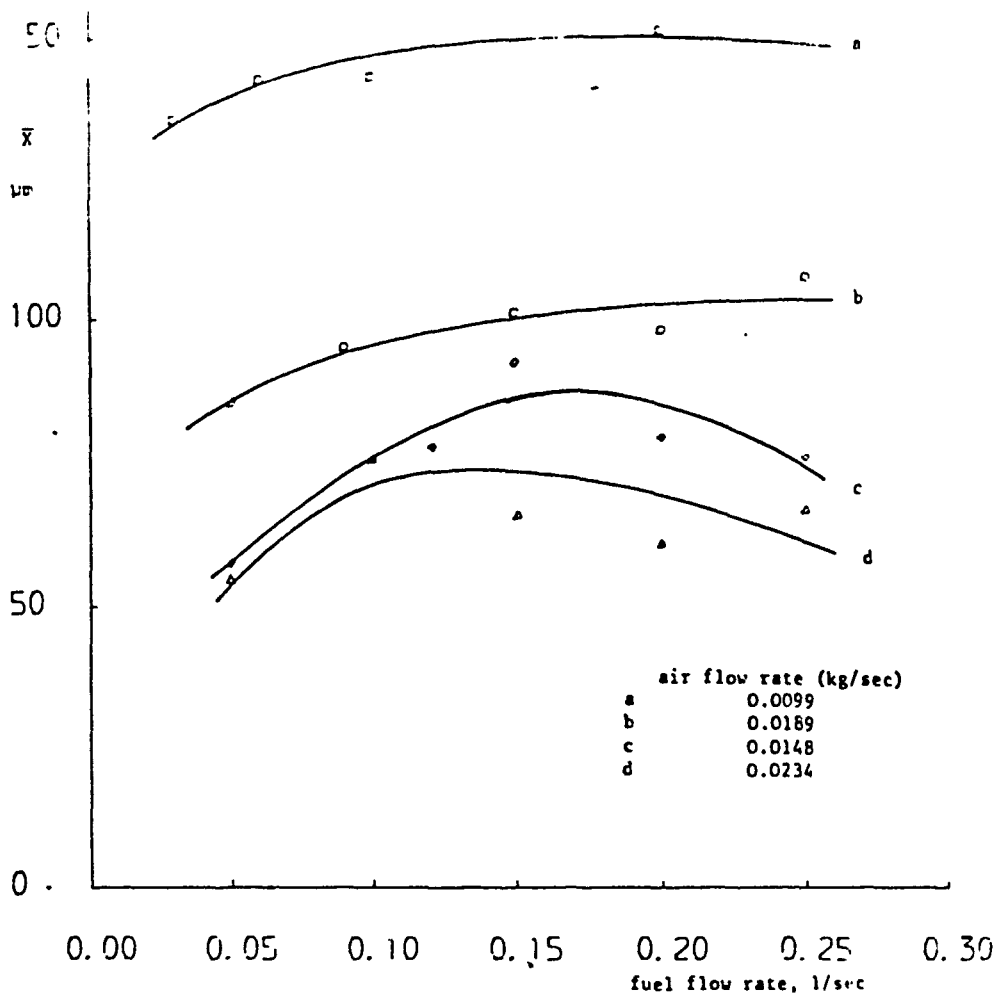
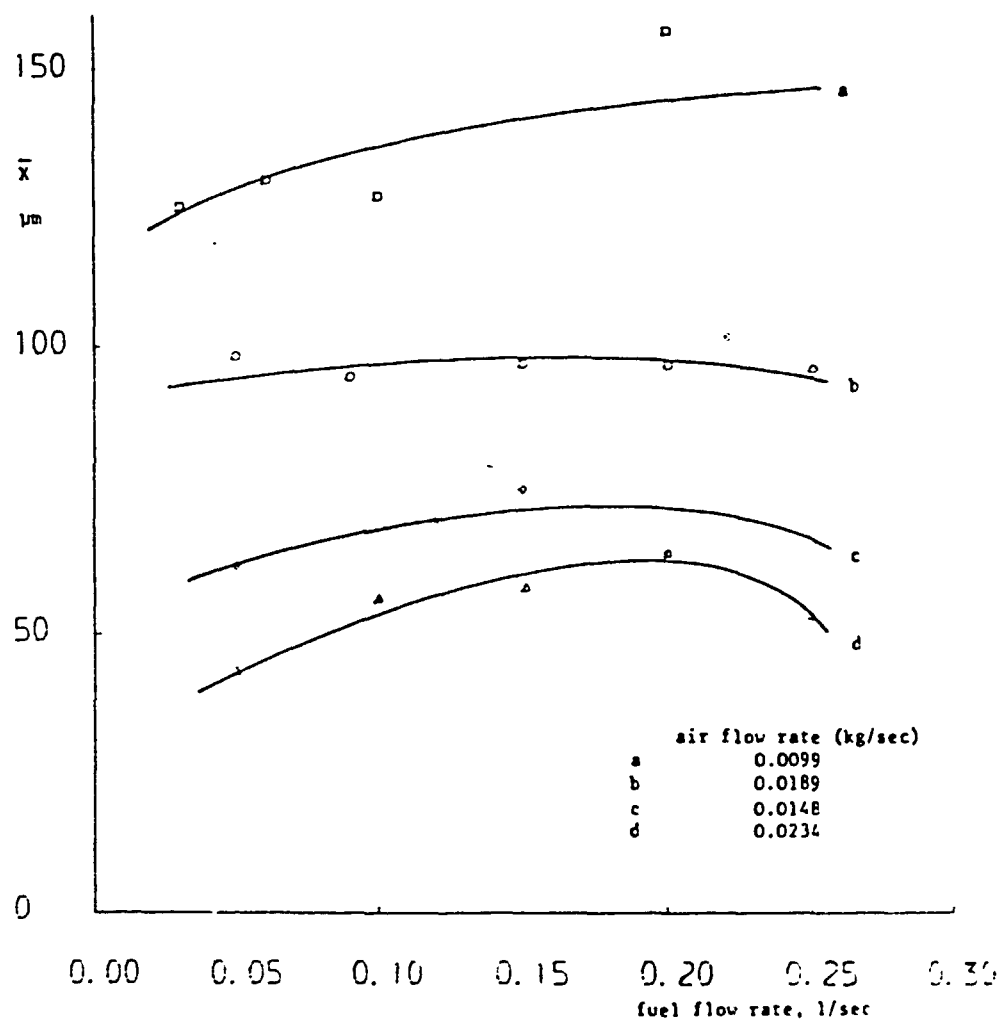


FIGURE 3 GRAPH OF \bar{x} AGAINST FUEL FLOW RATE (RECORDED 10cm DOWN STREAM OF INJECTOR)



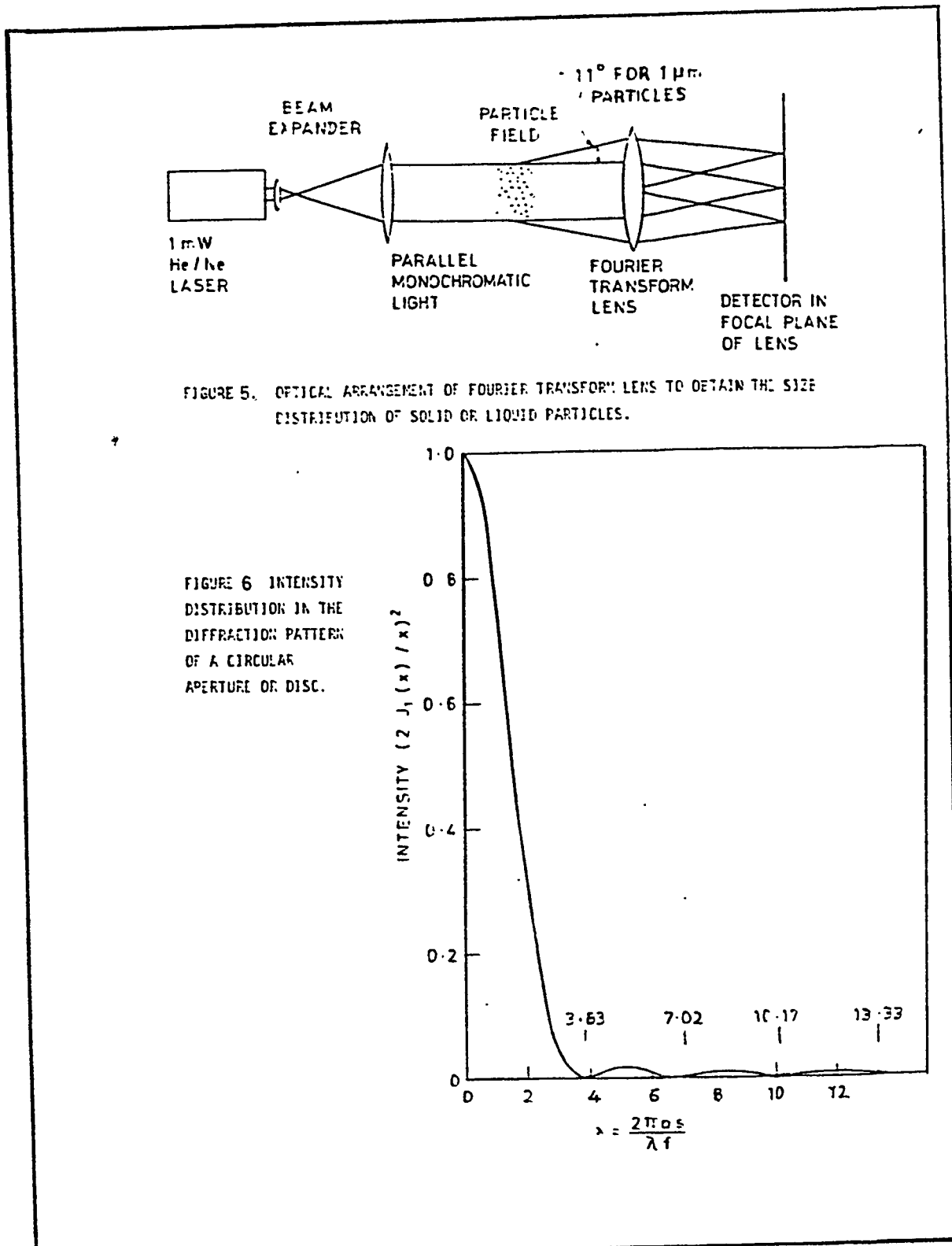


TABLE 1 DROPLET SIZE DISTRIBUTION

air flow rate kg/sec	fuel flow rate l/sec	d=10cm		d=20cm	
		\bar{X}	N	\bar{X}	N
0.0099	0.03	135.71	2.47	124.89	2.53
	0.0604	142.77	2.41	129.81	2.36
	0.10	143.42	2.39	126.85	2.42
	0.20	151.51	2.23	156.77	2.28
0.0148	0.05	85.46	2.42	98.32	2.42
	0.09	95.07	2.30	94.68	2.41
	0.15	101.31	2.31	96.89	2.35
	0.20	98.03	2.25	96.52	2.35
	0.25	107.46*	2.20	95.75	2.30
0.0189	0.05	57.86	2.42	62.21	2.60
	0.121	77.62	2.30	70.20	2.48
	0.15	92.43*	2.14	75.31	2.36
	0.20	79.30*	2.36	64.23	2.60
	0.25	75.77*	2.25	67.12	2.36
0.0234	0.05	54.98	2.46	43.38	2.94
	0.10	75.65	2.30	56.44	2.60
	0.151	66.12*	2.48	58.34*	2.60
	0.20	61.19*	2.53	64.29*	2.36
	0.25	67.01*	2.36	53.13*	2.56

d---- distance down stream of injector

*--- corrected for high obscuration

A STUDY OF F101 COUNTER SWIRLING INLET.

Introduction.

When rotating motion is imparted to a fluid upstream of an orifice, then the flow leaves the orifice with tangential as well as axial and radial velocity components. The presence of this swirl sets up an axial pressure gradient which causes reverse flow along the axis and a recirculation zone is formed. In a combustion chamber this is used to stabilise combustion in the primary zone. The ability to predict this phenomenon will be most important for accurate combustor modelling.

The object of this work was to make LDA measurements of velocity close to the exit of F101 swirlers and to demonstrate the ability of the FLUENT code (1) to predict these results.

The F101 Swirlers.

The spectacle plate and two stage counter rotating swirler assembly are illustrated in figure 1. A portion of the primary air flows through the swirlers. These comprise a primary swirler of eight tangential slots and a secondary guide van cascade. The remainder of the primary air enters through perforations in the structure to provide impingement cooling of the splash plates and hot side film cooling for the dome structure.

Experimental Measurements.

The calibration rig described in the previous report (2) was again used for this work and the LDA system is illustrated in figure 2. The latter employed an 800 mW argon laser operated in the fundamental TEM mode. Light is focused onto a rotating diffraction grating which serves as a beam splitter and provides the frequency shifting required for making measurements in the highly turbulent swirling flow. A mask blocks off all but the +1 and -1 order diffracted beams which are brought to focus at the measurement point in front of the F101 spectacle plate. The rotating grating is driven by a servo motor and its speed is monitored by means of an infra red transmitter and detector.

Detector System.

An 85-200 mm zoom lens was employed to focus scattered light from the measurement volume into a Malvern Instruments photomultiplier assembly which incorporates a pinhole, interference filter, EMI 9502B photomultiplier, amplifier and discriminator.

Clipped autocorrelation of the signal was carried out using a Malvern K7023 digital correlator and correlator store. This is a 1 bit clipping correlator and is described fully in reference (3). The device has 48 channels for storing the correlogram. Sample times down to 0.05 micro seconds can be used and these run consecutively with no dead time between.

The correlator was operated under control from a Malvern MDP7023V computing data processor. This is essentially a microcomputer running the Malvern fringes mode velocity and turbulence algorithm (3). Data stored in the correlator can be downloaded to the computer where it is processed to give values of velocity and turbulence.

Velocity Calculation.

The probability distribution of velocity in the turbulent flow is assumed Gaussian with variance σ^2 . The method employed to calculate the mean velocity, \bar{u} , and percentage turbulence

$$\eta = (\sigma/\bar{u}) \times 100\% \quad (1)$$

is that of differentiating the analytical expression for the photon correlation function and solving for the first three turning points in the correlogram. This yields:

$$\eta = \frac{1}{\pi} \sqrt{\frac{\frac{1}{2}(R-1) + \frac{1}{8n^2}}{}} \quad (2)$$

$$R = (g_2 - g_1)/(g_2 - g_3) \quad (3)$$

$$v_o = s/[\zeta(t_1 + t_2 + t_3)^{\frac{1}{3}}] \quad (4)$$

$$v_c = \left[1 - \eta^2 - \frac{1}{m^2 n^2 \pi^2} \left(1 + \frac{m^2}{2} \right) \right] \quad (5)$$

$$v_t = v_o \times v_c \quad (6)$$

$$m = (2c)/(a+b) \quad (7)$$

$$a = g_1 - FP \quad (8)$$

$$b = g_2 - FP \quad (9)$$

$$c = g_2 - g_1 \quad (10)$$

where

m = effective fringe visibility

τ = sample time

s = fringe spacing

n = number of fringes in beam radius.

The meaning of t_i and g_i are apparent from figure 8.

Gas velocity is then given by

$$(\text{gas velocity}) = V_t \pm C \times (\text{grating speed})$$

where C is a constant dependent on the diffraction grating line spacing.

Computer modelling.

The FLUENT code (1) was used to model the counter swirling flow. The boundary conditions employed are shown in tables 1, 2 and 3. The finite difference grid is shown in figure 7(a). The inlet velocity components were calculated from the combustor geometry and the known air flow rate using the swirling flow theory of Beér and Chigier (4).

Modelling was carried out using both the $K\epsilon$ model for turbulence and the algebraic stress model.

The predicted axial and tangential velocity components, at a station 25 mm downstream of the primary inlet, were compared with the LDA measurements.

Results.

Figures 3, 4, 5 and 6 compare the predicted axial and tangential velocity components with measured values. It can be seen that using the algebraic stress model for turbulence gives a considerable improvement in the predicted flow field.

Conclusion.

LDA measurements have been made at the exit of an F101 counter swirling air inlet. The swirlers have also been modelled, using the FLUENT finite difference code, with $K\epsilon$ and algebraic stress models for turbulence. From comparison of predicted and measured velocities it is concluded that an algebraic stress model for turbulence gives a considerable improvement over the $K\epsilon$ model.

Nomenclature.

- u axial velocity (m/s).
- v radial velocity (m/s).
- w tangential velocity (m/s).
- W₀ denotes wall cell.
- I denotes inlet.
- O denotes outlet.
- S denotes symmetry cell.
- denotes live cell.

References.

- (1) FLUENT Manual, Creare engineering research and development, computer systems and software.
- (2) Fuel spray droplet sizing on the F101 air blast atomizer. This Document.
- (3) K7023 digital correlator Manual. Malvern Instruments, Malvern, England.
- (4) J.M. Beér and N.A. Chigier, Combustion Aerodynamics, Applied Science Publishers, London.

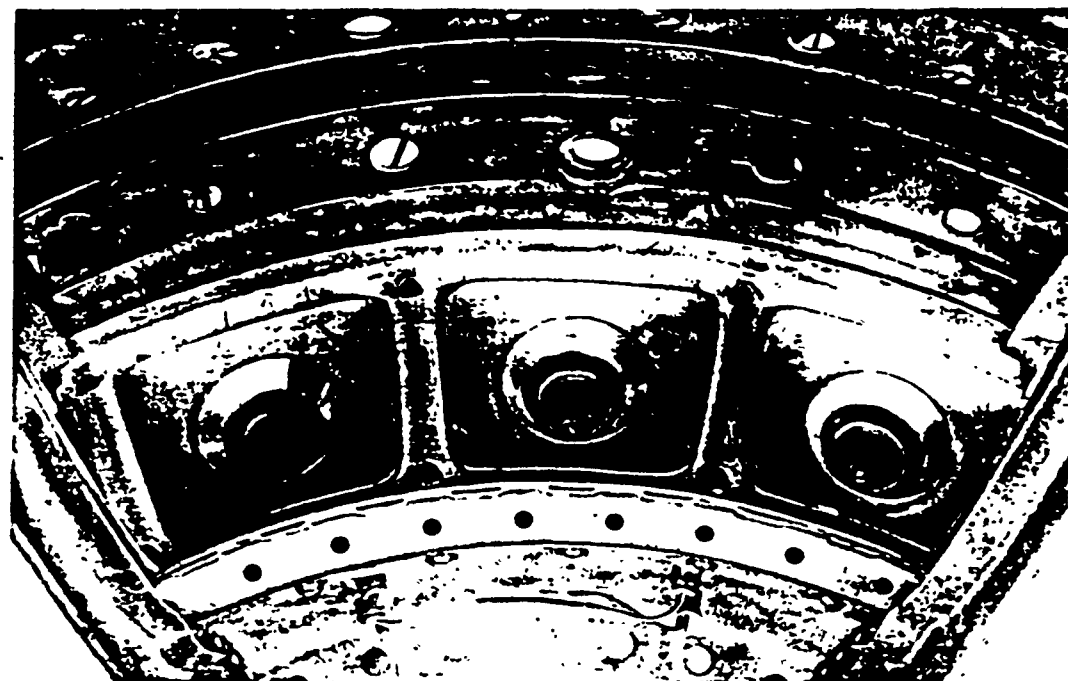
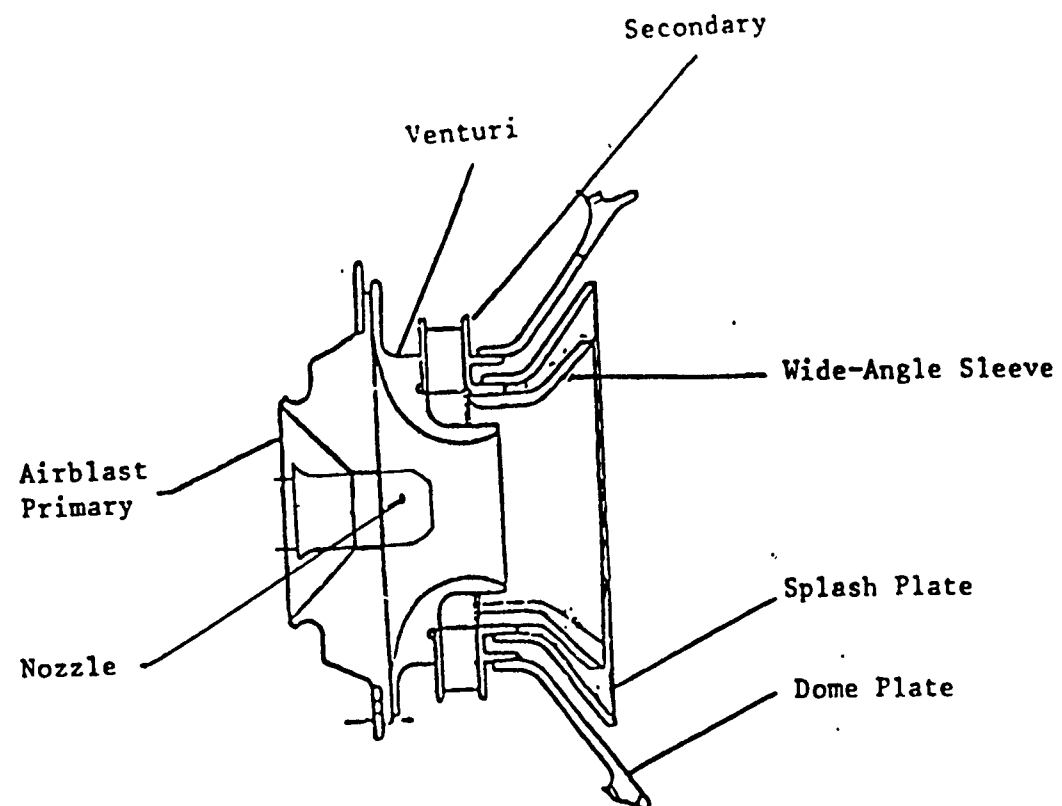


FIGURE 1 F101 SPECTACLE PLATE AND SWIRLER ASSEMBLY

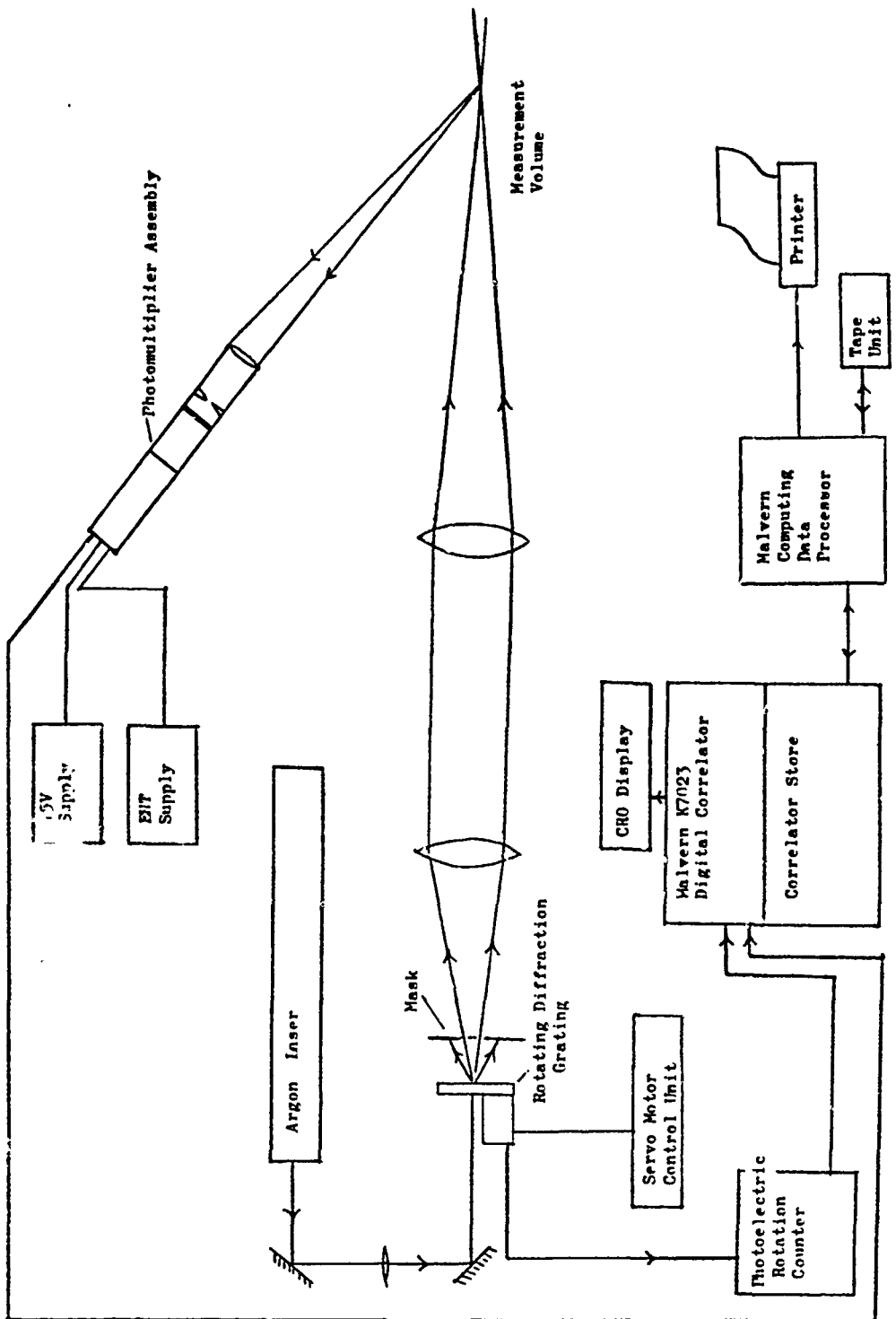


FIGURE 2 L.D.A. SYSTEM

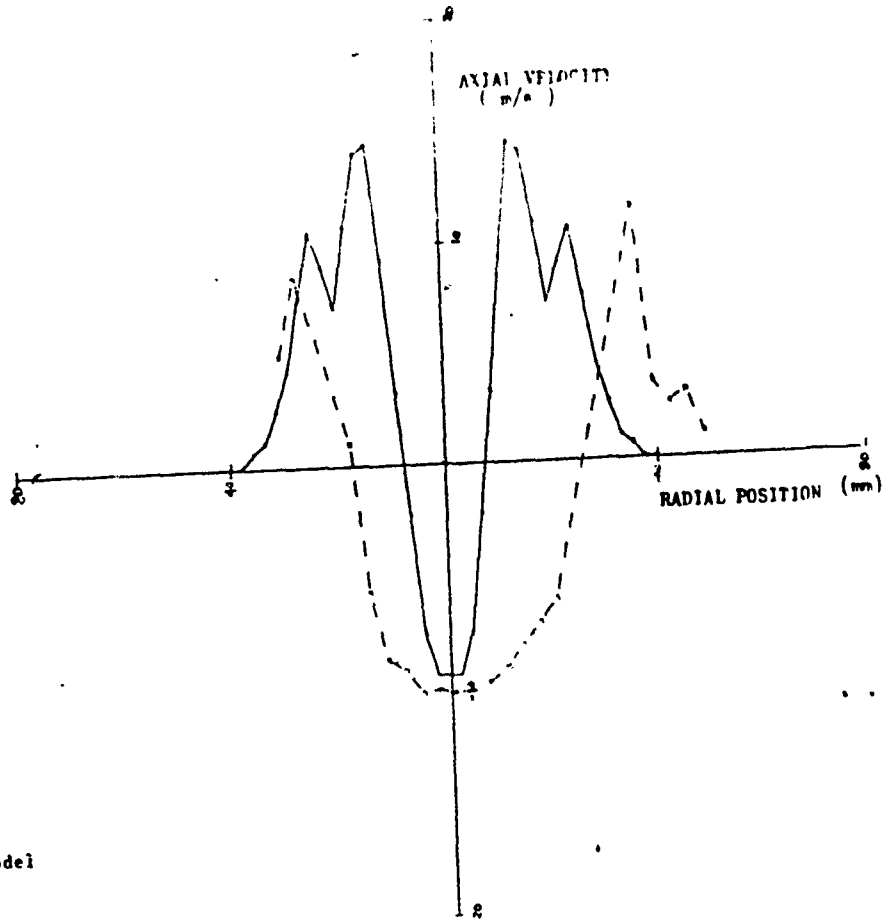


FIGURE 3
AXIAL VELOCITY PROFILE

□ LDA measurements
○ modelling with K-E model

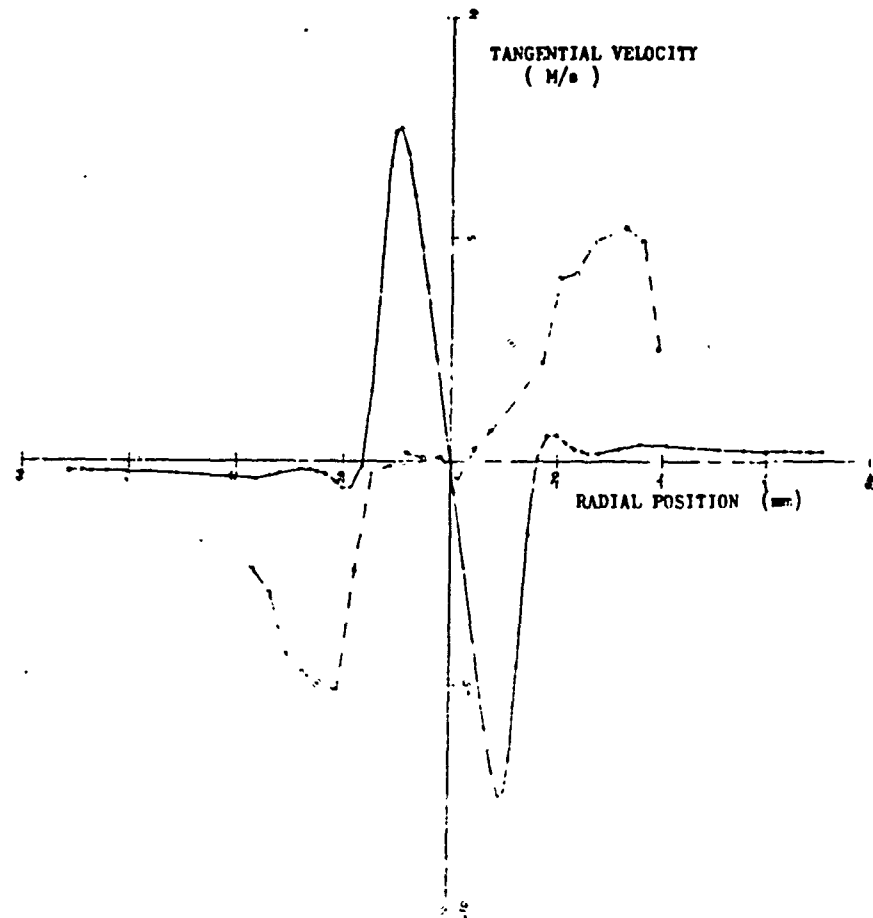
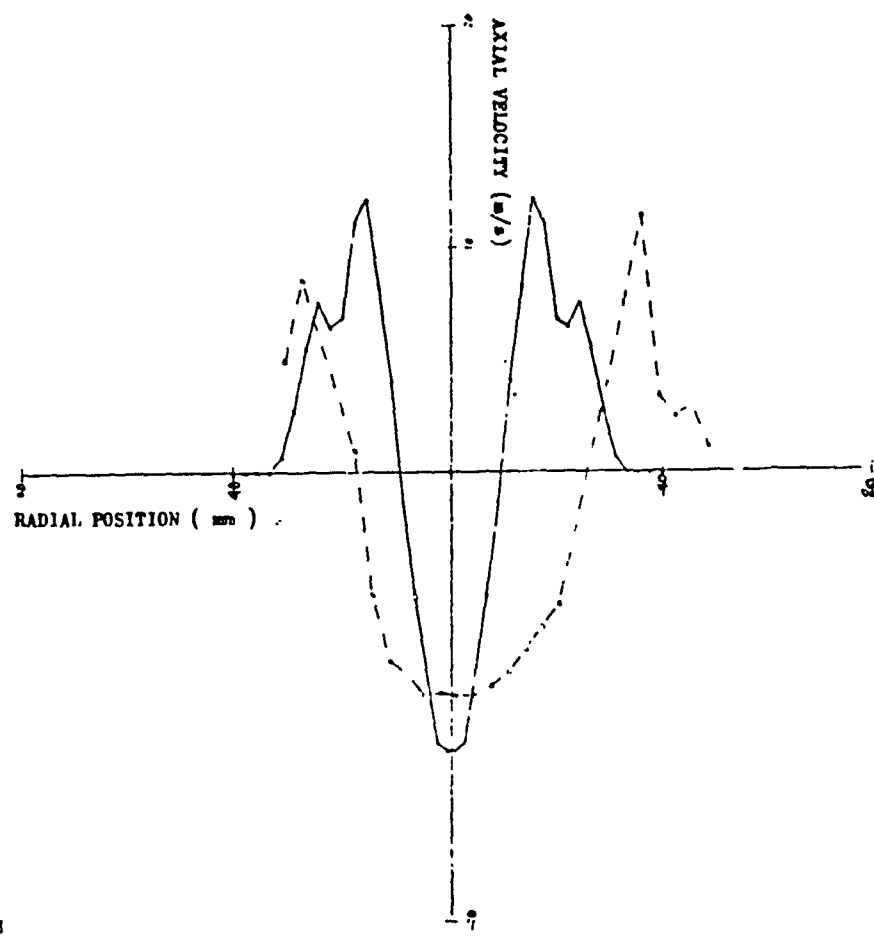
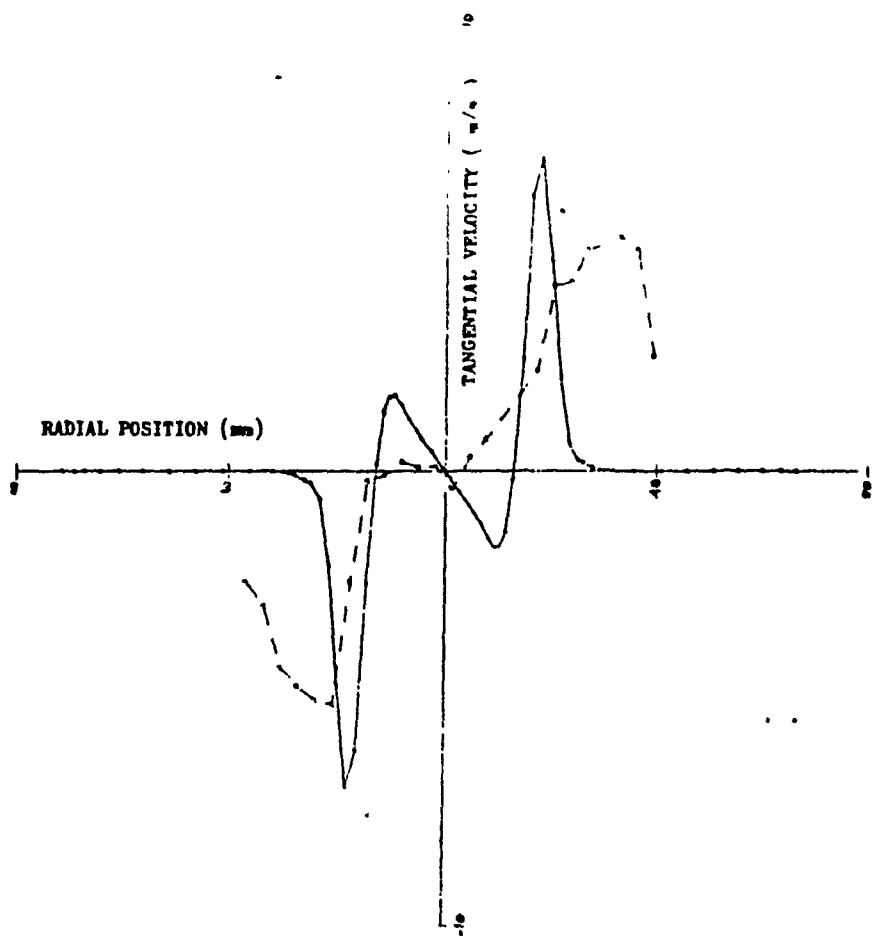
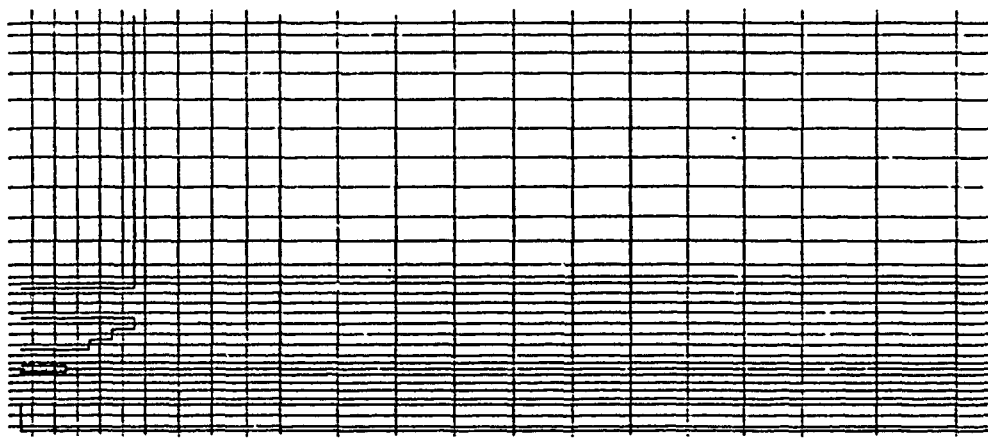


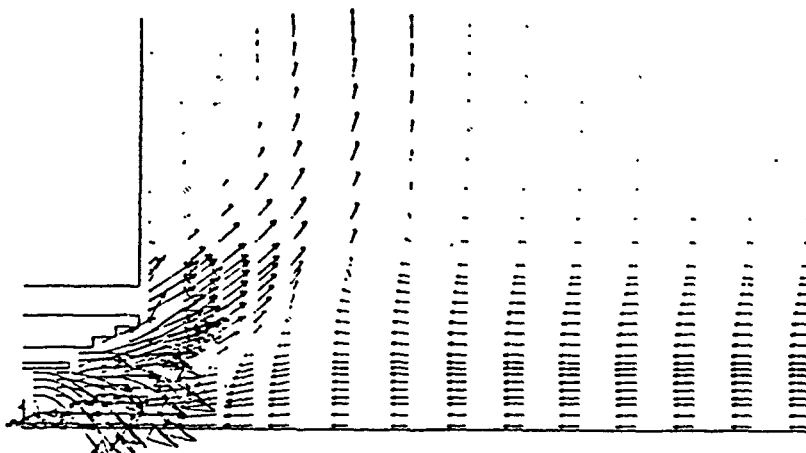
FIGURE 4
TANGENTIAL VELOCITY PROFILE

□ LDA measurements
○ modelling with K-E model





(A) FINITE DIFFERENCE GRID



(B)
VELOCITY VECTORS PREDICTED USING K & TURBULENCE MODEL

FIGURE 7

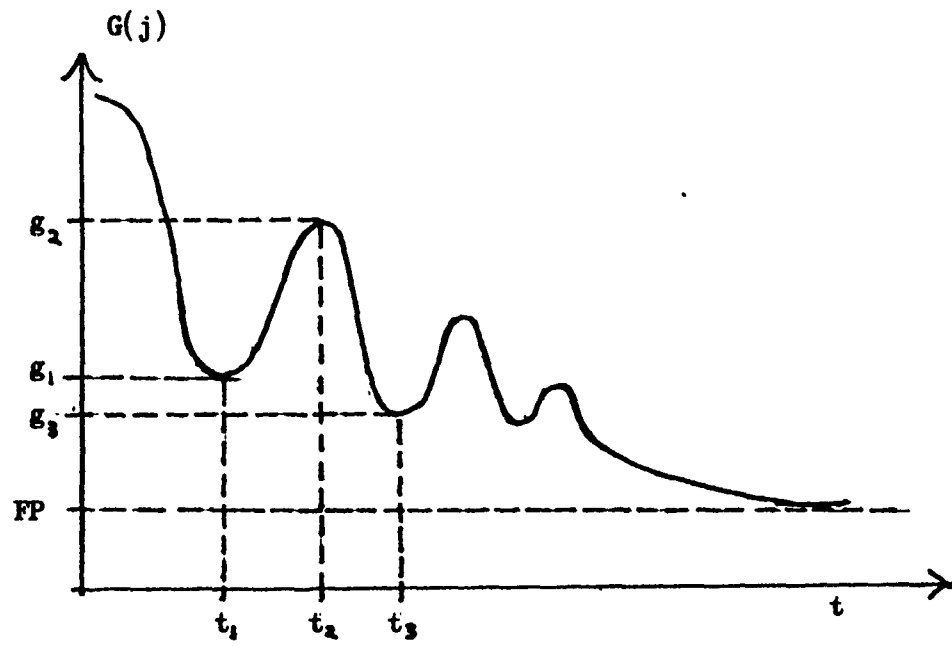


FIGURE 8 CORRELATION FUNCTION

- BOUNDARIES - TABLE 1

BNDRY ZONE	BOUNDARY CONDITIONS											
	(U)	(V)	(W)	(E)	(D)	(T)	(F)	(G)	(H)	(I)	(J)	(K)
W0	0. 0E-01W	0. 0E-01W	0. 0E-01W	0. 0E-01S	0. 0E-01S	2. 7E 02W	0. 0E-01C	R				
W1	0. 0E-01W	0. 0E-01W	0. 0E-01W	0. 0E-01S	0. 0E-01S	2. 7E 02W	0. 0E-01C	R				
W2	0. 0E-01W	0. 0E-01W	0. 0E-01W	0. 0E-01S	0. 0E-01S	2. 7E 02W	0. 0E-01C	R				
W2	0. 0E-01W	0. 0E-01W	0. 0E-01W	0. 0E-01S	0. 0E-01S	2. 7E 02W	0. 0E-01C	R				
W4	0. 0E-01W	0. 0E-01W	0. 0E-01W	0. 0E-01S	0. 0E-01S	2. 7E 02W	0. 0E-01C	R				
W5	0. 0E-01W	0. 0E-01W	0. 0E-01W	0. 0E-01S	0. 0E-01S	2. 7E 02W	0. 0E-01C	R				
W5	0. 0E-01W	0. 0E-01W	0. 0E-01W	0. 0E-01S	0. 0E-01S	2. 7E 02W	0. 0E-01C	R				
W7	0. 0E-01W	0. 0E-01W	0. 0E-01W	0. 0E-01S	0. 0E-01S	2. 7E 02W	0. 0E-01C	R				
W8	0. 0E-01W	0. 0E-01W	0. 0E-01W	0. 0E-01S	0. 0E-01S	2. 7E 02W	0. 0E-01C	R				
W9	0. 0E-01W	0. 0E-01W	0. 0E-01W	0. 0E-01S	0. 0E-01S	2. 7E 02W	0. 0E-01C	R				
0	0. 0E-01L	0. 0E-01L	0. 0E-01L	0. 0E-01L	0. 0E-01L	2. 7E 02L	0. 0E-01L	R				
10	2. 6E 01L	0. 0E-01L	-5. 6E 01L	5. 6E 01L	5. 6E 01L	1. 1E 05L	2. 7E 02L	0. 0E-01L	0. 0E-01L	0. 0E-01L	0. 0E-01L	R
11	2. 6E 01L	0. 0E-01L	3. 2E 01L	2. 6E 01L	3. 7E 04L	2. 7E 02L	0. 0E-01L	R				
12	1. 4E 01L	1. 1E 01L	0. 0E-01L	4. 9E 00L	4. 2E 03L	2. 7E 02L	0. 0E-01L	R				
13	0. 0E-01L	0. 0E-01L	0. 0E-01L	0. 0E-01L	0. 0E-01L	2. 7E 02L	0. 0E-01L	R				
14	0. 0E-01L	0. 0E-01L	0. 0E-01L	0. 0E-01L	0. 0E-01L	2. 7E 02L	0. 0E-01L	R				
15	0. 0E-01L	0. 0E-01L	0. 0E-01L	0. 0E-01L	0. 0E-01L	2. 7E 02L	0. 0E-01L	R				
16	0. 0E-01L	0. 0E-01L	0. 0E-01L	0. 0E-01L	0. 0E-01L	2. 7E 02L	0. 0E-01L	R				
17	0. 0E-01L	0. 0E-01L	0. 0E-01L	0. 0E-01L	0. 0E-01L	2. 7E 02L	0. 0E-01L	R				
18	0. 0E-01L	0. 0E-01L	0. 0E-01L	0. 0E-01L	0. 0E-01L	2. 7E 02L	0. 0E-01L	R				
19	0. 0E-01L	0. 0E-01L	0. 0E-01L	0. 0E-01L	0. 0E-01L	2. 7E 02L	0. 0E-01L	R				

- GEOMETRY - TABLE 2

CYLINDRICAL POLAR COORDINATES - INNER RADIUS = 0.000E-01
NI = 31 NJ = 31 NK = 1

NO.	X-GRID	Y-GRID	Z-GRID	[GRID POSITIONS (m)]
1	-2.0000E-03	-7.5000E-04	1.0000E 00	
2	2.0000E-03	7.5000E-04	1.0000E 00	
3	6.0000E-03	2.6250E-03	0.0000E-01	
4	1.0000E-02	4.5000E-03	0.0000E-01	
5	1.4000E-02	5.5000E-03	0.0000E-01	
6	1.8000E-02	6.8400E-03	0.0000E-01	
7	2.2000E-02	8.1800E-03	0.0000E-01	
8	2.5500E-02	9.5000E-03	0.0000E-01	
9	2.9000E-02	1.0500E-02	0.0000E-01	
10	3.6000E-02	1.1500E-02	0.0000E-01	
11	4.6000E-02	1.2800E-02	0.0000E-01	
12	5.6000E-02	1.4600E-02	0.0000E-01	
13	6.6000E-02	1.6400E-02	0.0000E-01	
14	7.6000E-02	1.8200E-02	0.0000E-01	
15	8.6000E-02	2.0000E-02	0.0000E-01	
16	9.6000E-02	2.1600E-02	0.0000E-01	
17	1.0600E-01	2.3300E-02	0.0000E-01	
18	1.1600E-01	2.4900E-02	0.0000E-01	
19	1.2600E-01	2.6000E-02	0.0000E-01	
20	1.3600E-01	2.8000E-02	0.0000E-01	
21	1.4900E-01	3.2000E-02	0.0000E-01	
22	1.6300E-01	3.6000E-02	0.0000E-01	
23	1.7800E-01	4.1000E-02	0.0000E-01	
24	1.9325E-01	4.6000E-02	0.0000E-01	
25	2.0850E-01	5.0900E-02	0.0000E-01	
26	2.2375E-01	5.5800E-02	0.0000E-01	
27	2.3900E-01	6.0300E-02	0.0000E-01	
28	2.5890E-01	6.3800E-02	0.0000E-01	
29	2.7880E-01	6.6790E-02	0.0000E-01	
30	2.9483E-01	6.8793E-02	0.0000E-01	
31	3.0517E-01	7.1207E-02	0.0000E-01	

- CELL TYPES - TABLE 3

THE F101 COMBUSTOR TEST FACILITY AND MERCURY PULSE
TRACER MEASUREMENTS.

Introduction.

The finite difference programmes developed at Sheffield for the modelling of gas turbine combustors, incorporates a stochastic particle tracking algorithm to predict droplet trajectories. Here individual droplets are tracked through the combustion chamber as they experience the predicted flow velocities. At each location a turbulent contribution is also included whose magnitude is based on the random choice of a normally distributed variable simulating Gaussian turbulence and whose duration is based on an eddy decay model.

Such a procedure can also be used for the converged flowfields with a neutrally buoyant fluid tracer element. If sufficient elements are tracked from a fixed input position to the exit plane then the resulting number versus time is the RTD function at the exit embodying the effects of broadening due to turbulence and recirculation.

By comparing these results with measured RTD functions at the exit of the combustor it is possible to check the accuracy of the predicted 3 dimensional flow field and the particle tracking algorithm. The results can also be used to predict the blow off limits for the combustor, Ewan et al. (2).

This report describes measurement of RTD functions which will be used to check the accuracy of F101 combustor modelling.

The F101 combustor test facility.

The test combustor is a 54° sector of a full annular F101 engine combustor. This comprises a combustor dome, containing 3 air blast fuel atomizers and associated inlet swirlers, together with inner and outer liners all of which are fabricated from actual engine parts (figure 2).

The chamber is mounted in a stainless steel vessel. This allows operation under pressure and can be opened to allow easy access for measurement when operating at atmospheric pressure. Air is supplied from a four cylinder reciprocating compressor at pressures of up to 100 psi. High pressure and realistic operating conditions can be achieved by discharging air from a storage tank. Figure 1 shows the test facility.

Combustor Instrumentation.

Total air flow is measured by means of a square edged orifice plate with corner taps and primary air flow by means of a venturi meter. Differential and upstream pressures are measured using mercury manometers. Air temperature is monitored using chromel-alumel thermocouples with signal conditioning by means of RSAD595AD amplifier/cold junction compensators.

Mercury pulse tracer method.

Theory.

The residence time distribution (RTD), denoted $E(t)$, is defined as the fraction of material at the exit with a residence time between t and $t+dt$. It can be determined by introducing a pulse of tracer material into the chamber over a period of time short compared to the mean residence time and by monitoring the change of tracer concentration with time at the exit.

The concentration versus time information can be converted into the form of an RTD by normalising. This makes the result independent of the actual size of tracer pulse. It is usual to take the average of many RTD measurements to eliminate the effect of random fluctuations observed from one experiment to the next. The data in this form is suitable for comparison with computer model results.

Most tracer methods employ solenoid operated valves to introduce steps or pulses in a gas or dye concentration entering the chamber. However, these methods often generate pulses with long rise times compared to the mean residence time. This is a serious problem with high intensity combustors where residual lifetimes are low. Topps (1) has designed a method in which a pulse of mercury is produced by passing an electric spark across the ends of two mercury amalgam electrodes. As the mercury vapour leaves the combustor its concentration is monitored. This is done by making use of its ability to absorb U.V. light produced by a low pressure mercury lamp and detected by a photomultiplier. The method has been used successfully at Sheffield on a Lycoming gas turbine combustor can. B.C.R. Ewan (2). Tests have also been carried out in laminar pipe flow by means of which it was shown that pulses of around 1.2 micro second duration could be produced.

Experimental apparatus.

The mercury spark electrode.

This comprises a length of twin bore refractory tubing into which dental amalgam has been packed. Details of construction can be found in reference (2). The electrode was inserted into the combustion chamber through a suitable hole drilled in the outer casing. The mercury vapour pulse was generated by discharging a 0.1 micro farad capacitor across the tip after charging to 800 V from an EHT supply.

Detection apparatus.

Tracer concentration at the exit was measured using a low pressure mercury vapour lamp emitting radiation at 253.7 nanometres wave length and an EMI type 9789QB photomultiplier tube with an entrance aperture of 2 mm diameter. (Hence a 2 mm diameter cylinder at the exit was monitored.)

A CMB computer with machine code program and analogue to digital converter, were employed to record the PM output as mercury excited the combustor. Data acquisition was triggered at the instant of firing the electrode using a 5V pulse from the capacitor discharge circuit. 1024 12 bit values were recorded at 0.7 milli-second intervals. These were then stored on disc for processing into RTD functions at a later stage.

Results.

The RTD obtained from the average of 50 separate pulse injections is shown in figure 2. These were obtained when the pulse was injected at the location of the F101 surface discharge igniter and with the combustor operating at atmospheric pressure.

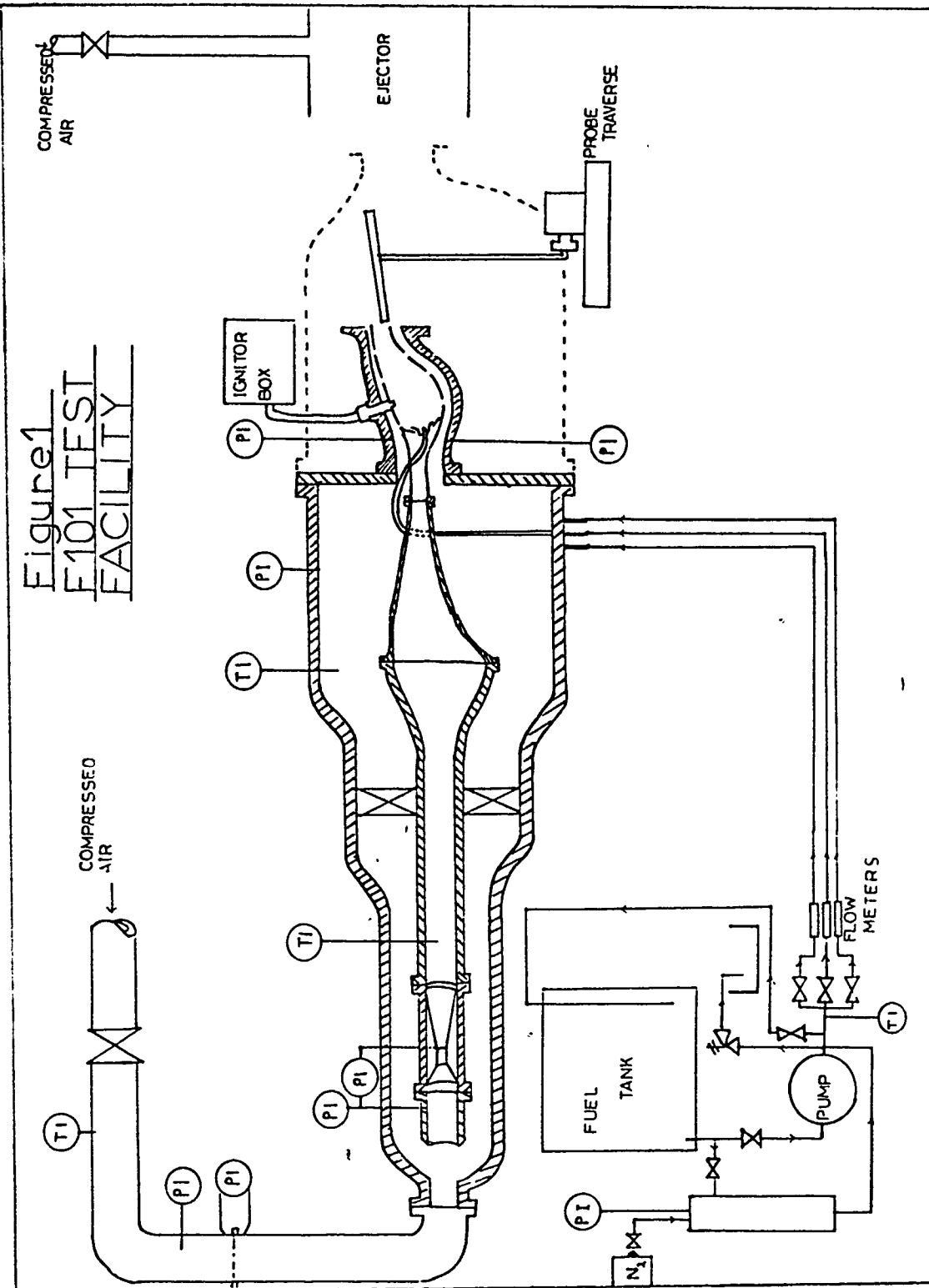
Conclusion.

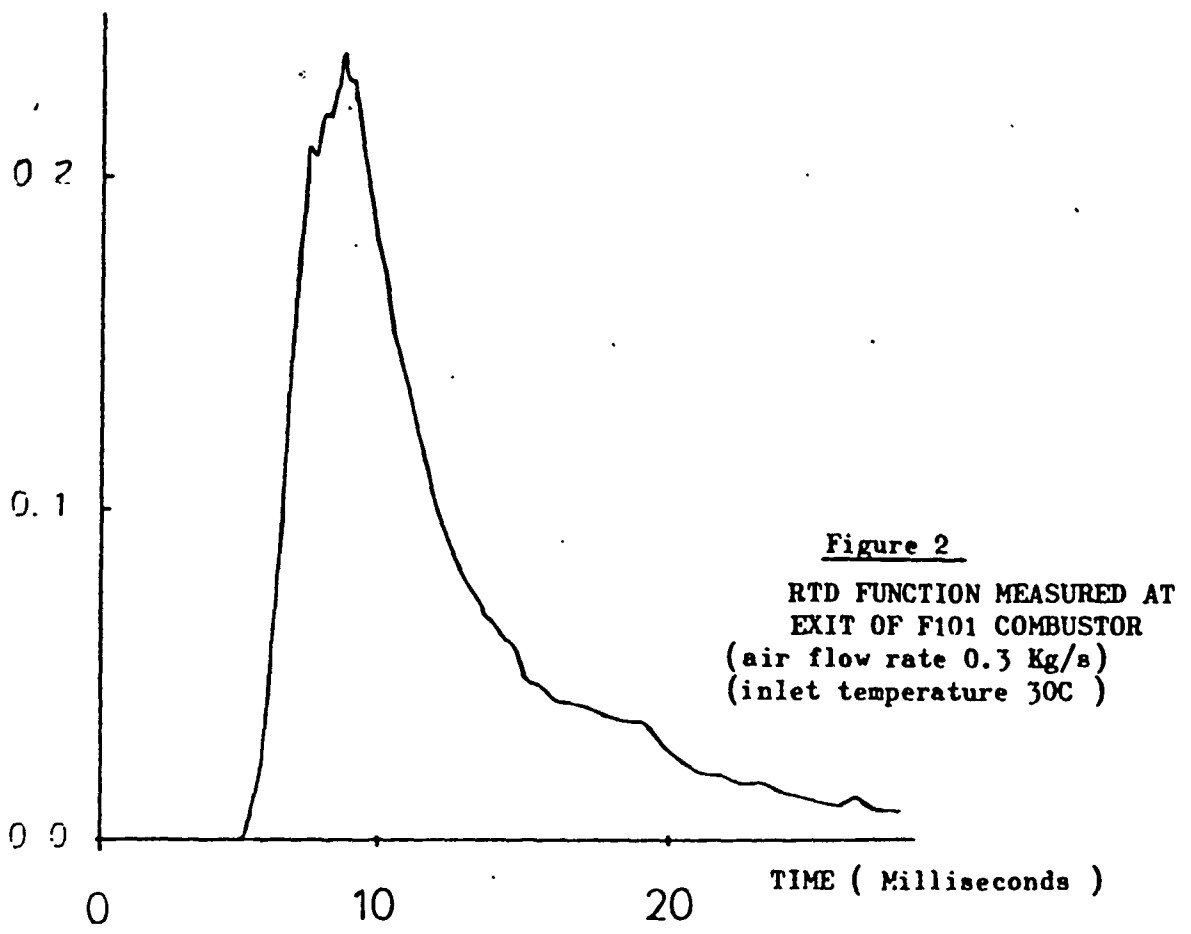
Residence time distribution measurements have been made in the F101 gas turbine combustion chamber. Work to obtain more data and to simulate the results numerically is continuing.

References.

- (1) J.E.C. Topps, "An optical technique for the investigation of flow in gas turbine combustors", 17th Symposium (International) on Combustion, The Combustion Institute 1978.
- (2) B.C.R. Ewan, F. Boysan and J. Swithenbank, "Closing the gap between finite difference and stirred reactor combustor modelling procedures", 20th Symposium (International) on Combustion, The Combustion Institute, 1984.

Figure 1
E101 TEST
FACILITY





ON THE MODELLING OF THE RETURN TO
ISOTROPY OF HOMOGENEOUS NON-ISOTROPIC TURBULENCE

by
S. A. Vasquez-Malebran and F. Boysan

Department of Chemical Engineering and
Fuel Technology, The University of
Sheffield, Mappin Street,
Sheffield, S1 3JD

Contents

Notation	
1. Introduction	1
2. Equations for the Invariants	5
3. Cubic equation for the Principal Reynolds stress components	7
4. Some solutions for the equations of the Invariants	12
4.1 Neglecting non-linear effects	13
4.2 Non-linear term in the pressure- strain tensor	15
5. Results for non-axisymmetric flows	19
5.1 Tucker and Reynolds Experiment (1968)	20
5.2 Gence and Mathieu Experiment (1980)	20
5.3 Le Penven, Gence and Compte-Bellot Experiment (1984)	22
6. Conclusions	23
7. Acknowledgements	25
References	26
Appendix A	28
Appendix B	30
Figures	33

Notation

ν	kinematic viscosity
$\overline{u_i u_j}$	Reynolds stress tensor
p	pressure
ϵ	viscous energy dissipation rate
ρ	density
ψ_{ij}	pressure-strain tensor
b_{ij}	anisotropy tensor
k	turbulent kinetic energy
c_1	constant of the linear part of the pressure-strain tensor
λ	constant of the non-linear part of the pressure strain tensor
II	second invariant of the anisotropy tensor
III	third invariant of the anisotropy tensor
$c_{\epsilon 2}$	constant of the model for energy dissipation
\bar{U}	mean velocity in the x_1 direction
τ	normalised time
t	elapsed time
a_1	constant equal to $c_1 - 1$
\bar{u}^2	streamwise component of the Reynolds stress tensor
\bar{v}^2	lateral component of the Reynolds

	stress tensor
\bar{w}^2	component of the Reynolds stress tensor in the x_3 direction
ω	perturbation parameter
Ω	parameter that measures the departure from axisymmetry
P_{ij}	production tensor
P	half the trace of the production tensor
σ	principal components of the Reynolds stress tensor
x_i	space coordinates
R_M	grid Reynolds number $\frac{U_M}{v}$
\bar{u}^2_p	principal component of the Reynolds stress tensor
\bar{v}^2_p	principal component of the Reynolds stress tensor
\bar{w}^2_p	principal component of the Reynolds stress tensor

superscript

— average value

ON THE MODELLING OF THE RETURN TO
ISOTROPY OF HOMOGENEOUS NON-ISOTROPIC TURBULENCE

by
S. A. Vasquez-Malebran and F. Boysan

Department of Chemical Engineering and
Fuel Technology, The University of
Sheffield, Mappin Street,
Sheffield, S1 3JD

1.- Introduction

It is well known that homogeneous anisotropic turbulence, in the absence of mean velocity gradients, approaches a state of equilibration of the diagonal components of the Reynolds stress tensor. This phenomenon which is associated to the redistribution of energy among its components, embodied in the general dynamics of decay of the energy containing eddies, has been observed experimentally by various authors (Ref. 2,3,10,11). Since pressure interaction forces are mainly responsible for this behaviour, return to isotropy of homogeneous turbulence is very important from the point of view of the modelling of the pressure-strain tensor.

The transport equation for the Reynolds stress tensor, in homogeneous turbulent flow without mean strain is:

$$\frac{D u_i u_j}{Dt} = \rho \left[\frac{\partial u_i}{\partial x_j} + \frac{\partial u_j}{\partial x_i} \right] - 2\nu \left[\frac{\partial u_i \partial u_j}{\partial x_k \partial x_k} \right] \quad (1)$$

where the term on the left hand side represents the convective transport of the Reynolds stress tensor while the terms on the

right hand side are the pressure-strain and the dissipation terms respectively. The expression for the pressure strain term follows from the fact that in homogeneous turbulence

$$\overline{u_i \frac{\partial p}{\partial x_j}} = \overline{p \frac{\partial u_i}{\partial x_j}}.$$

Although, without analytical proof, it can be said on physical grounds, that the role of the pressure-strain term is to force an equilibration of the diagonal components of the Reynolds stress tensor, nothing can be concluded from equation (1) about the direction of the energy transfer and the speed at which the tendency towards equipartition is evolving. The dissipation term in the above equation is usually replaced by its isotropic part $\frac{2}{3}\epsilon\delta_{ij}$, with

$$\epsilon = v \left[\frac{\partial u_i \partial u_i}{\partial x_k \partial x_k} \right].$$

The transport equation for the viscous dissipation rate in unstrained, high Reynolds number, homogeneous turbulence, neglecting diffusional effects of pressure fluctuations can be expressed as:

$$\frac{D\epsilon}{Dt} = -2 \left[\frac{\partial u_i \partial u_i \partial x_j}{\partial x_j \partial x_k \partial x_k} + \left[\frac{\partial^2 u_i}{\partial x_k \partial x_j} \right]^2 \right] \quad (2)$$

where, following Hanjalic and Launder (1972), the first term on the right hand side represent the generation rate of vorticity fluctuations through the self-stretching action of turbulence, and the second term is the decay of the dissipation rate through the action of viscosity.

Unfortunately there is no a direct solution for these complex equations even in the case of homogeneous turbulence and therefore only qualitative information can be inferred from these. To advance in the solution of the problem it is necessary to introduce modelling assumptions.

For the transport equation of the Reynolds stress components the explicit appearance of the pressure-strain term satisfies a quasi-Poisson equation as shown by Chou (1945). The solution for this Poisson equation, for the case of unstrained flows shows that the pressure-strain originates from the interaction between turbulence components. On physical grounds Rotta (1951) suggested that this term may be, as a first approximation, proportional to the anisotropy tensor b_{ij}

$$\psi_{ij} = \frac{p}{\rho} \left[\frac{\partial u_i}{\partial x_j} + \frac{\partial u_j}{\partial x_i} \right] = -c_1 \epsilon b_{ij}$$

with

$$b_{ij} = \frac{\overline{u_i u_j}}{k} - \frac{2}{3} \delta_{ij}$$

where c_1 is a constant of proportionality, and $k = \frac{1}{2} \overline{u_i u_i}$ the

turbulent kinetic energy.

Using different approaches to the modelling of this term, Lumley (1977) Speziale (1980), Launder (private communication) have expanded this expression incorporating non-linear terms. On the whole, based on the current pressure-strain models proposed, equation (1) can be expressed in the following general form:

$$\frac{D u_i u_j}{Dt} = -c_1 \epsilon b_{ij} + \lambda \epsilon (b_{ik} b_{kj} - \frac{1}{3} II \delta_{ij}) - \frac{2}{3} \epsilon \delta_{ij} \quad (3)$$

where $II = b_{ik} b_{ki}$ is the second invariant of the anisotropy tensor, c_1 and λ can be either constants or functions of some relevant parameters.

For the equation of viscous dissipation rate Rodi (1971) has argued that both terms in the right hand side of equation (2) should be modelled together. These terms are governed by the dynamics of the transfer of energy from low to high wave numbers and so they are independent of viscosity; on dimensional considerations it can be suggested that:

$$2 \left[v \frac{\partial u_i}{\partial x_j} \frac{\partial u_i}{\partial x_k} \frac{\partial u_j}{\partial x_k} + \left[v \frac{\partial^2 u_i}{\partial x_k \partial x_j} \right]^2 \right] = c_{\epsilon} 2 \frac{\epsilon^2}{k}$$

where $c_{\epsilon 2}$ is a constant. Lumley and Khajeh-Nouri (1972) have suggested independently that the factor $c_{\epsilon 2}$ should be a dimensionless invariant function, and that this invariant

function, in the general case, contains the entire mechanism of production and destruction of dissipation.

Thus, based on the currents models, the equation for the viscous dissipation rate is

$$\frac{D\epsilon}{Dt} = -c_{\epsilon} \frac{\epsilon^2}{k} \quad (4)$$

Equations (3) and (4) constitute a closed system and can be solved using numerical procedures. The constants involved in the modelling are tuned in the light of experimental data. But since the modelling of the rate of energy dissipation equation is usually based on simplifying assumptions, the conclusions can be sometimes misleading. A rather different approach is adopted here to obtain the variation of the components of the Reynolds stress tensor, along the flow.

2.- Equations for the Invariants.

It may be shown empirically that the decay of turbulent kinetic energy implies, for an initially anisotropic turbulent flow without mean velocity gradients, a decay in the state of anisotropy and consequently a decay of the second invariant of the anisotropy tensor (this second invariant can be regarded as a measure of the anisotropy of the flow), and also a decay of the absolute value of the third invariant. By constructing differential transport equations for these invariants (see Appendix A) it would be possible to obtain more information of

the distribution of energy among the components.

Based on the models outlined on the preceding paragraphs, the following equations may be constructed:

$$\frac{\partial k}{\partial t} = -\epsilon \quad (5)$$

$$\frac{\partial \epsilon}{\partial t} = -C_{\epsilon}^2 \frac{\epsilon^2}{k} \quad (6)$$

$$\frac{\partial II}{\partial t} = -2\frac{\epsilon}{k} \left[(c_1 - 1)II - \lambda III \right] \quad (7)$$

$$\frac{\partial III}{\partial t} = -3\frac{\epsilon}{k} \left[(c_1 - 1)III - \frac{\lambda}{6} II^2 \right] \quad (8)$$

with $\frac{\partial}{\partial t} = \bar{U} \frac{\partial}{\partial x}$ and $III = b_{ik} b_{kj} b_{ji}$ being the third invariant of the anisotropy tensor.

To avoid implications arising from the approximate modelling of the dissipation transport equation a non-dimensional time related to the natural time of decay of the turbulent energy can be introduced

$$\frac{\epsilon}{k} dt = d\tau \quad \text{with} \quad \tau = -\ln\left(\frac{k}{k_0}\right)$$

where k_0 is the initial value of the turbulent kinetic energy. Then the equations (5), (6), (7) and (8) become

$$\frac{\partial k}{\partial \tau} = k \Rightarrow k = k_0 e^{-\tau} \quad (9)$$

$$\frac{\partial \text{II}}{\partial \tau} = -2 \left[(c_1 - 1) \text{II} - \lambda \text{III} \right] \quad (10)$$

$$\frac{\partial \text{III}}{\partial \tau} = -3 \left[(c_1 - 1) \text{III} - \frac{\lambda}{6} \text{II}^2 \right] \quad (11)$$

To solve these equations the normalised time τ is taken from the experiments. In this way the problem of solving a tensor equation with three components and a scalar equation for the energy dissipation with the elapsed time as the independent variable has been transformed into the solution of three scalar equations with the normalised time, which is related to the natural time of decay, as the independent variable. Thus by solving the equations for the turbulent kinetic energy, the second and third invariant of the anisotropy tensor, the implications of the assumptions involved in the modelling of the energy dissipation has been eliminated and the effects of the pressure-strain term isolated. The physical meaning of the second invariant II is that it is a measure of the state of anisotropy of the flow, and the role and physical meaning of the third invariant in the return to isotropy process shall be dealt in the next section.

3.- Cubic equation for the Principal Reynolds stress components.

For a given variation of the invariants with respect to the normalised time, the principal components of the Reynolds stress tensor can be recovered from the following algebraic

relations:

$$b_{ii} = 0 \quad (12)$$

$$b_{ik} b_{ki} = II \quad (13)$$

$$b_{ik} b_{kj} b_{ji} = III \quad (14)$$

For the axisymmetric case the diagonal components of the anisotropy tensor b_{ij} can be expressed as $b_{11} = -b$, $b_{22} = b_{33} = \frac{1}{2}b$, with $b > 0$, giving $II = \frac{3}{2}b^2$ and $III = \frac{3}{4}b^3$ so that $III < 0$ or as $b_{11} = b$, $b_{22} = b_{33} = \frac{1}{2}b$, with $b > 0$, giving $II = \frac{3}{2}b^2$ and $III = \frac{3}{4}b^3$ thus $III > 0$, it can be seen from here that III is positive when two components of the Reynolds stress tensor are less than the isotropic level $\frac{2}{3}k$ and III is negative when two components are larger than the isotropic level (a similar explanation was first given by Gence and Mathieu (1980), the third invariant is positive when the component of the Reynolds stress tensor along the symmetry axis is greater than the two others, and is negative in the opposite case). The solutions of the algebraic relations for this particular case are:

$$\bar{u}^2 = k \left[\frac{2}{3} + \sqrt{\frac{2}{3}II} \right]$$

$$\bar{v}^2 = k \left[\frac{2}{3} + \sqrt{\frac{1}{6} II} \right] = \bar{w}^2$$

where the sign to be taken follows from the above discussion, depending on the sign of the third invariant III.

Moreover for the general case when three components of the Reynolds stress tensor are distinct a cubic equation may be obtained:

$$x^3 - \frac{1}{2} IIx - \frac{1}{3} III = 0 \quad (15)$$

with x representing the individual components of the anisotropy tensor. For the problem to have a physical meaning the three roots of equation (15) must be real since each root corresponds to each diagonal component of the anisotropy tensor. From the algebraic solution of the cubic equation

$$F(x) = ax^3 + 3bx^2 + 3cx + d = 0$$

with $Q = ac - b^2$ and $R = \frac{1}{2}(3abc - da^2) - b^3$ it follows that

(i) If $Q^3 + R^2 = 0$ ie. $6III^2 - II^3 = 0$, $F(x)$ has three real roots of which at least two are equal, this is the axisymmetric case and a strong realizability condition for axisymmetry appears in terms of the invariants, ie. $6III^2 - II^3 = 0$

(ii) If $Q^3 + R^2 = 0$ ie. $6III^2 - II^3 > 0$ $F(x)$ has one real root only and the other two are complex, this solution has no physical meaning.

(iii) If $Q^3 + R^2 = 0$ ie. $6III^2 - II^3 < 0$ $F(x)$ has three distincts real roots which correspond to the three principal velocity correlations.

The solution for the principal components of the Reynolds stress tensor is:

$$\sigma = k \left[\frac{2}{3} + \sqrt{\frac{2}{3}} II \cos \left[\frac{1}{3} \tan^{-1} \left[\frac{II^3 - 6III^2}{6III^2} \right]^{\frac{1}{2}} + \frac{n\pi}{3} \right] \right] \quad (16)$$

where $n = 0, 2, 4$; when $III > 0$ the upper sign is used and when $III < 0$ the lower sign is used (the sign follows from the sign of R in the general solution for the cubic equation, which in our case turns out to be the sign of the third invariant)

Observing these simple analytical solutions for the energy components a physical picture of the evolution of these in return to isotropy can be suggested. It can be noted that the sign of the third invariant remains constant during the process of return to isotropy. A change of sign means that the turbulence have passed through a state where there are only two equal and of opposite sign nonzero components for the anisotropy tensor so

that $III=0$, (the diagonal components of the anisotropy tensor in this state are of the form $b_{11} = b$, $b_{22} = -b$, and $b_{33} = 0$). This phenomenon is not physically probable without the external production of energy through the action of velocity gradients and it follows therefore that the variation of the angles

$$\alpha = \frac{1}{3} \tan^{-1} \left[\frac{II^3 - 6III^2}{6III^2} \right]^{\frac{1}{2}} + n\frac{\pi}{3}$$

with $n = 0, 2, 4$ cannot be equal or more than 30° , therefore no change of the sign of the cosine of these angles is expected during the process. When the third invariant is negative the smallest component has the largest absolute value of the respective cosine term in the solution of the cubic equation, and it is approaching isotropy from below the isotropic level $\frac{2}{3}k$. This component is gaining energy from the other two larger components, (both are approaching isotropy from above the isotropic level) in a proportion which may be related to the absolute value of their respective cosine terms. Therefore it is likely that there will be an increase of energy in the smaller component and the process of return to isotropy will be faster.

When the third invariant is positive the picture is quite the contrary. The largest component has now the largest absolute value of the cosine term and it is giving energy to the other two smaller components (which are approaching isotropy from below the isotropic level). If the relative amount of energy shared by the

smaller components is taken to be proportional to the absolute value of their respective cosine terms, the smaller the component the greater is the amount of relative energy accumulated from the largest component. But, because of the sharing it is unlikely for the smallest component to have a significant increase of energy during the process and the return to isotropy is likely to be slower than when the third invariant is negative. With this mechanism in mind it is seen that the direction of the flow of energy and possibly the relative amount of energy transferred among the components is governed by the sign of the third invariant, the sign of the cosine terms in the solution of the cubic equation and the absolute value of their respective cosine terms. It should be mentioned that the influence of the third invariant in the dynamics of return to isotropy was suggested by the Gence and Mathieu experiment (1980).

Another observation from the solution of (15) is that there appears to be a realizability condition for the existence of unstrained homogeneous turbulence in terms of the invariants which can be expressed as $6III^2 - II^3 \leq 0$; but since in theory any turbulent flow may be characterized by its invariants this general realizability condition should be satisfied by any proposed model of turbulence. The simplicity of this expression constitutes a very simple test for the phenomenological models.

4.- Some solution for the equations of the Invariants.

The next step in this analysis is to solve the equations for the invariants as a function of the normalized time

4.1- Neglecting non-linear effects ($\lambda = 0$)

When c_1 is a constant we have Rotta's proposal (1951), and the analytical solutions for II and III are

$$II = II_0 e^{-2(c_1 - 1)\tau} \quad (17)$$

$$III = III_0 e^{-3(c_1 - 1)\tau} \quad (18)$$

with II_0 and III_0 being the initial values for the second and third invariants. From these solutions we obtain $\frac{II^3}{III^2} = \text{constant}$, which is only true for homogeneous axisymmetric turbulent flows (constant=6) or at most when the departure from axisymmetry is small. Moreover c_1 can be estimated using the experimental data:

$$c_1 = 1 + \frac{1}{2 \ln(\frac{k}{k_0})} \ln\left(\frac{II}{II_0}\right)$$

with $k < k_0$, $II < II_0$ everywhere, and since decays means that the values of the second invariant and the kinetic energy in the process are less than their respective initial values it follows that $c_1 > 1.0$. (this can also be seen from the solutions (17) and (18) where if $c_1 < 1.0$ there would be an increase in the anisotropy)

of the flow without the action of a generation term)

When one uses the data of Uberoi (195) (anisotropic decaying turbulence submitted to axisymmetric plane strain with a contraction ratio of 4:1) to estimate the constant c_1 , it becomes apparent that there is not a unique value which gives the same agreement for the three different contraction ratios of the axisymmetric duct used in the experiments. Furthermore, the value of c_1 varies along the development of the flow: $1.2 \leq c_1 \leq 2.3$. As a first approximation c_1 can be taken a constant with $c_1 = 2.0$ giving reasonably agreement within the uncertainty of the experimental data. Figures 1, 2, and 3 shows this satisfactory agreement.

When $\lambda = 0$ and c_1 is not a constant. For this situation equations (7) and (8) may be reduced to:

$$(3III)\frac{dII}{dt} = (2II)\frac{dIII}{dt} \quad (19)$$

and solving, one obtains

$$\frac{II^3}{III^2} = \text{constant}$$

Again the same condition as for c_1 being a constant is obtained. Therefore any improvement in the modelling of the pressure-strain term, for the return to isotropy, in expressing c_1 as a function of some relevant parameters (Lumley (1978)) is still unsatisfactory to model non-axisymmetric flows.

4.2 Non-linear term in the pressure-strain tensor

Focusing attention on the complete expression for the pressure-strain tensor in the return to isotropy process and for simplicity taking c_1 and λ to be constants, the constraints imposed by the linear model can be avoided.

(i) Axisymmetric flows

A straightforward analytical solution is obtained in the axisymmetric case:

$$III = \frac{-1}{+\sqrt{6}} III^{\frac{3}{2}}$$

when substituted into equation (8) one obtains

$$\frac{dII}{d\tau} = -2 \left[(c_1-1) + \frac{\lambda}{\sqrt{6}} II^{\frac{3}{2}} \right]$$

which can be easily integrated to give

$$II = \frac{II_0 (c_1-1)^2 e^{-2(c_1-1)\tau}}{\left[(c_1-1) + \frac{\lambda}{\sqrt{6}} II_0^{\frac{1}{2}} \left[1 - e^{-(c_1-1)\tau} \right] \right]^2} \quad (20)$$

and similarly for III

$$III = \frac{III_0(c_1-1)^3 e^{-3(c_1-1)\tau}}{\left[(c_1-1) + \frac{\lambda}{\sqrt{6}} III_0^{\frac{1}{3}} \left[1 - e^{-(c_1-1)\tau} \right] \right]^3} \quad (21)$$

when $III < 0$ the upper sign is used and vice versa

Again by taking Uberoi (1956) experiment, it is possible to estimate the value of second constant λ by fixing c_1 . Along the flow the variation of λ is small for a fixed c_1 , thus if the average of λ is taken and the quantity $|\lambda| \sqrt{III_0}$ is plotted against (c_1-1) a straight line relationship between the constants is obtained (see figure 4). It is noted here that the sign of λ depends on the sign of the third invariant. Figures 5, 6, and 7 show the prediction for the Uberoi (1956) experiment with different values for c_1 and λ obtained from Figure 4. An improvement with respect to the linear model can be noted.

(ii) Non-axisymmetric flows.

When the flow is not axisymmetric an approximate analytical solution can be obtained using perturbation methods. It can be assumed that λ is small parameter and that the solution for the invariants is also a function of this parameter together with the constant c_1 .

Writing equations (10) and (11) in the form:

$$\begin{aligned}\dot{II} &= -2a_1 II + 2\lambda III \\ \dot{III} &= -3a_1 III + \frac{\lambda}{2} II^2\end{aligned}$$

where

$$\begin{aligned}\dot{II} &= \frac{dII}{d\tau} \\ \dot{III} &= \frac{dIII}{d\tau}\end{aligned}\tag{22}$$

$a_1 = (c_1 - 1)$, where II_0 and III_0 are the initial values for the invariants at $\tau = 0$ and rearranging one obtains

$$\ddot{II} + 5a_1 \dot{II} + 6a_1^2 II - \lambda^2 II^2 = 0$$

Normalising the invariants with respect to their initial values and putting $\omega^2 = \lambda^2 II_0$, with $0 < \omega < 1$ the perturbation parameter so that $0 < \lambda < \sqrt{\frac{1}{II_0}}$ equation (22) becomes:

$$\ddot{II}_n + 5a_1 \dot{II}_n + 6a_1^2 II_n - \omega^2 II_n^2 = 0\tag{23}$$

where the subscript n denotes a normalized quantity. To solve this equation the following transformation is applied:

$$II_n = X e^{-\frac{5}{2}a_1 \tau}$$

Equation (23) now reduces to

$$\ddot{X} - \frac{1}{4}a_1^2 X - \omega^2 e^{-\frac{5}{2}a_1 \tau} X^2 = 0$$

which can be easily solved using perturbation methods. (see

appendix B)

Finally when the initial conditions are introduced the solutions for the invariants are:

$$\text{II} = \left[\text{II}_0 + \frac{2\lambda \text{III}_0}{a_1} + \frac{\lambda^2 \text{II}_0^2}{2a_1^2} \right] e^{-2a_1\tau} - \left[\frac{2\lambda \text{III}_0}{a_1} + \frac{\lambda^2 \text{II}_0^2}{a_1^2} \right] e^{-3a_1\tau} \\ + \left[\frac{\lambda^2 \text{II}_0^2}{2a_1^2} \right] e^{-4a_1\tau} \quad (24)$$

and

$$\text{III} = \text{III}_0 \left[\left(1 + \frac{2\lambda \text{II}_0^2}{4a_1 \text{III}_0} \right) e^{-3a_1\tau} - \frac{2\lambda \text{II}_0^2}{4a_1 \text{III}_0} e^{-4a_1\tau} \right] \quad (25)$$

Expressions (24) and (25) indicate that λ and a_1 are important parameters which influence the speed at which the return to isotropy is taking place. When the invariants were normalised using the initial conditions, λ is related to the perturbation parameter ω as $\lambda = \omega / \sqrt{\text{II}_0}$ for $0 < \omega < 1$. Then once ω is fixed the value of λ is obtained from the initial condition of the second invariant. In section 4 it has been remarked that the third invariant has an important influence on the transfer of energy among the components and also on the speed at which the return to isotropy takes place; it is then possible to reflect how fast or slow the process of equilibration of energy is taking place through the constant a_1 . For axisymmetry, in the linear

model, $a_1 = 1.0$ gives satisfactory agreement with the data and the perturbation solution is around this state.

A new parameter which measures the initial degree of departure from axisymmetry can be defined as:

$$\Omega = 1 - \frac{III_0}{II_0}$$

so that $\Omega = 0$ for axisymmetry and $\Omega \rightarrow 1$ as the departure from axisymmetry increases. On an empirical basis the following expression for a_1 can be put forward:

$$a_1 = e^{-10\Omega III_0} \quad (26)$$

(or more generally $a_1 = e^{-f\Omega III_0}$ with f being a factor of proportionality), thus

$$a_1 = \begin{cases} < 1 & \text{for } III_0 > 0 \\ 1 & \text{for axisymmetry} \\ > 1 & \text{for } III_0 < 0 \end{cases}$$

5.- Results for non-axisymmetric flows

The above analysis is now applied to three experiments on the return to isotropy: Tucker and Reynolds (1968), Gence and Mathieu (1980), Le Penven, Gence and Comte-Bellot (1984). Table 1 presents the conditions used in the calculation of these experiments.

5.1 Tucker and Reynolds Experiment (1968)

In this experiment homogeneous grid-generated turbulence was subjected to a uniform plane strain through the action of a distorting duct with a rectangular constant cross-sectional area, measurements which reveal the tendency of the flow to become less anisotropic were taken in the parallel duct. The sign of the third invariant is negative and the component with less energy is increasing along the process of return to isotropy. Le Penven et al (1984) pointed out that this is a visible effect of the influence of the third invariant in the dynamics of equilibration of the energy components. Figures 8(a) and 8(b) show the comparison between experimental data and the analytical solutions (21) and (22) together with that of the linear model (equation 18). Good agreement is obtained with the perturbation solution in particular for the smallest component which increases its energy along the parallel duct, demonstrating the superiority of the non-linear model. It is necessary to mention that the total decay time was taken from the experiment but the decay time at each measurement in the flow was estimated from the least square fit to the experimental data, since the experimental turbulent kinetic energy does not give a smooth decay due to scatter.

5.2 Gence and Mathieu Experiment (1980)

These authors have considered the return to isotropy

phenomenon after the homogeneous turbulent flow has been submitted to two successive plane strains whose principal axes are shifted by an angle α . Two important conclusions are expressed in their paper, (a) The orientation of the principal axes of the Reynolds stress tensor does not change during the return to isotropy process and is independent of the history of the turbulence previous to the starting point of the return to isotropy, and furthermore, the axes of the pressure strain term and the axes of the Reynolds stress tensor are aligned during the whole process, and (b) the third invariant is an important parameter which influences the mechanics of the return to isotropy, the process being slower or faster according to the sign of the third invariant. Fig 9(a) to 11(b) present the comparison between the linear model (equations (17) and (18)), the perturbation solution and the experimental data. The fact that there is no change of orientation of the principal axes of the Reynolds stress tensor, when the angle between both strains were shifted, was utilized in the calculations, and the principal components were calculated from the solution of the equations for the invariants. For the angles $\alpha = 0$ and $\alpha = \frac{\pi}{4}$ excellent agreement is obtained with the perturbation solution (being superior to the linear model). When the angle $\alpha = \frac{3\pi}{4}$ it seems that the nonlinear solution does not reproduce adequately the above agreement, but this can be attributed to the fact that the initial conditions which determine the values of the constants a_1

and λ and these do not reflect the overall state of the flow (see Table 1). The data of Gence and Mathieu (1980) clearly shows that the second invariant for $\alpha = \frac{3\pi}{4}$ does not decay smoothly in the first three measurement locations of the non-distorting duct. Provided that the experimental data does not reflect major errors a possible explanation for this situation is seen when the balance of energy of the smaller component can be visualised; the smaller component is gaining energy from the largest and losing some energy by the dissipative action of viscosity, but just after the strain is suppressed the gain of the smallest component is compensating the decay and therefore the anisotropy of the flow is not decaying. The initial time of decay should then be displaced to the point when there is a clear decay of the anisotropy. Figure 11.1(a) and 11.1(b) shows this correction and the agreement is excellent.

5.3 Le Penven, Gence and Comte-Bellot Experiment (1984)

This experiment is interesting in the confirmation of the ideas put by Gence and Mathieu (1980). In this experiment the authors have observed the evolution of the kinetic energy, second invariant and the Reynolds stress components, under the influence of the third invariant with different sign. Conclusions obtained are similar to the Gence and Mathieu (1980) experiment but they go further in giving a physical interpretation of the role of the third invariant III, and emphasize its importance in the

modelling of turbulent flows.

Figures 12(a) to 13(b) present the predictions for this experiment, when the third invariant is negative good agreement is obtained with the perturbation solution. The linear solution appears to be inferior in the prediction of the smallest component. When the third invariant is negative both solutions seems to be unsatisfactory, but again using the same argument as for the third case in the experiment of Gence and Mathieu (1980) and shifting the initial time of decay, the predictions agree with the experiment with the non-linear solution being better than the linear one.

6.- Conclusions

The present analysis shows that the discrepancies between experiment and prediction with the current models of turbulence, even for the simpler case of return to isotropy, can be largely due to the modelling of the rate of dissipation of energy equation. In the return to isotropy process the effects from the modelling of the pressure-strain tensor and the ϵ -dissipation may be isolated by using a normalised time related to the natural time of decay.

Rotta's proposal (1951) and those proposals where the factor of proportionality in the modelling of the pressure-strain term is not a constant, are still unsatisfactory to model non-axisymmetry flows. Nevertheless, the linear model with ϵ_1 being a

constant gives reasonable agreement and the predictions can be improved by introducing a non-linear term with a second constant λ . In this way it is expected to avoid the constraint of axisymmetry imposed by linear modelling

A physical picture of the transfer of energy among the components of the Reynolds stress tensor is suggested on the basis of the solution of the cubic equation for the principal components of the Reynolds stress tensor; when the third invariant is negative the two larger components are giving energy to the smaller consequently the smallest component tend to increase its energy; while when the third invariant is positive the two smaller component are gaining energy from the largest and the return to isotropy is slower than the former case. Furthermore Le Penven et al. (1984) point out that when the third invariant is positive there may be a return to axisymmetry, but with the suggestions of section 4. it is possible to explain that this phenomenon is not likely to happen in all cases and depend on the particular initial configuration rather than the sign of the third invariant; if the two smaller (greater) initial energy component are nearly equal, there may be a return to axisymmetry from "below" ("above") the isotropic level when the third invariant is positive (negative), due to the direction and the relative amount of the flow of energy transferred.

Finally it should be emphasized that the six cases of these three experiments were well reproduced by the perturbation

solution.

7. Acknowledgements.

The authors are grateful to Professor B. E. Launder for stimulating discussions.

References

- 1.- Chou, P. Y. (1945) "On velocity correlations and the solution of the equations of turbulence fluctuation". Quart. Appl. Math. , 3, 38-54.
- 2.- Gence, J. N., and Mathieu J., (1980) "The Return to isotropy of an homogeneous turbulence having been submitted to two successive plane strains", J. Fluid Mech., Vol 101, 555-566
- 3.- Le Penven, L., Gence, J.N. and Comte-Bellot, "On the Approach to isotropy of Homogeneous Turbulence: Effect of the Partition of the Kinetic Energy among the Velocity Components", (1984) Fundamentals of Fluid Mechanics Conference.
- 4.- Hanjalic, K. & Launder, B. E. "A Reynolds stress model of turbulence and its application to thin shear layer flows". J. Fluids Mech. 52, 609-638.
- 5.- Lumley, J. L., "Computational Modelling of Turbulent Flows", Advances in Applied Mechanics, Vo. 18. (1978)
- 6.- Lumley, J. L., and Newman, G. R., "The return to isotropy of homogeneous turbulence", J. Fluid Mech. (1977), Vol 82, pp. 161-178
- 7.- Lumley, J. L., & Khajeh-Nouri, B. (1972) "Computational Modeling of Turbulent Transport", Adv. in Geophysics. A-18, 169-192.
- 8.- Rodi, W. (1971) "On the equation governing the rate of turbulent energy dissipation". Mech. Engng. Dept. Imperial College, Rep. TM/TN/A/14
- 9.- Rotta. J. C. (1951) "Statistische Theorie nichthomogener Turbulenz. Z. Phys., 129, 547-572.
- 10.- Tucker, H. J. , & A. J. Reynolds (1968). " The distortion of turbulence by irrotational plane strain", J. Fluid Mech., 32, 657

11.- Uberoi, M. S. (1956). "Effect of wind tunnel contraction on free stream turbulence", J. Aero. Sci. 754. .

APPENDIX A

Equation for the invariants

The equations for the invariant of the anisotropy tensor are obtained from the transport equation of the Reynolds stress tensor and from the transport equation of the turbulent kinetic energy

$$\frac{D\overline{u_i u_j}}{Dt} = P_{ij} + \Psi_{ij} - \frac{2}{3}\epsilon\delta_{ij} \quad (1)$$

$$\frac{Dk}{Dt} = P - \epsilon \quad (2)$$

where P_{ij} , Ψ_{ij} , and ϵ are the production tensor, the pressure-strain tensor and the viscous dissipation of energy respectively. The production P and the turbulent kinetic energy k are half of the trace of the production and the Reynolds stress tensor respectively

The anisotropy tensor and its invariant are defined as follows

$$b_{ij} = \frac{\overline{u_i u_j}}{k} - \frac{2}{3}\delta_{ij} \quad II = b_{ik}b_{ki} \text{ and } III = b_{ik}b_{kj}b_{ji}$$

then

$$\frac{D}{Dt} k(b_{ij} + \frac{2}{3}\delta_{ij}) = P_{ij} + \Psi_{ij} - \frac{2}{3}\epsilon\delta_{ij}$$

and using equation (2)

$$(b_{ij} + \frac{2}{3}\delta_{ij})(P - \epsilon) + k \frac{Db_{ij}}{Dt} = P_{ij} + \Psi_{ij} - \frac{2}{3}\epsilon\delta_{ij}$$

$$2b_{ij}b_{ij}(P - \epsilon) + 2kb_{ij} \frac{Db_{ij}}{Dt} = 2b_{ij}P_{ij} + 2b_{ij}\Psi_{ij}$$

it thus follows

$$k \frac{DII}{Dt} = 2(b_{ij}P_{ij} + b_{ij}\Psi_{ij}) - 2II(P - \epsilon) \quad (3)$$

In a similar way the equation for the third invariant can be obtained

$$k \frac{DIII}{Dt} = 3(b_{ik}b_{kj}P_{ij} + b_{ik}b_{kj}\Psi_{ij}) - 3III(P - \epsilon) - 2IIP \quad (4)$$

In the return to isotropy process $P_{ij} = 0$, and once inserting the expression for the pressure-strain tensor,

$$\Psi_{ij} = -\epsilon(c_1 b_{ij} - \lambda(b_{ik}b_{kj} - \frac{1}{3}II\delta_{ij})),$$

the equations (3) and (4) are reduced to

$$\frac{DII}{Dt} = -2\frac{\epsilon}{k}(c_1 - 1)II - \lambda III \quad (5)$$

$$\frac{DIII}{Dt} = -3\frac{\epsilon}{k}(c_1 - 1)III - \frac{\lambda}{6}II^2 \quad (6)$$

APPENDIX B

Solution for the Invariants using Perturbation Methods

Equations (10) and (11) of section 3 can be expressed in a simpler form as:

$$\dot{x} = -2a_1x + 2\lambda y \quad (1)$$

$$\dot{y} = -3a_1y + \frac{1}{2}\lambda x^2 \quad (2)$$

where $x=III$, $y=III$ $a_1 = c_1 - 1$, λ and c_1 being the constants connected to the non-linear and linear part of the pressure-strain term respectively. The differentiation is with respect to the defined normalised time.

Taking derivative with respect to the noemalised time again and rearranging the equations (1) and (2) one can obtain

$$\ddot{x} + 5a_1\dot{x} + 6a_1^2x - \lambda^2x^2 = 0 \quad (3)$$

Normalising the second invariant with respect to their initial values, $X = x/x_0$, equation (3) becomes:

$$\ddot{X} + 5a_1\dot{X} + 6a_1^2X - \lambda^2x_0X^2 = 0$$

Now defining ω as the perturbation parameter so that $\omega^2 = \lambda^2x_0$ for $0 < \omega < 1$ then

$$\ddot{X} + 5a_1\dot{X} + 6a_1^2X - \omega^2X^2 = 0 \quad (4)$$

To solve this equation the following transformation is applied:

$$X = U e^{-\frac{5}{2}a_1\tau}$$

equation (4) reduces to

$$\ddot{U} - \frac{1}{4}a_1^2U - \omega^2e^{-\frac{5}{2}a_1\tau}U^2 = 0.$$

Assuming that the solution may be expressed in the form

$$U = U_0 + \omega U_1 + \omega^2 U_2 + \dots$$

where U_0, U_1, U_2 , are continuous twice-differentiable functions of the normalised time τ and that $0 < \omega < 1$ is the perturbation parameter. The initial conditions obtained from equations (2) and (3) in terms of U are

$$U_0(0) = 1, \quad U_1(0) = 0, \quad U_2(0) = 0$$

and

$$\dot{U}_0(0) = \frac{1}{2}a_1$$

$$\dot{U}_1(0) = \frac{2III_0}{\sqrt{II_0 II_0}}$$

$$\dot{U}_2(0) = 0$$

Substituting the expression for U and equating coefficients of ω^r to zero for $r = 0, 1, 2$ one obtains:

$$\ddot{U}_0 - \frac{1}{4}a_1 U_0 = 0 \quad (5)$$

$$\ddot{U}_1 - \frac{1}{4}a_1 U_1 = 0 \quad (6)$$

$$\ddot{U}_2 - \frac{1}{4}a_1 U_2 = e^{\frac{5}{2}a_1\tau} U_0^2 \quad (7)$$

For equation (5) the solution is

$$U_0 = A_0 e^{\frac{1}{2}a_1\tau} + B_0 e^{-\frac{1}{2}a_1\tau}$$

where A_0 and B_0 are constants to be determined by the initial conditions, then

$$U_0 = e^{\frac{1}{2}a_1\tau} \quad (8)$$

Similarly for equation (6) the solution is

$$U_1 = A_1 e^{\frac{1}{2}a_1\tau} + B_1 e^{-\frac{1}{2}a_1\tau}$$

where A_1 and B_1 are constants, and substituting the initial conditions one obtains

$$U_1 = \frac{2III_0}{a_1II_0\sqrt{II_0}}(e^{\frac{1}{2}a_1\tau} - e^{-\frac{1}{2}a_1\tau}). \quad (9)$$

Finally for equation (7) the solution is

$$U_2 = A_2 e^{\frac{1}{2}a_1 \tau} + B_2 e^{-\frac{1}{2}a_1 \tau} + \left(\frac{1}{2a_1^2} \right) e^{-\frac{3}{2}a_1 \tau}$$

where A_2 and B_2 are constants to be determined from the initial conditions, thus

$$U_2 = \frac{1}{2a_1^2} \left(e^{\frac{1}{2}a_1 \tau} - 2e^{-\frac{1}{2}a_1 \tau} + e^{-\frac{3}{2}a_1 \tau} \right) \quad (10)$$

The final solution for the second invariant once substituting the perturbation parameter ω by the related value λ in the expansion for U and transforming to the original variable II is:

$$\begin{aligned} II &= \left(II_0 + \frac{2\lambda III_0}{a_1} + \frac{\lambda^2 III_0^2}{2a_1^2} \right) e^{-2a_1 \tau} - \dots \\ &\quad - \left(\frac{2\lambda III_0}{a_1} + \frac{\lambda^2 III_0^2}{a_1^2} \right) e^{-3a_1 \tau} + \left(\frac{\lambda^2 III_0^2}{2a_1^2} \right) e^{-4a_1 \tau} \end{aligned} \quad (11)$$

The final solution for the third invariant is obtained by using equation (1)

$$III = III_0 \left[\left(1 + \frac{\lambda III_0^2}{2a_1 III_0} \right) e^{-3a_1 \tau} - \frac{\lambda III_0^2}{2a_1 III_0} e^{-4a_1 \tau} \right] \quad (12)$$

TABLE 1

Authors	II_o	III_o	k_o	τ	Ω_o	$\bar{\Omega}$
Tucker & Reynolds (1968)	0.3139	-0.03213	0.0175	0.21	0.8	0.7
Gence & Mathieu (1980), $\alpha = 0$	0.3165	0.03502	0.1157	0.37	0.8	0.7
$\alpha = \frac{\pi}{4}$	0.2897	0.03418	0.1191	0.28	0.7	0.7
$\alpha = \frac{3\pi}{4}$	0.1294	0.01729	0.0775	0.34	0.2	0.5
Le Penven et al. (1984) (1)	0.2194	0.02487	0.02251	0.61	0.7	0.4
(2)	0.2604	-0.4248	0.03986	0.5	0.4	0.5

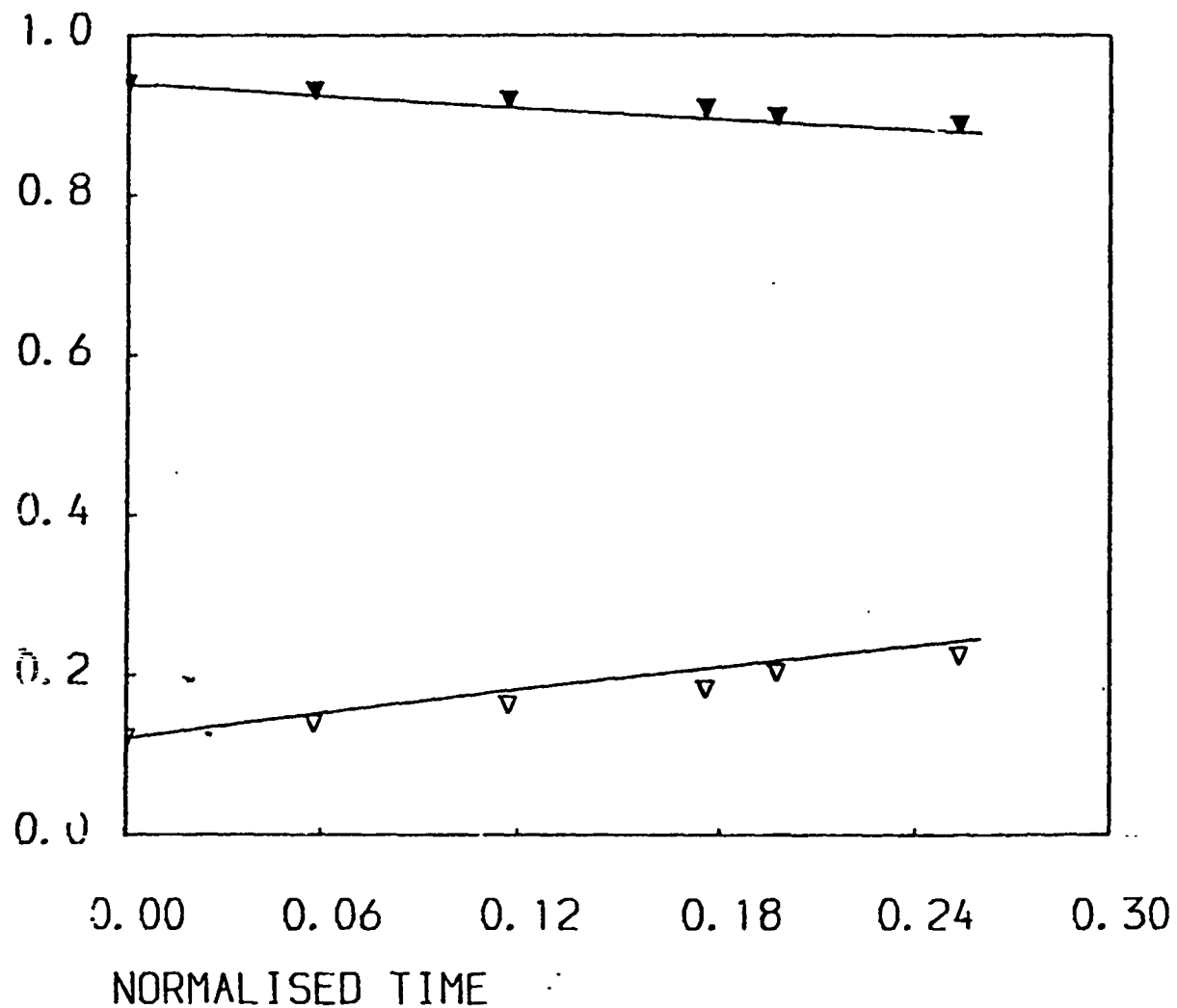


FIGURE 1 COMPARISON OF THE EVOLUTION OF THE REYNOLDS STRESS COMPONENTS IN THE UBEROI EXPERIMENT (1956) AS A FUNCTION OF THE NORMALISED TIME. LINEAR SOLUTION.
 (CONTRACTION RATIO 4:1, $R_M = 3710$; DATA:
 $\blacktriangledown \frac{\bar{v}^2}{k} = \frac{\bar{w}^2}{k}$ $\triangleright \frac{\bar{u}^2}{k}$).

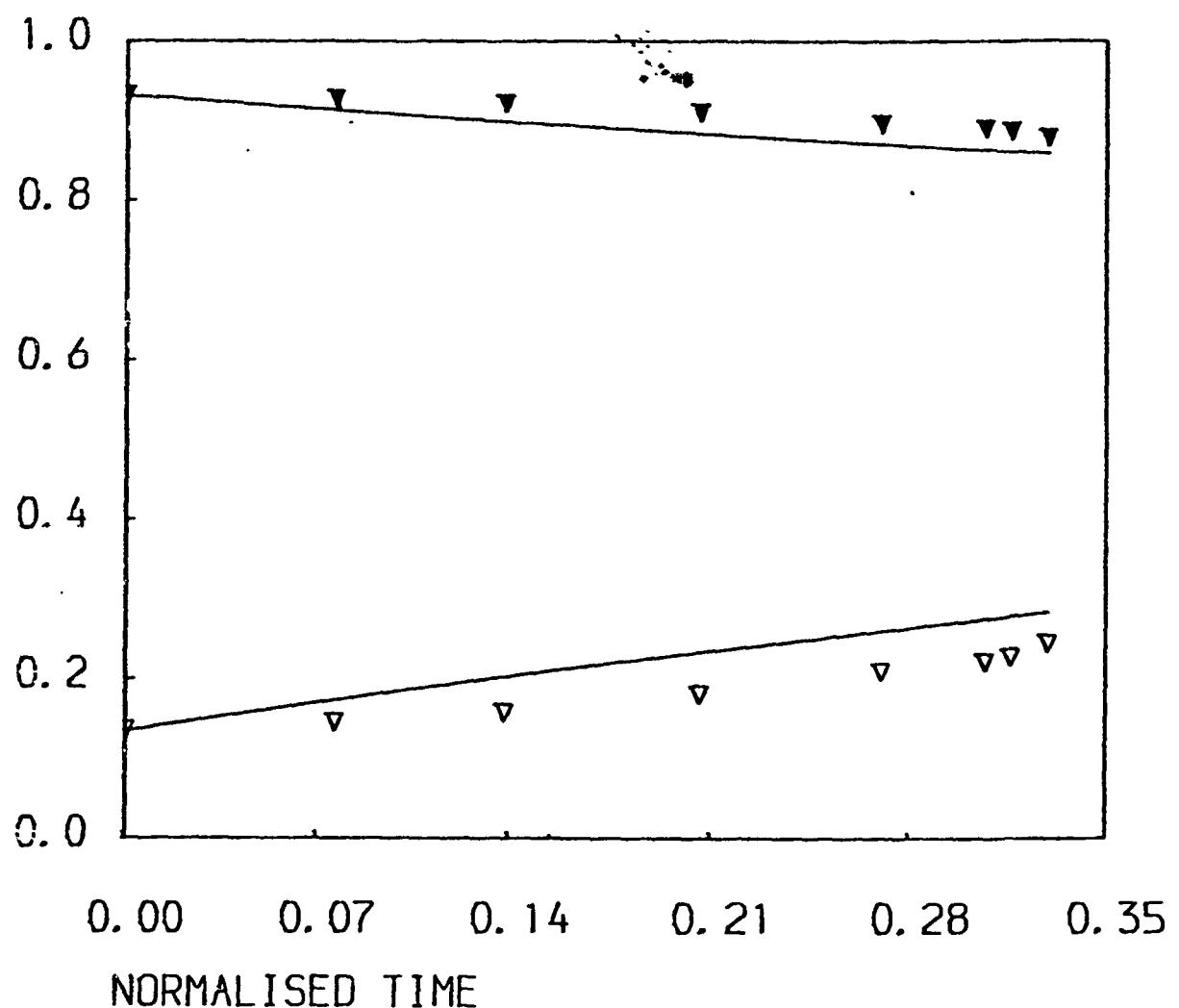


FIGURE 2 COMPARISON OF THE EVOLUTION OF THE REYNOLDS STRESS COMPONENTS IN THE UBEROI EXPERIMENT (1956) AS A FUNCTION OF THE NORMALISED TIME. LINEAR SOLUTION. (CONTRACTION RATIO 4:1, $R_M = 6150$; DATA:
 $\nabla \frac{v^2}{k} = \frac{w^2}{k}$ $\nabla \frac{u^2}{k}$).

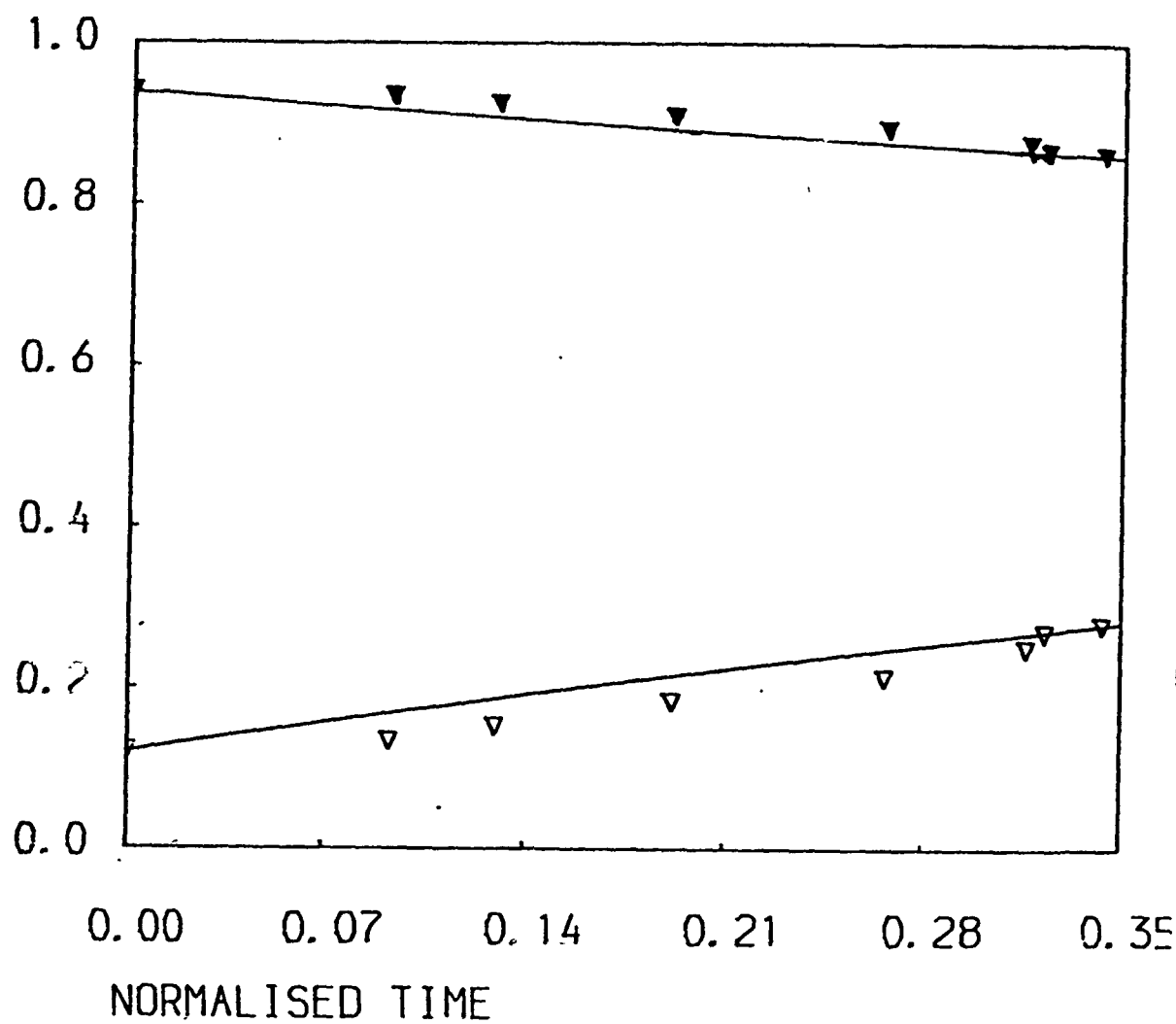


FIGURE 3 COMPARISON OF THE EVOLUTION OF THE REYNOLDS STRESS COMPONENTS IN THE UBEROI EXPERIMENT (1956) AS A FUNCTION OF THE NORMALISED TIME. LINEAR SOLUTION.
 (CONTRACTION RATIO 4:1, $R_M = 12300$; DATA:
 $\nabla \frac{\bar{v}^2}{k} = \frac{\bar{w}^2}{k}$ $\nabla \frac{\bar{u}^2}{k}$).

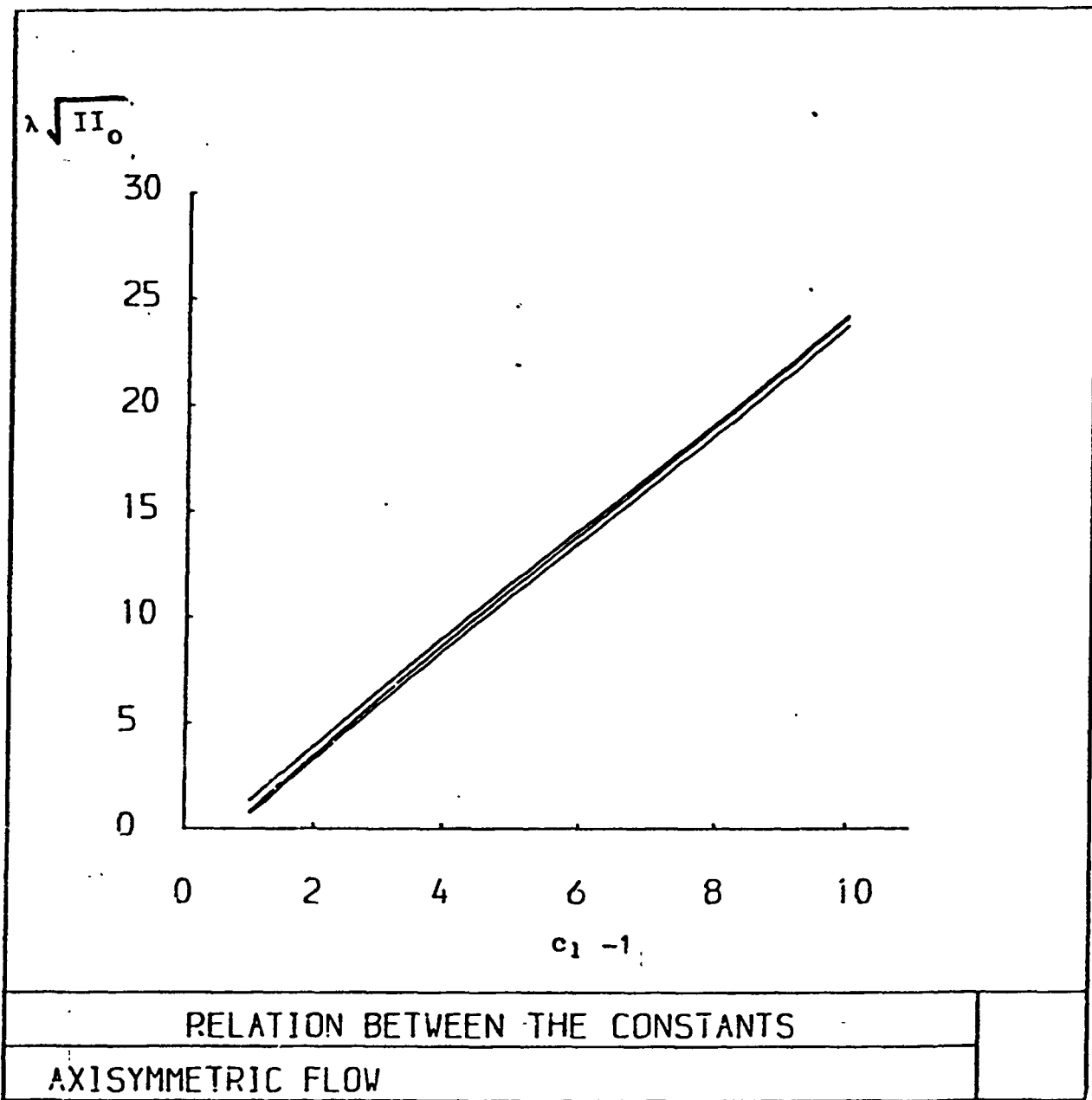


FIGURE 4

RELATION BETWEEN THE CONSTANTS CONNECTED TO THE LINEAR AND NON-LINEAR PART OF THE PRESSURE-STRAIN TERM FOR AXISYMMETRIC FLOWS, UBEROI EXPERIMENT (1956).

VARIATION OF $|\lambda \sqrt{II_0}|$ AGAINST $c_1 - 1$

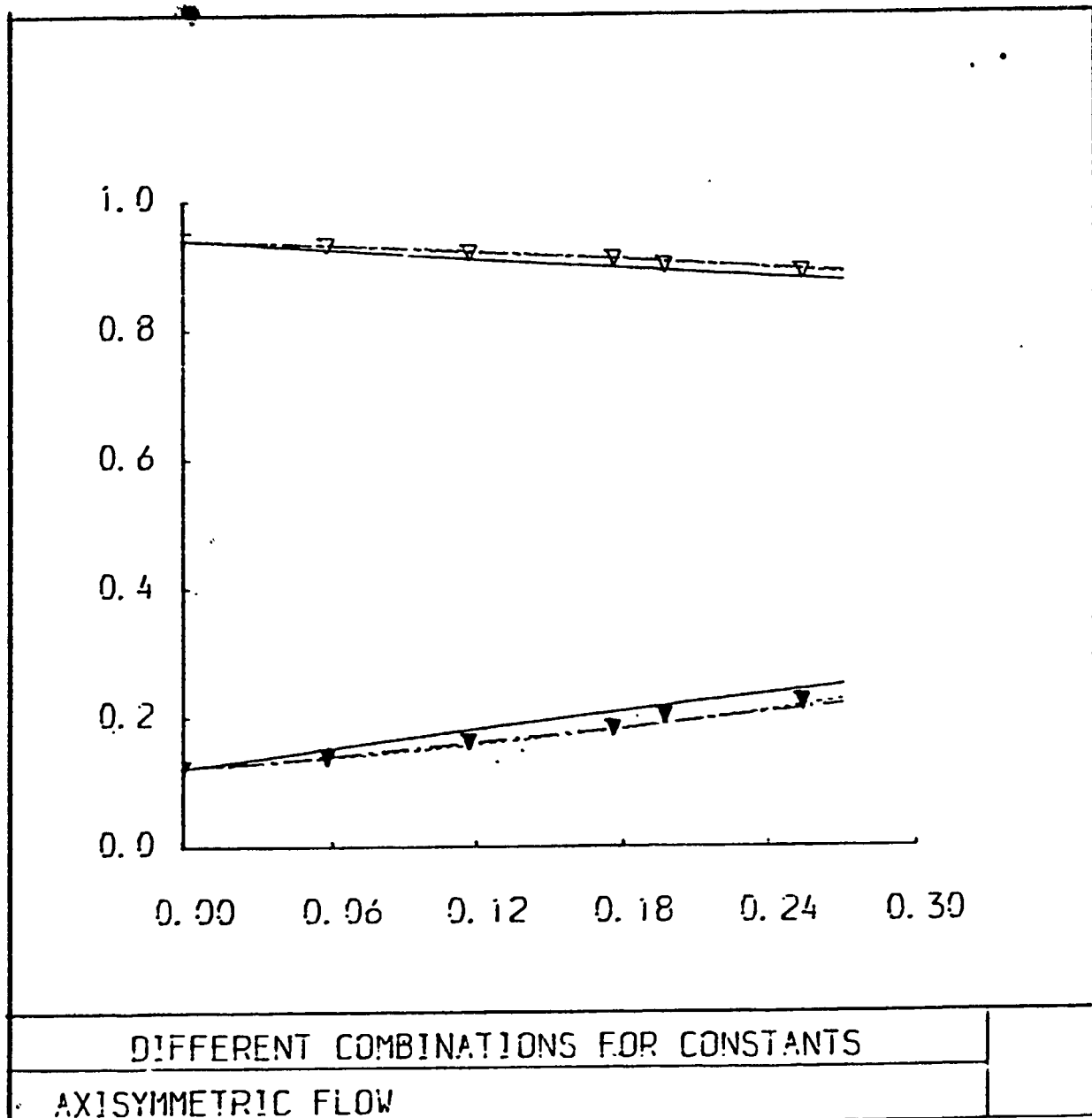


FIGURE 5 COMPARISON OF THE EVOLUTION OF THE REYNOLDS STRESS COMPONENTS AS A FUNCTION OF THE NORMALISED TIME, WITH VALUES OBTAINED FROM THE LINEAR AND NON-LINEAR ANALYTICAL SOLUTIONS USING DIFFERENT COMBINATIONS OF c_1 AND λ . (UBEROI EXPERIMENT (1956) CONTRACTIO RATIO 4:1, $R_M = 3710$, $\lambda < 0$, LINEAR —, NON-LINEAR - - - - - , - - - - - - -);

$$\text{DATA: } v \frac{\bar{v}^2}{k} = \frac{\bar{w}^2}{k}; \quad v \frac{\bar{u}^2}{k} \quad).$$

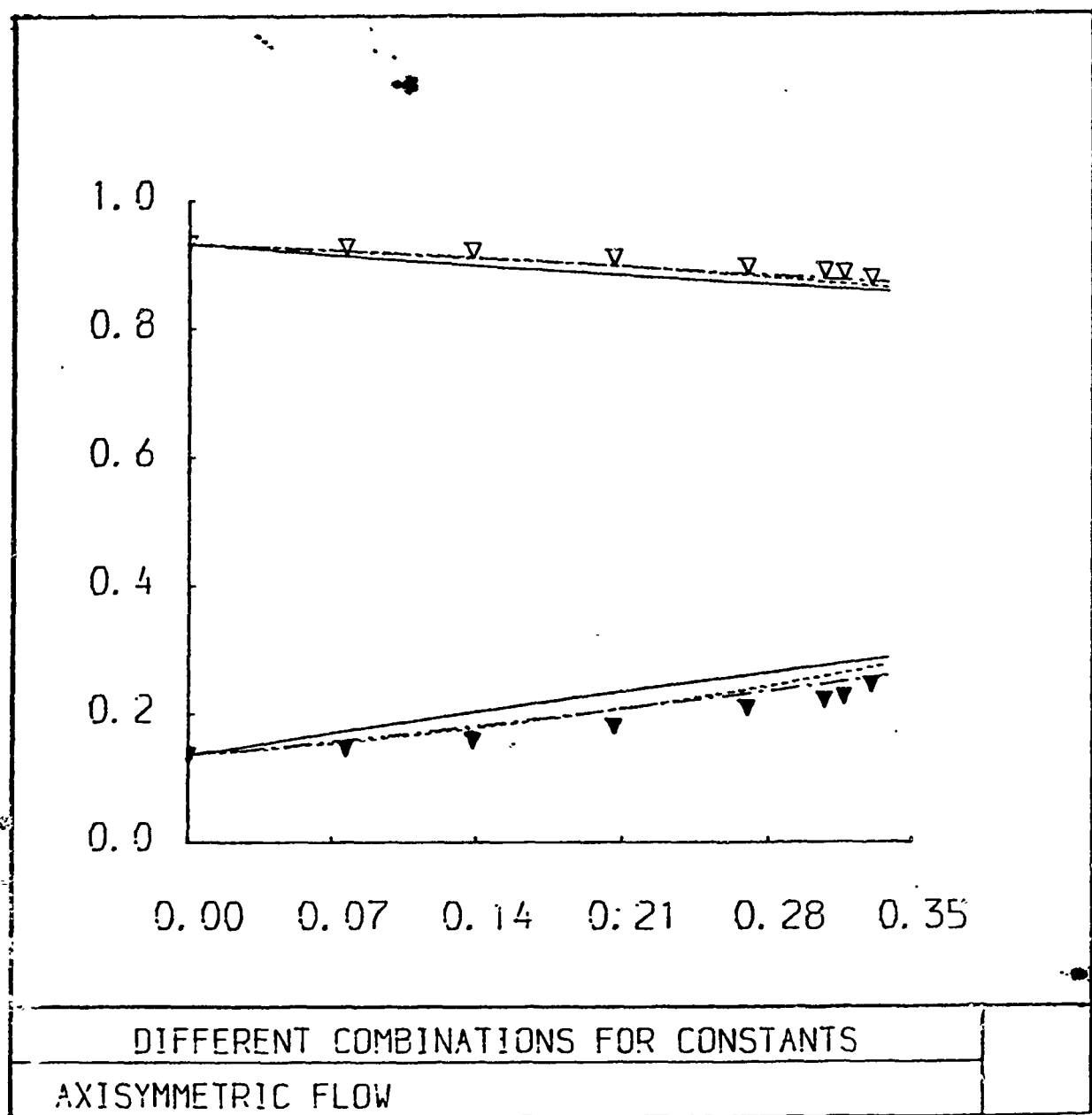


FIGURE 6

COMPARISON OF THE EVOLUTION OF THE REYNOLDS STRESS COMPONENTS AS A FUNCTION OF THE NORMALISED TIME, WITH VALUES OBTAINED FROM THE LINEAR AND NON-LINEAR ANALYTICAL SOLUTIONS, USING DIFFERENT COMBINATIONS OF c_1 AND λ . (UBEROI EXPERIMENT (1956), CONTRACTION RATIO 4:1, $R_M = 6150$, $\lambda < 0$, LINEAR —, NON-LINEAR - - - , - - - - -);

$$\text{DATA: } \nabla \frac{\bar{v}^2}{k} = \frac{\bar{w}^2}{k}; \quad \nabla \frac{\bar{u}^2}{k} .$$

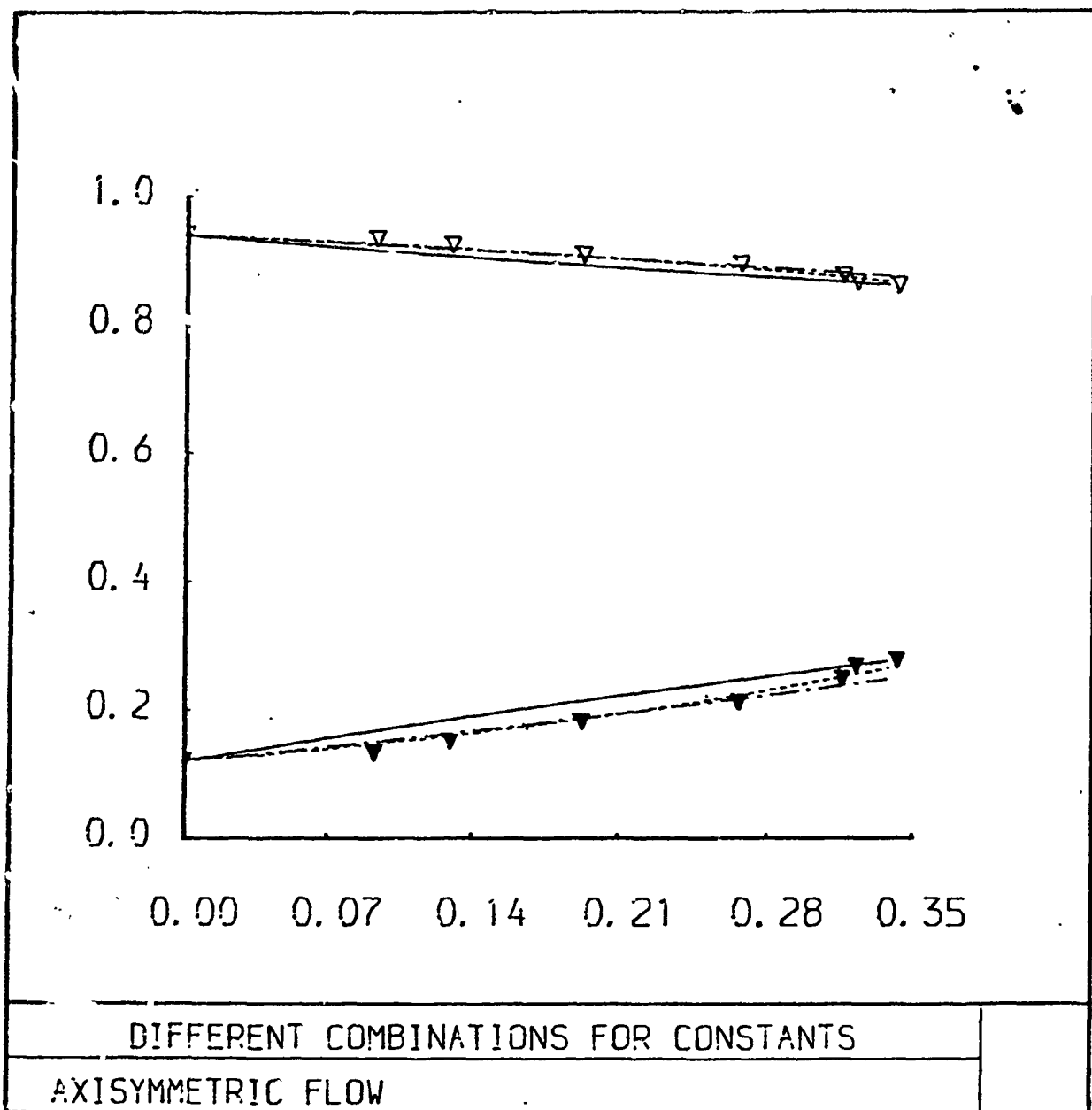


FIGURE 7 COMPARISON OF THE EVOLUTION OF THE REYNOLDS STRESS
 COMPONENTS AS A FUNCTION OF THE NORMALISED TIME,
 WITH VALUES OBTAINED FROM THE LINEAR AND NON-LINEAR
 ANALYTICAL SOLUTIONS, USING DIFFERENT COMBINATIONS
 OF c_1 AND λ . (UBEROI EXPERIMENT (1956), CONTRACTION
 RATIO 4:1, $R_M = 12,300$, $III < 0$, LINEAR — ,
 NON-LINEAR - - - - -)

$$\text{DATA: } v \frac{\bar{v}^2}{k} = \frac{\bar{w}^2}{k}; \quad v \frac{\bar{u}^2}{k}).$$

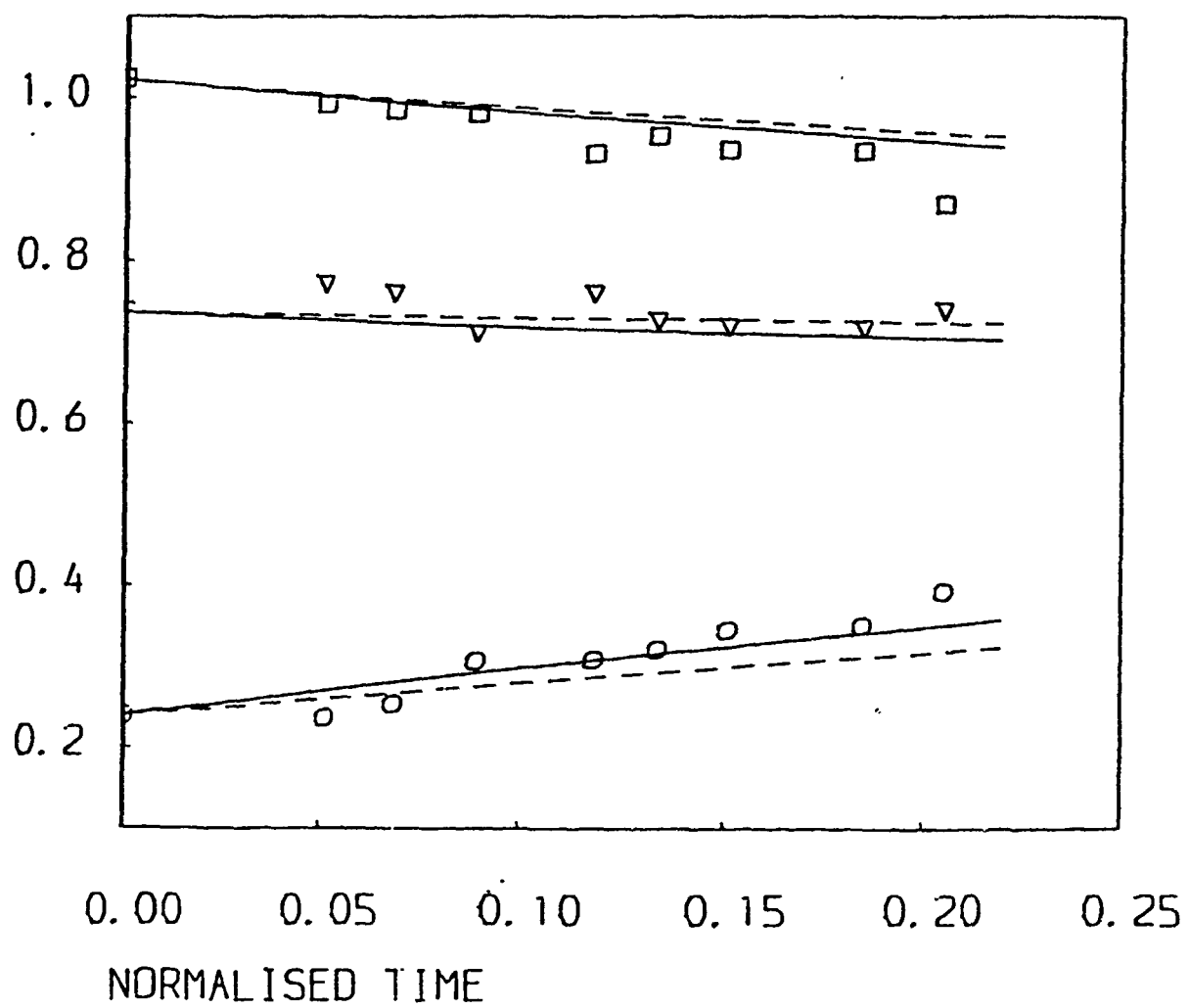


FIGURE 8(a) COMPARISON OF THE EVOLUTION OF THE REYNOLDS STRESS TENSOR AS A FUNCTION OF THE NORMALISED TIME IN THE TUCKER AND REYNOLDS EXPERIMENT (1968) WITH PREDICTIONS OBTAINED FROM THE LINEAR AND PERTURBATION SOLUTIONS (III<0; LINEAR - - -, NON-LINEAR ——).

DATA: $\nabla \frac{\bar{u}^2}{k}$; $\square \frac{\bar{v}^2}{k}$; $\circ \frac{\bar{w}^2}{k}$.

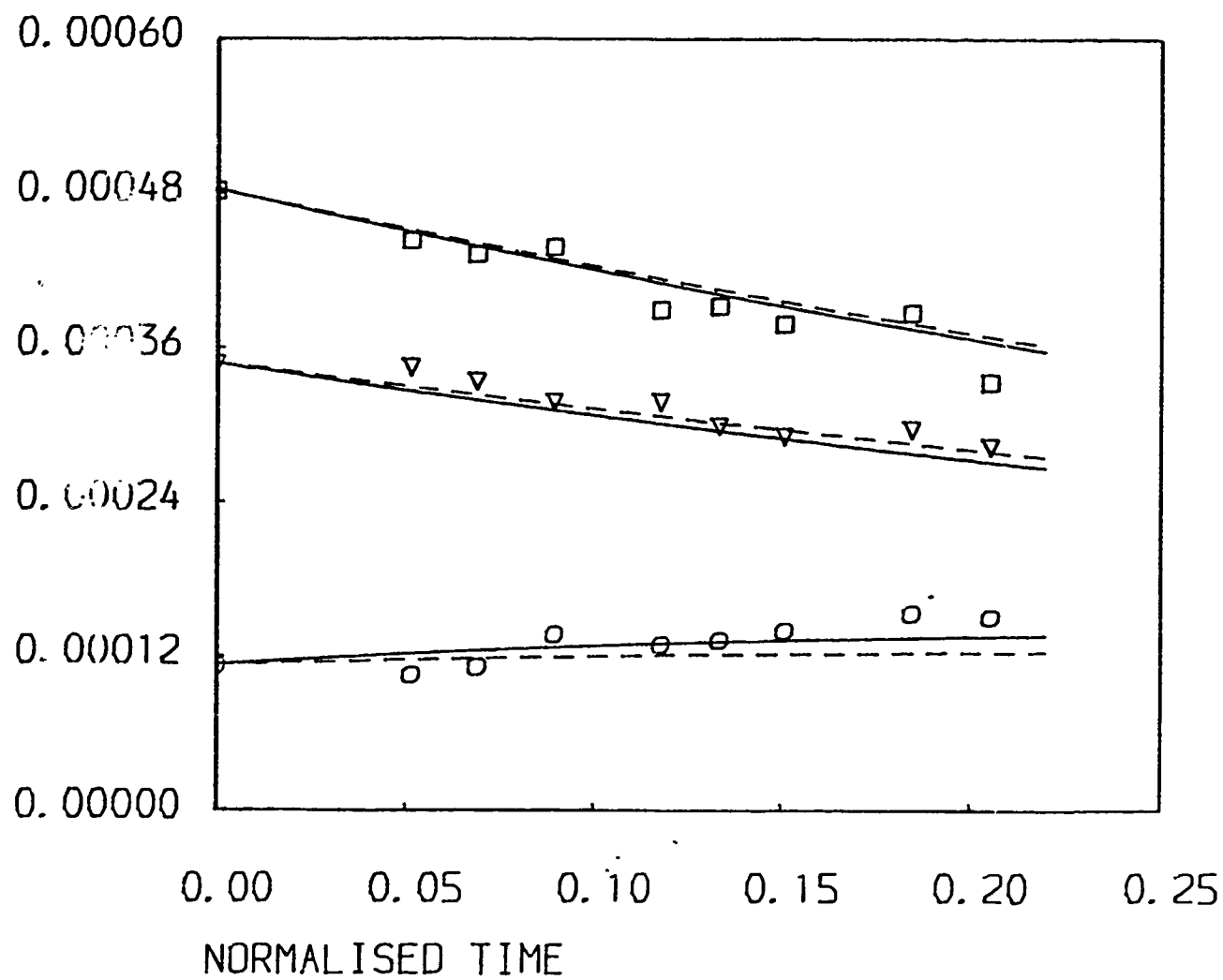


FIGURE 8(b) COMPARISON OF THE EVOLUTION OF THE REYNOLDS STRESS TENSOR AS A FUNCTION OF THE NORMALISED TIME IN THE TUCKER AND REYNOLDS EXPERIMENT (1968) WITH PREDICTIONS OBTAINED FROM THE LINEAR AND PERTURBATION SOLUTIONS (III<0; LINEAR- - -, NON-LINEAR-----,
 DATA: $\nabla \frac{\bar{u}^2}{\bar{U}^2}$; $\square \frac{\bar{v}^2}{\bar{U}^2}$; $\circ \frac{\bar{w}^2}{\bar{U}^2}$).

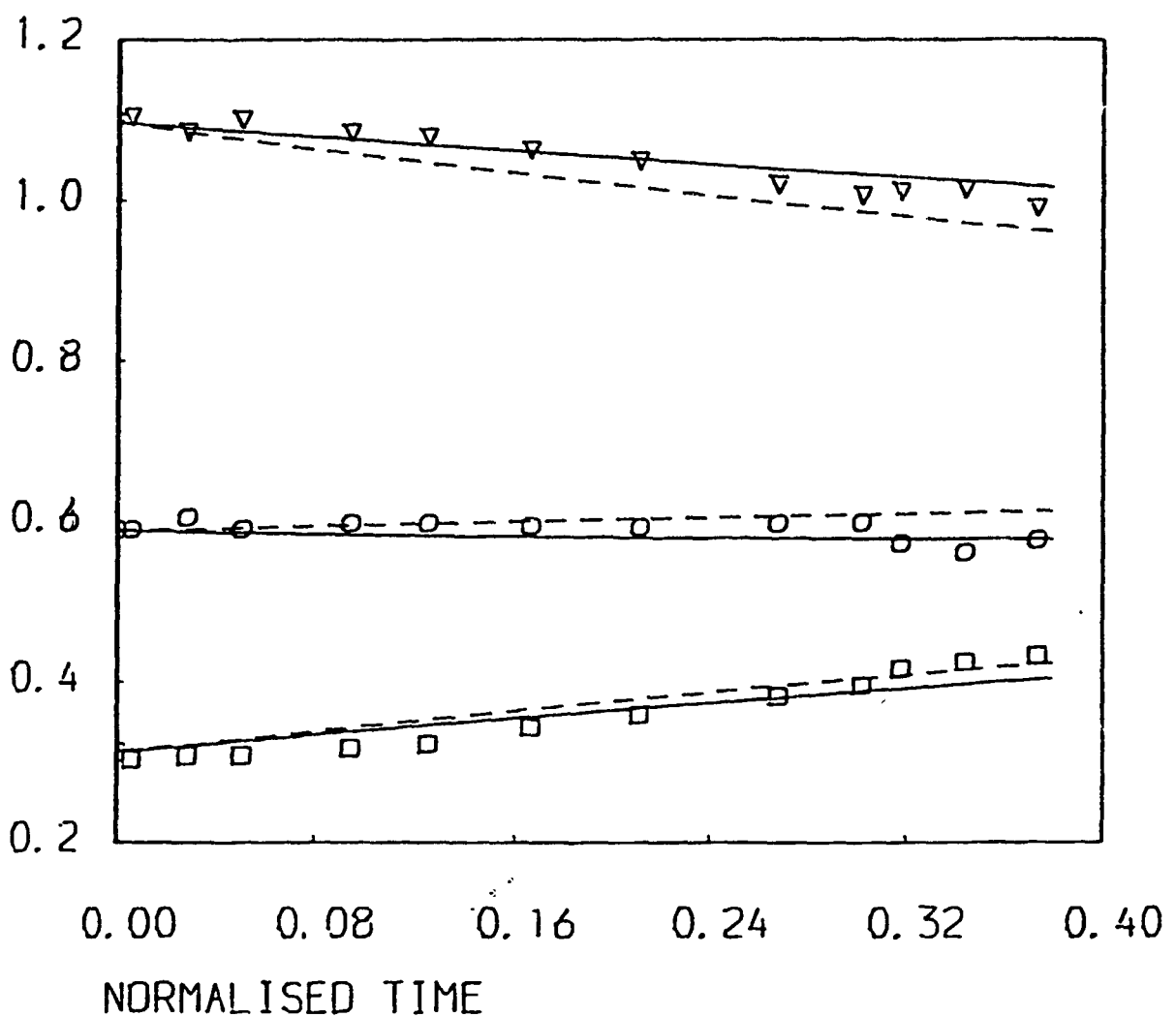


FIGURE 9(a) COMPARISON OF THE EVOLUTION OF THE REYNOLDS STRESS TENSOR AS A FUNCTION OF THE NORMALISED TIME IN THE GENCE AND MATHIEU EXPERIMENT (1980), WITH PREDICTIONS OBTAINED FROM THE LINEAR AND PERTURBATION SOLUTIONS ($\text{III} > 0$, $\alpha = 0$, LINEAR—, NON-LINEAR—).

DATA: $\circ \frac{\bar{u}^2}{k}$; $\square \frac{\bar{v}^2}{k}$; $\nabla \frac{\bar{w}^2}{k}$.

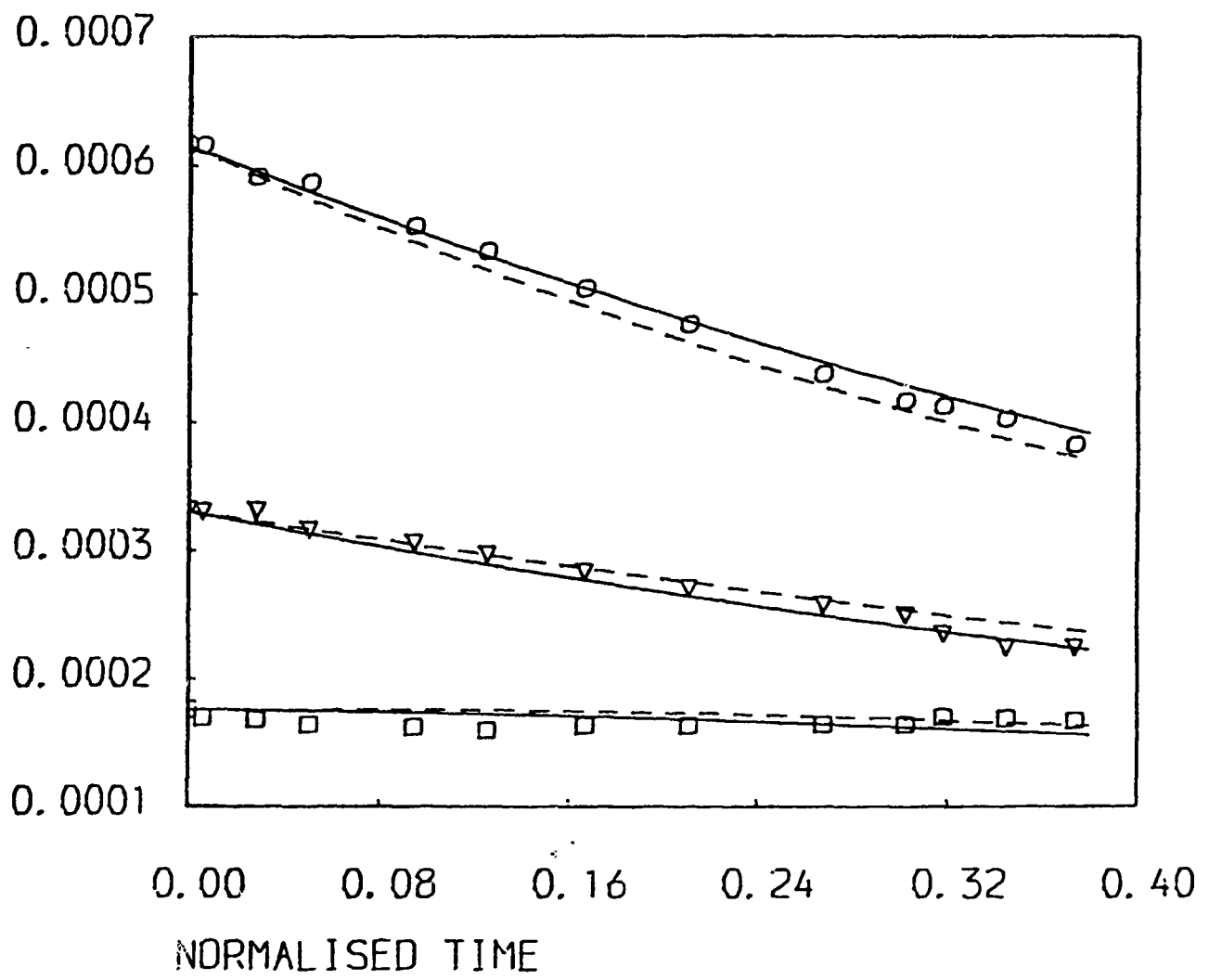


FIGURE 9(b) COMPARISON OF THE EVOLUTION OF THE REYNOLDS STRESS TENSOR AS A FUNCTION OF THE NORMALISED TIME IN THE GENCE AND MATHIEU EXPERIMENT (1980), WITH PREDICTIONS OBTAINED FROM THE LINEAR AND PERTURBATION SOLUTIONS ($\beta \gg 0$, $\alpha = 0$, LINEAR - - -, NON-LINEAR - - -).

DATA: $v\bar{u}^2/U^2$; $w\bar{u}^2/U^2$; \bar{u}^2/U^2 .

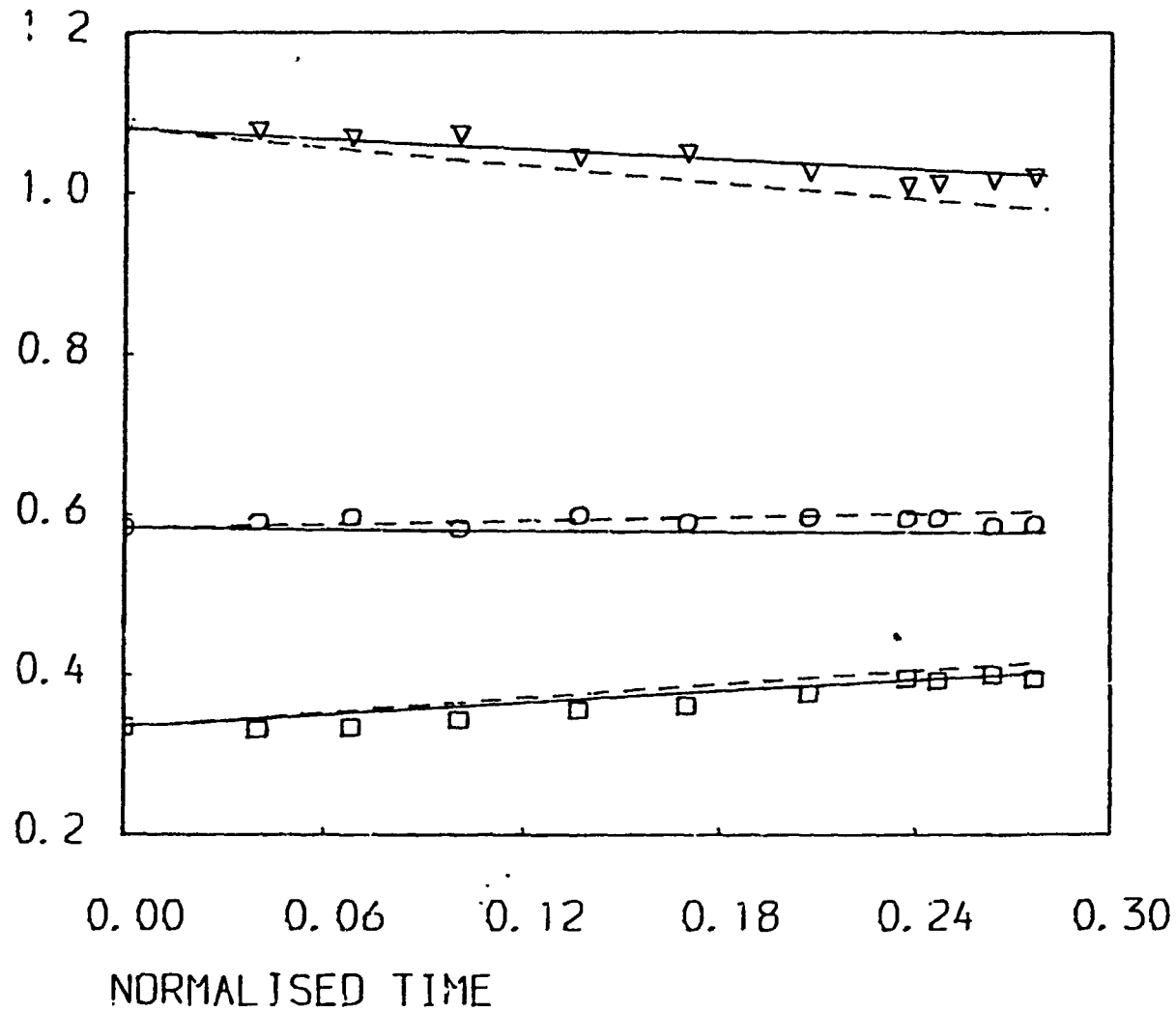


FIGURE 10(a) COMPARISON OF THE EVOLUTION OF THE REYNOLDS STRESS TENSOR (PRINCIPAL COMPONENTS) AGAINST THE NORMALISED TIME IN THE GENCE AND MATHIEU EXPERIMENT (1980), WITH PREDICTIONS OBTAINED FROM THE LINEAR AND PERTURBATION SOLUTIONS ($\text{III} > 0$, $\alpha = \frac{\pi}{4}$),
 LINEAR - - -, NON-LINEAR —,
 DATA: $\circ \frac{\bar{u}^2}{k}$; $\square \frac{\bar{v}^2}{k}$; $\nabla \frac{\bar{w}^2}{k}$)

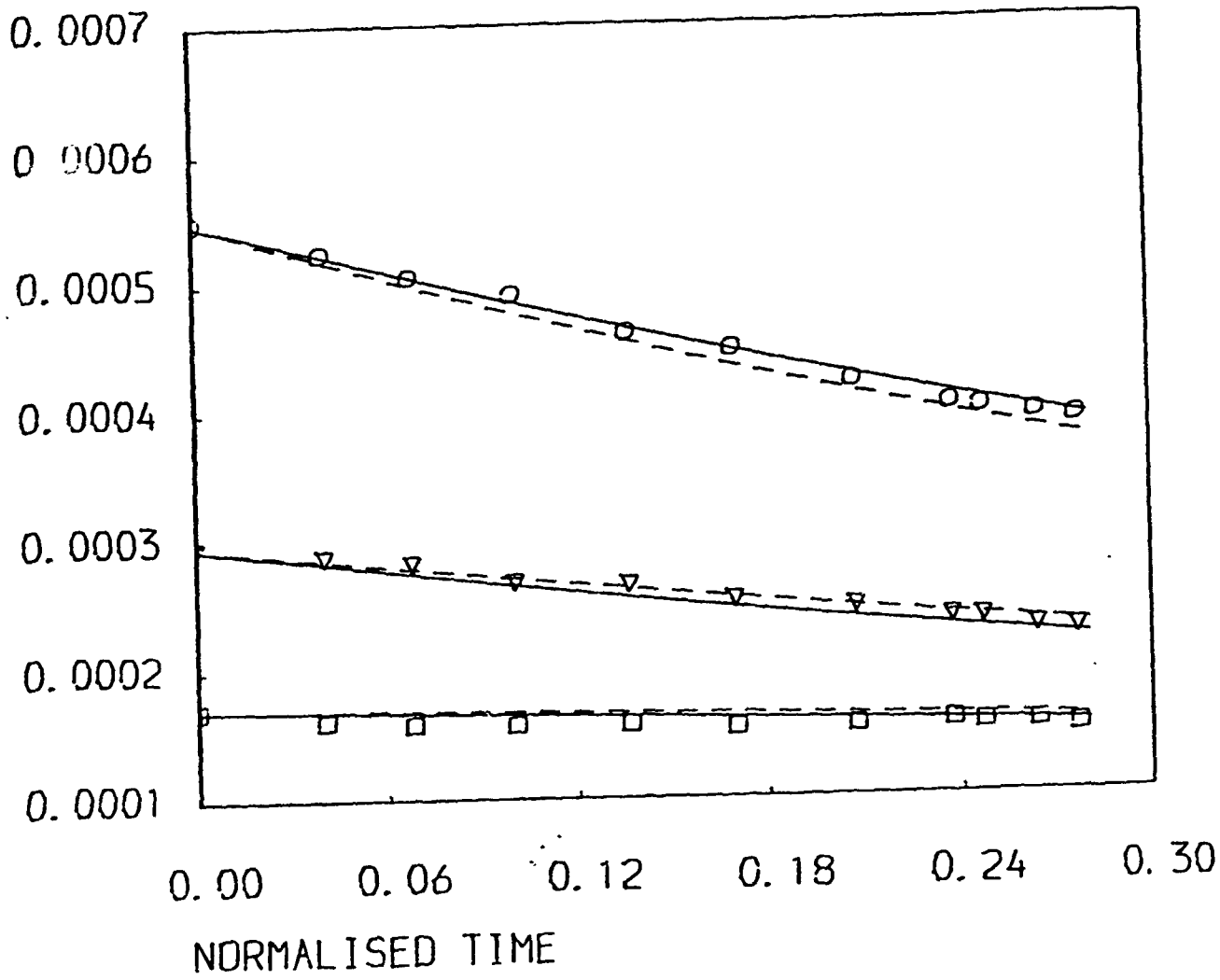


FIGURE 10(b) COMPARISON OF THE EVOLUTION OF THE REYNOLDS STRESS TENSOR (PRINCIPAL COMPONENTS) AGAINST THE NORMALISED TIME IN THE GENCE AND MATHIEU EXPERIMENT (1980), WITH PREDICTIONS OBTAINED FROM THE "NEAR AND PERTURBATION" SOLUTIONS ($\bar{u}^2_p > 0$, $\frac{\pi}{4}$, LINEAR - - -, NON-LINEAR ——),
 DATA: $\nabla \bar{u}^2_p / U^2$; $\square \bar{v}^2_p / U^2$; $\circ \bar{w}^2_p / U^2$.

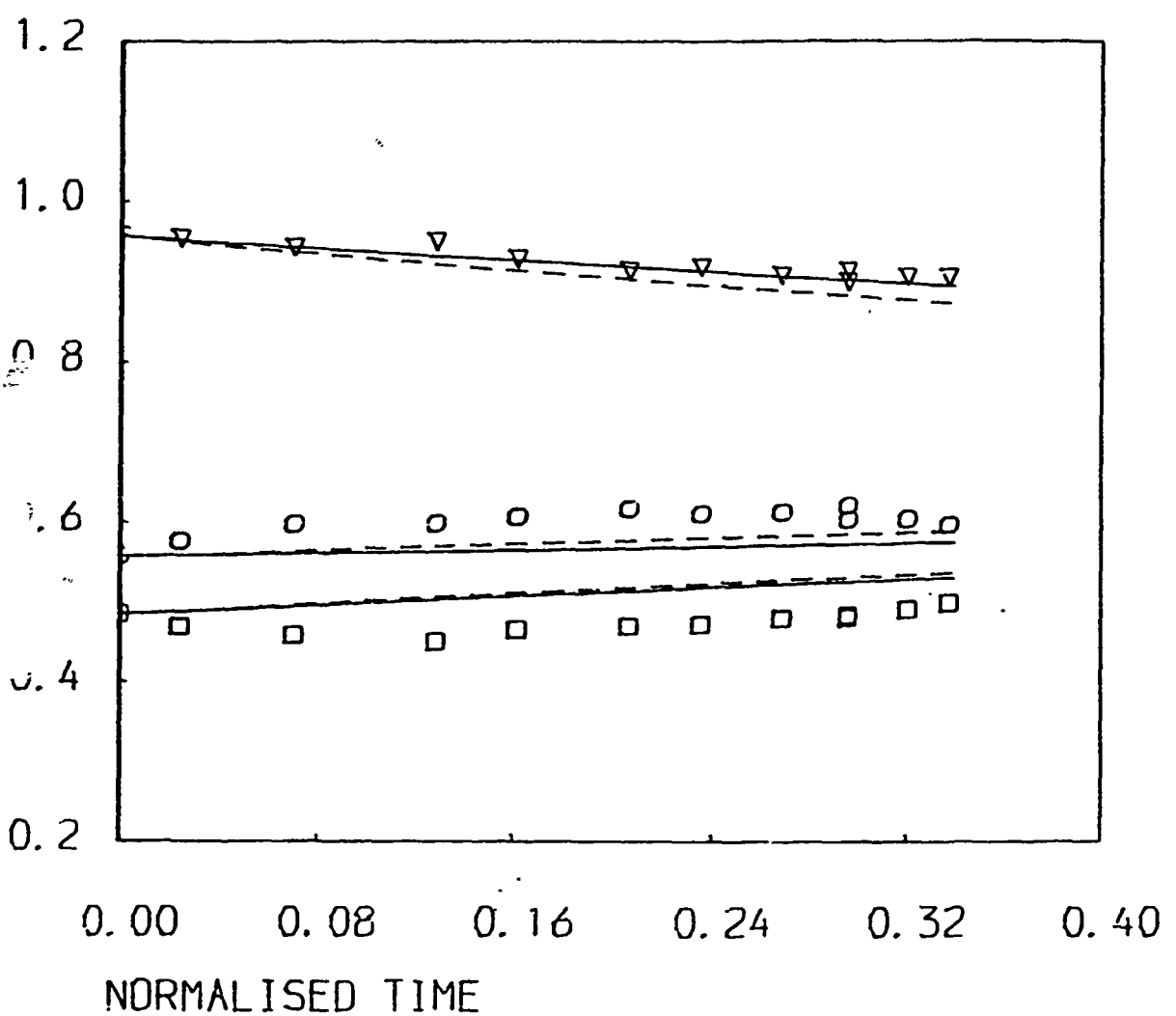


FIGURE 11(a) COMPARISON OF THE EVOLUTION OF THE REYNOLDS STRESS TENSOR (PRINCIPAL COMPONENTS) AGAINST THE NORMALISED TIME in THE GENCE AND MATHIEU EXPERIMENT (1980), WITH PREDICTIONS OBTAINED FROM THE LINEAR AND PERTURBATION SOLUTIONS ($\text{III} > 0$, $\alpha = \frac{3}{4}\pi$, LINEAR - - -, NON-LINEAR ——),
 DATA: $\circ \frac{u^2}{k}$; $\square \frac{v^2}{k}$; $\nabla \frac{w^2}{k}$).

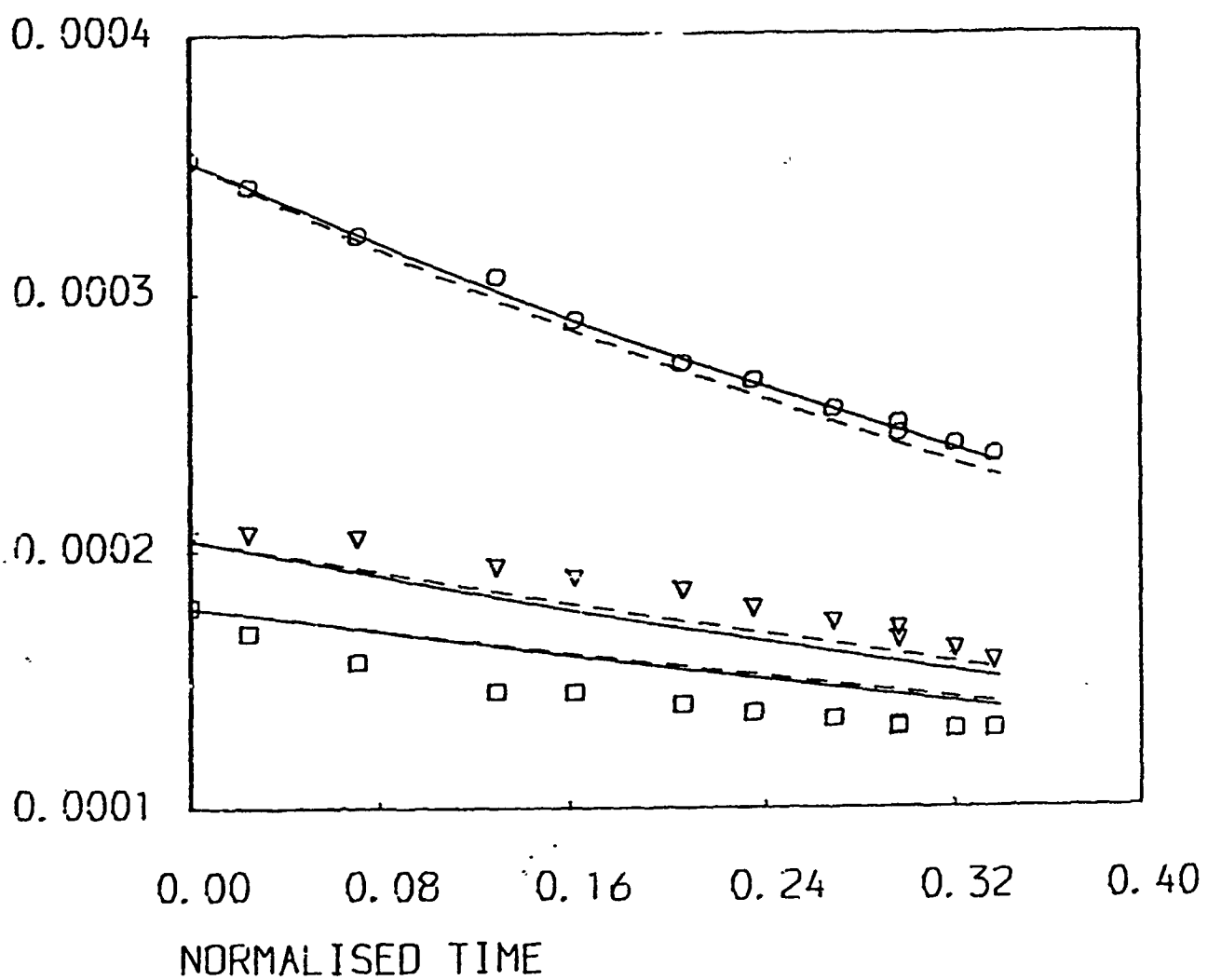


FIGURE 11(b) COMPARISON OF THE EVOLUTION OF THE REYNOLDS STRESS TENSOR (PRINCIPAL COMPONENTS) AGAINST THE NORMALISED TIME IN THE GENCE AND MATHIEU EXPERIMENT (1980), WITH PREDICTIONS OBTAINED FROM THE LINEAR AND PERTURBATION SOLUTIONS ($\text{III} > 0$, $\alpha = \frac{3}{4}\pi$),
 LINEAR - - -, NON-LINEAR —————,
 DATA: $\nabla \frac{\bar{v}^2}{\bar{u}^2}$; $\square \frac{\bar{w}^2}{\bar{u}^2}$; $\circ \frac{\bar{u}^2}{\bar{u}^2}$).

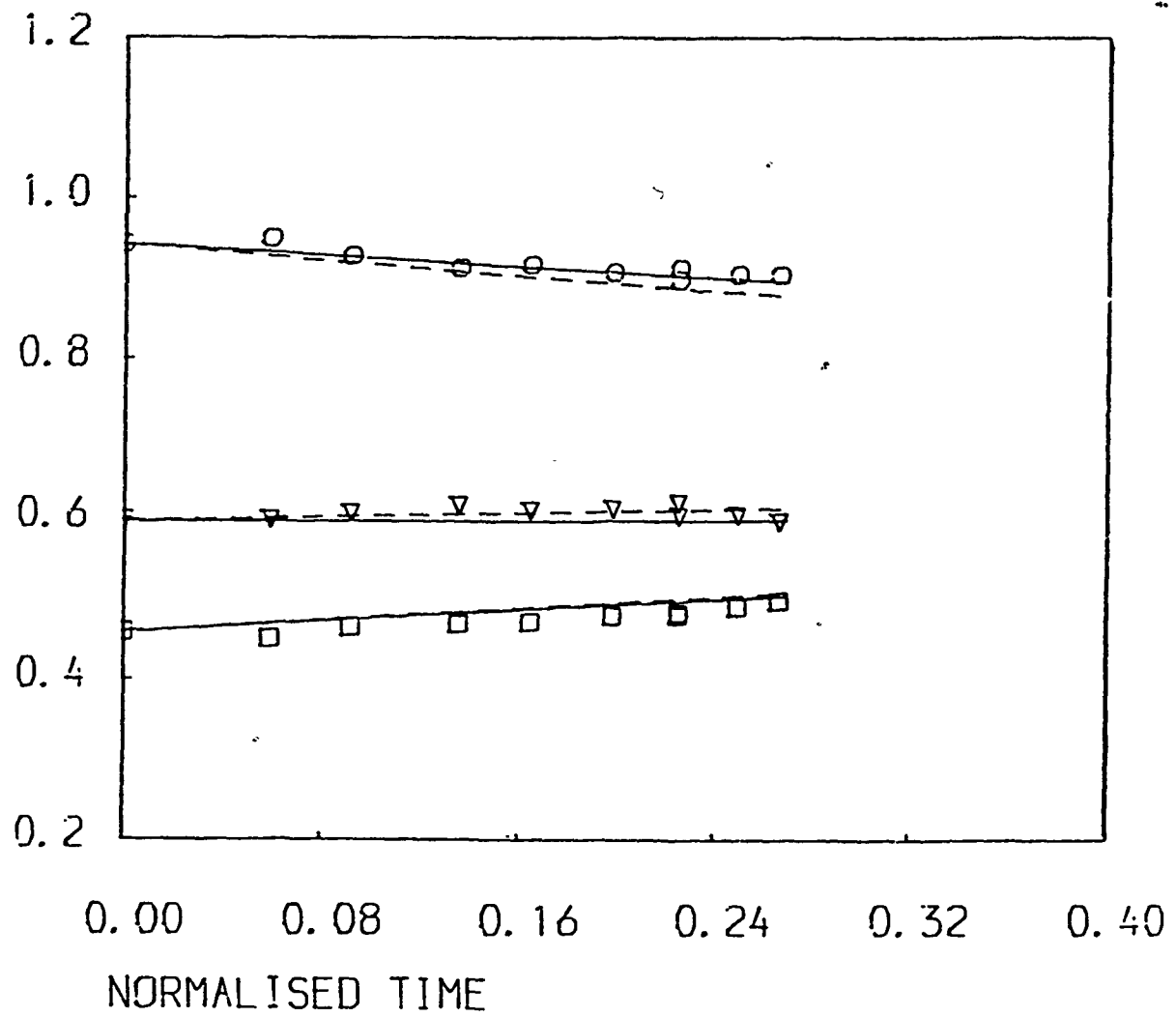


FIGURE 11.1(a) COMPARISON OF THE EVOLUTION OF THE REYNOLDS STRESS TENSOR (PRINCIPAL COMPONENTS) AGAINST THE NORMALISED TIME IN THE GENCE AND MATHIEU EXPERIMENT (1980), WITH PREDICTIONS OBTAINED FROM THE LINEAR AND PERTURBATION SOLUTIONS. THE INITIAL NORMALISED TIME HAS BEEN SHIFTED TO THE POINT WHERE THE ANISOTROPY STARTS TO DECAY SMOOTHLY.
 ($\text{III} > 0$, $\alpha = \frac{3}{4}\pi$, LINEAR - - - - -, NON-LINEAR - - -)

DATA: $\nabla \frac{\bar{u}^2}{k}$; $\square \frac{\bar{v}^2}{k}$; $\circ \frac{\bar{w}^2}{k}$).

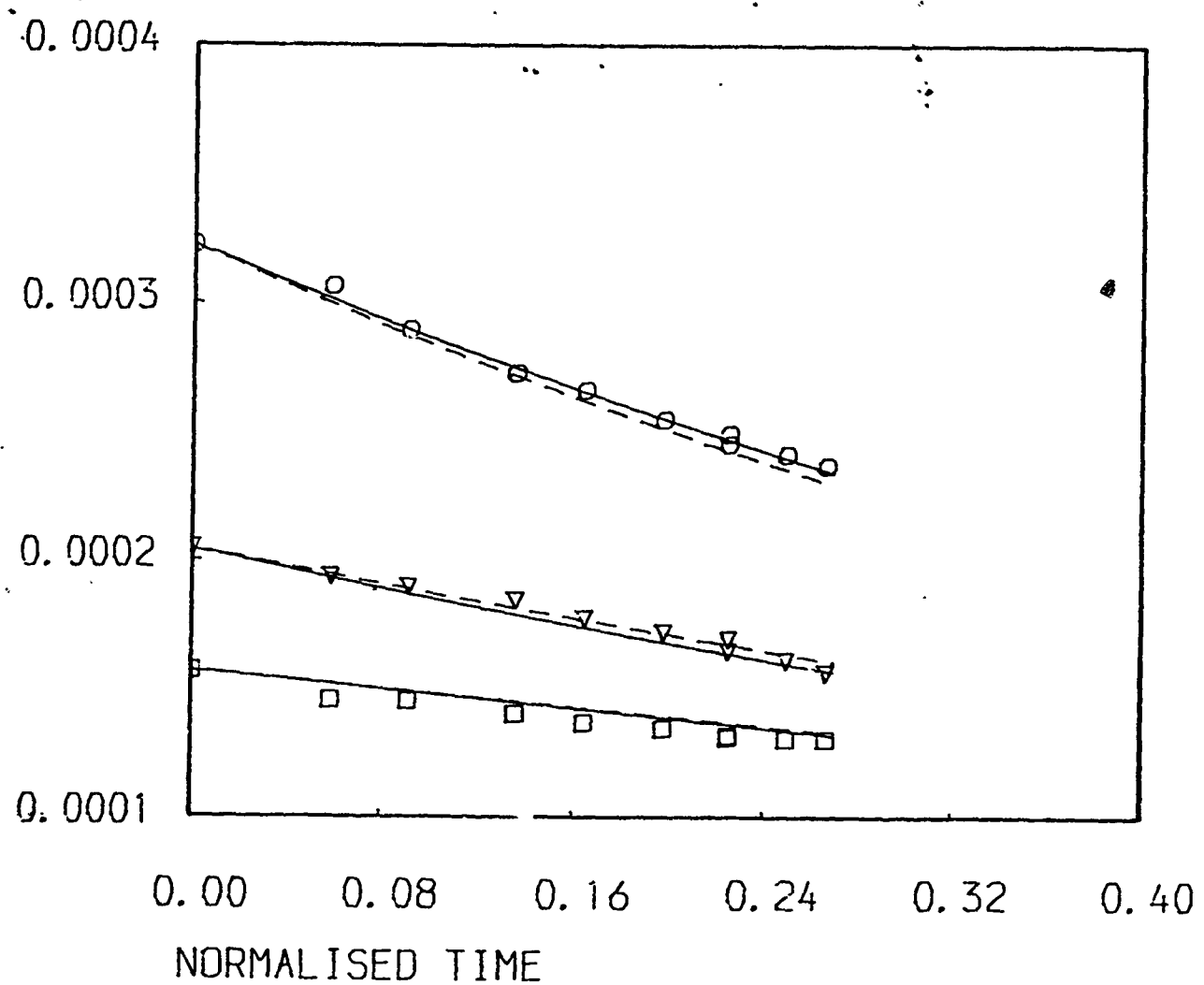


FIGURE 11.1(b) COMPARISON OF THE EVOLUTION OF THE REYNOLDS STRESS TENSOR (PRINCIPAL COMPONENTS) AGAINST THE NORMALISED TIME IN THE GENCE AND MATHIEU EXPERIMENT (1980), WITH PREDICTIONS OBTAINED FROM THE LINEAR AND PERTURBATION SOLUTIONS. THE INITIAL NORMALISED TIME HAS BEEN SHIFTED TO THE POINT WHERE THE ANISOTROPY STARTS TO DECAY SMOOTHLY.

($\langle III \rangle > 0$, $\alpha = \frac{3}{4}\pi$, LINEAR - - - -, NON-LINEAR -----,
 DATA: $\nabla \frac{\bar{u}^2}{\bar{u}^2}$; $\square \frac{\bar{v}^2}{\bar{u}^2}$; $\circ \frac{\bar{w}^2}{\bar{u}^2}$).

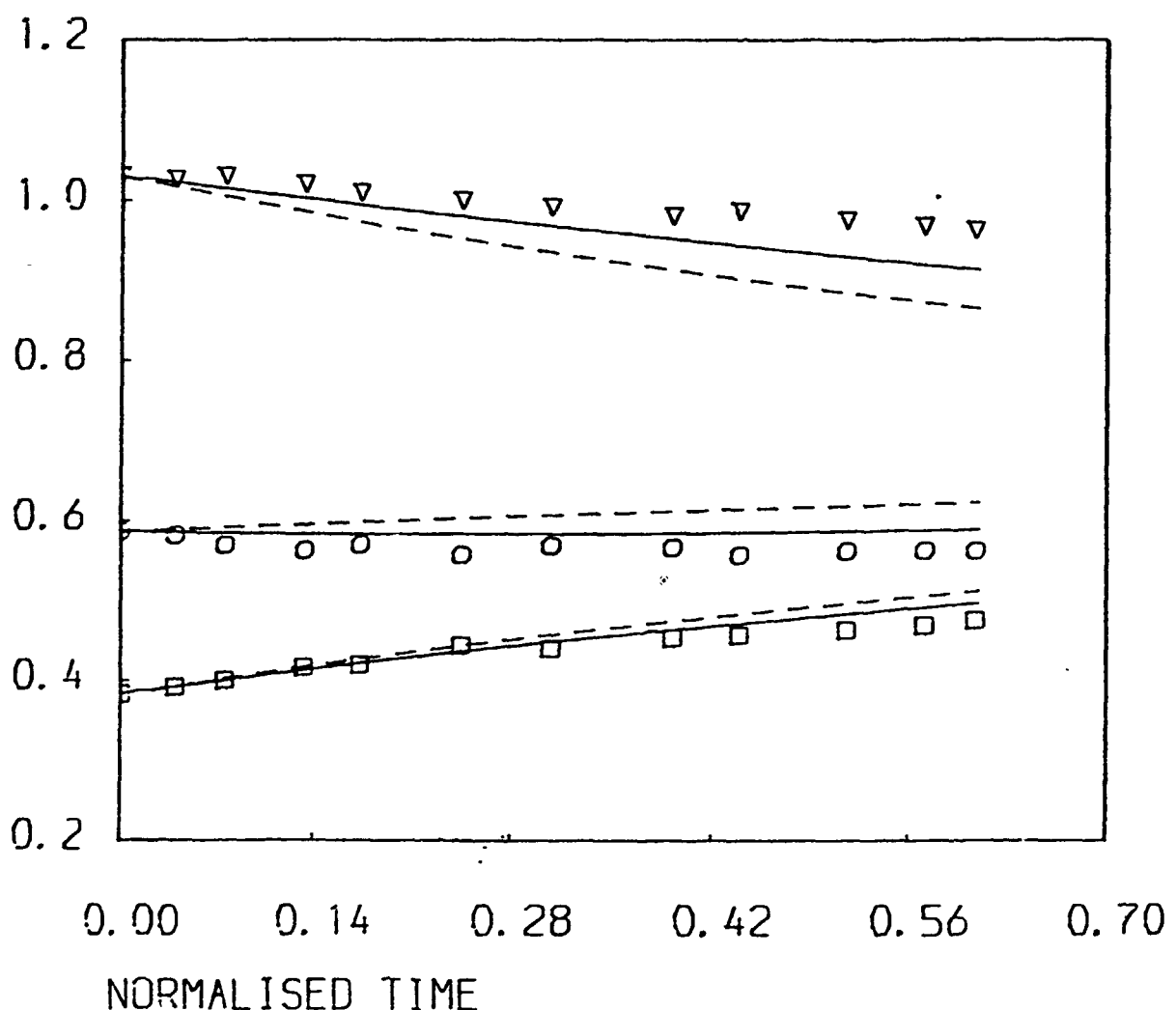


FIGURE 12(a) COMPARISON OF THE EVOLUTION OF THE REYNOLDS STRESS COMPONENTS AGAINST THE NORMALISED TIME IN THE LE PENVEN ET AL. EXPERIMENT (1984), WITH PREDICTIONS OBTAINED FROM THE LINEAR AND PERTURBATION SOLUTIONS. ($\frac{u^2}{k} > 0$, LINEAR - - - -, NON-LINEAR ——).

DATA: $\square \frac{u^2}{k}$; $\circ \frac{v^2}{k}$; $\nabla \frac{w^2}{k}$.

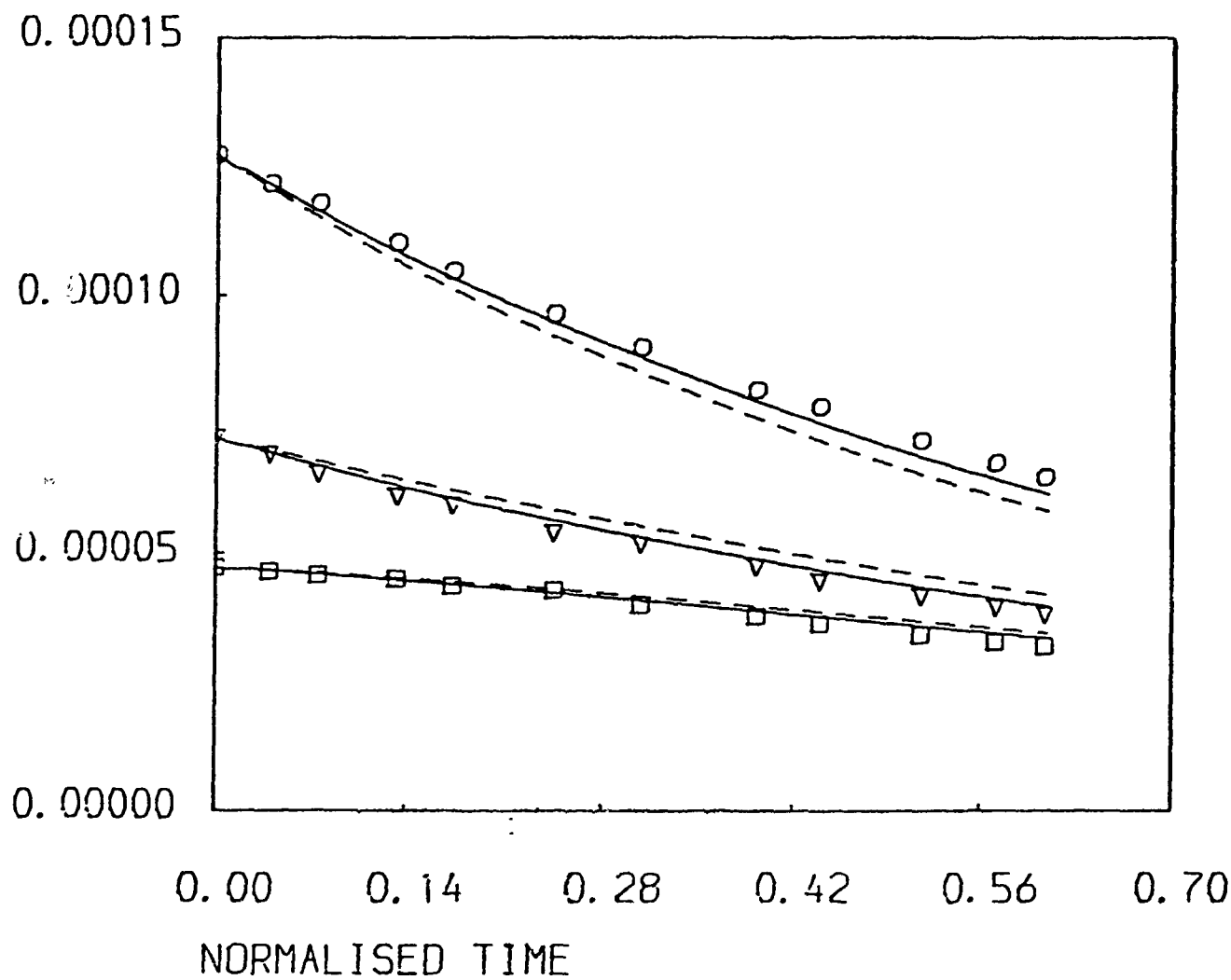


FIGURE 12(b) COMPARISON OF THE EVOLUTION OF THE REYNOLDS STRESS TENSOR AGAINST THE NORMALISED TIME IN THE LE PENVEN ET AL. EXPERIMENT (1984), WITH PREDICTIONS OBTAINED FROM THE LINEAR AND PERTURBATION SOLUTIONS.
 ($\bar{u}^2 / \bar{U}^2 > 0$, LINEAR- - -, NON-LINEAR—),
 DATA: $\square \frac{\bar{u}^2}{\bar{U}^2}$; $\nabla \frac{\bar{v}^2}{\bar{U}^2}$; $\circ \frac{\bar{w}^2}{\bar{U}^2}$).

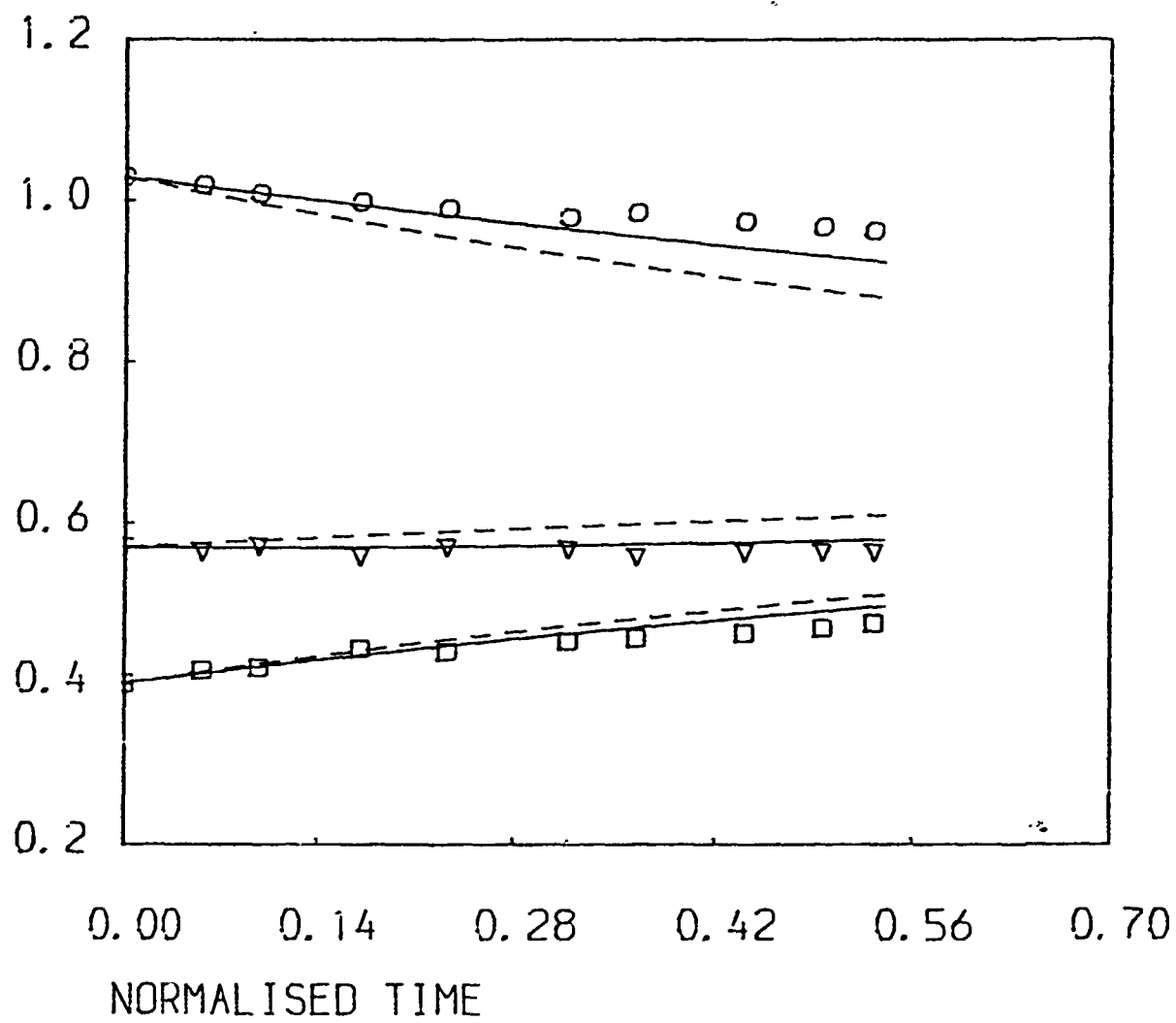


FIGURE 12.1(a) COMPARISON OF THE EVOLUTION OF THE REYNOLDS STRESS TENSOR AGAINST THE NORMALISED TIME IN THE LE PENVEN ET AL. EXPERIMENT (1984), WITH PREDICTIONS OBTAINED FROM THE LINEAR AND PERTURBATION SOLUTIONS. THE INITIAL NORMALISED TIME HAS BEEN SHIFTED TO THE POINT WHERE THE ANISOTROPY STARTS TO DECAY SMOOTHLY. ($\bar{u}^2/k > 0$, LINEAR- - - -, NON-LINEAR—).

DATA: $\square \frac{\bar{u}^2}{k}$; $\nabla \frac{\bar{v}^2}{k}$; $\circ \frac{\bar{w}^2}{k}$).

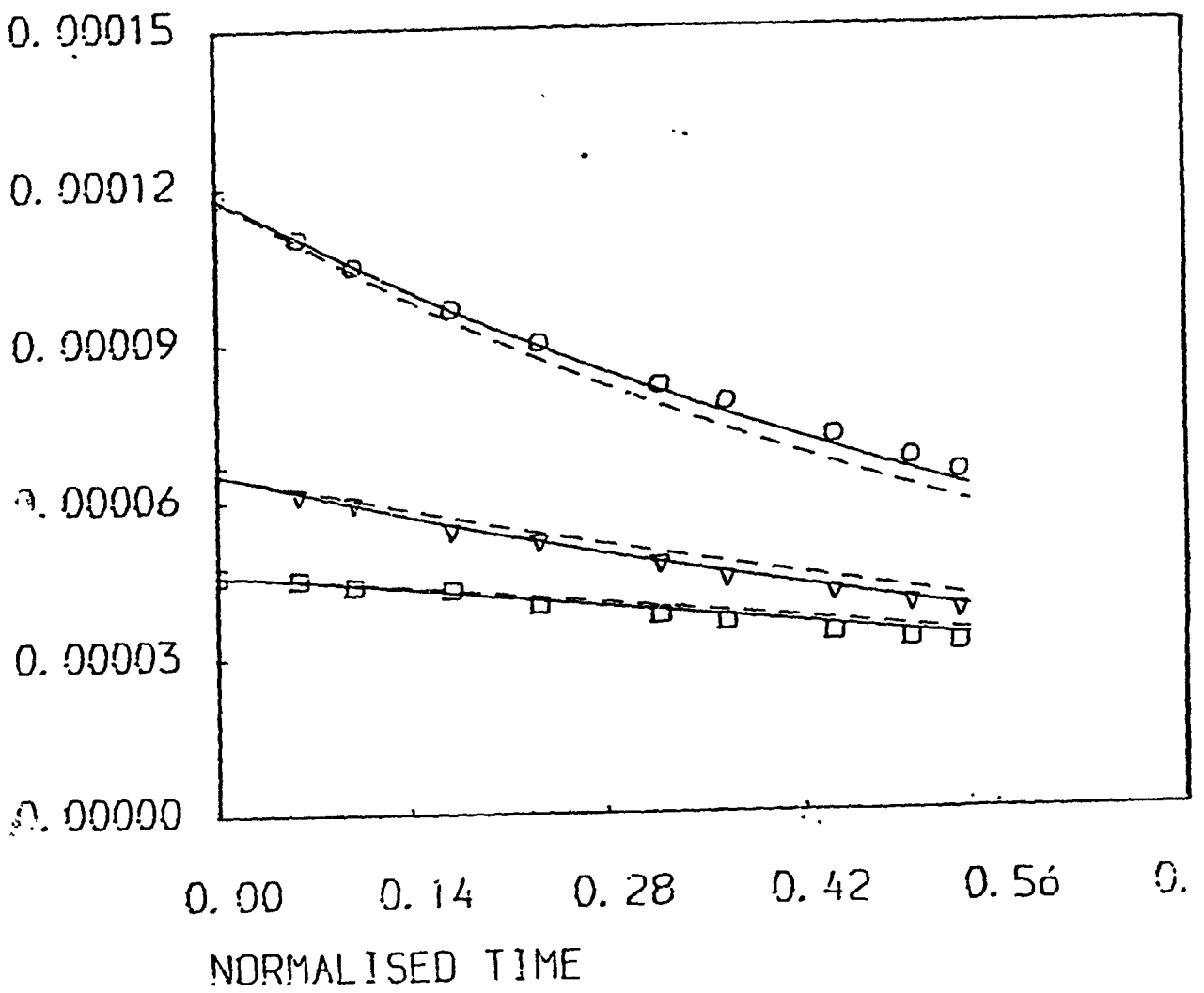


FIGURE 12.1(b) COMPARISON OF THE EVOLUTION OF THE REYNOLDS STRESS TENSOR AGAINST THE NORMALISED TIME IN THE LE PENVEN ET AL. EXPERIMENT (1984), WITH PREDICTIONS OBTAINED FROM THE LINEAR AND PERTURBATION SOLUTIONS. THE INITIAL NORMALISED TIME HAS BEEN SHIFTED TO THE POINT WHERE THE ANISOTROPY STARTS TO DECAY SMOOTHLY. ($\bar{u}^2 > 0$, LINEAR- - -, NON-LINEAR—).

DATA: $\square \frac{\bar{u}^2}{\bar{U}^2}$; $\nabla \frac{\bar{v}^2}{\bar{U}^2}$; $\circ \frac{\bar{w}^2}{\bar{U}^2}$.

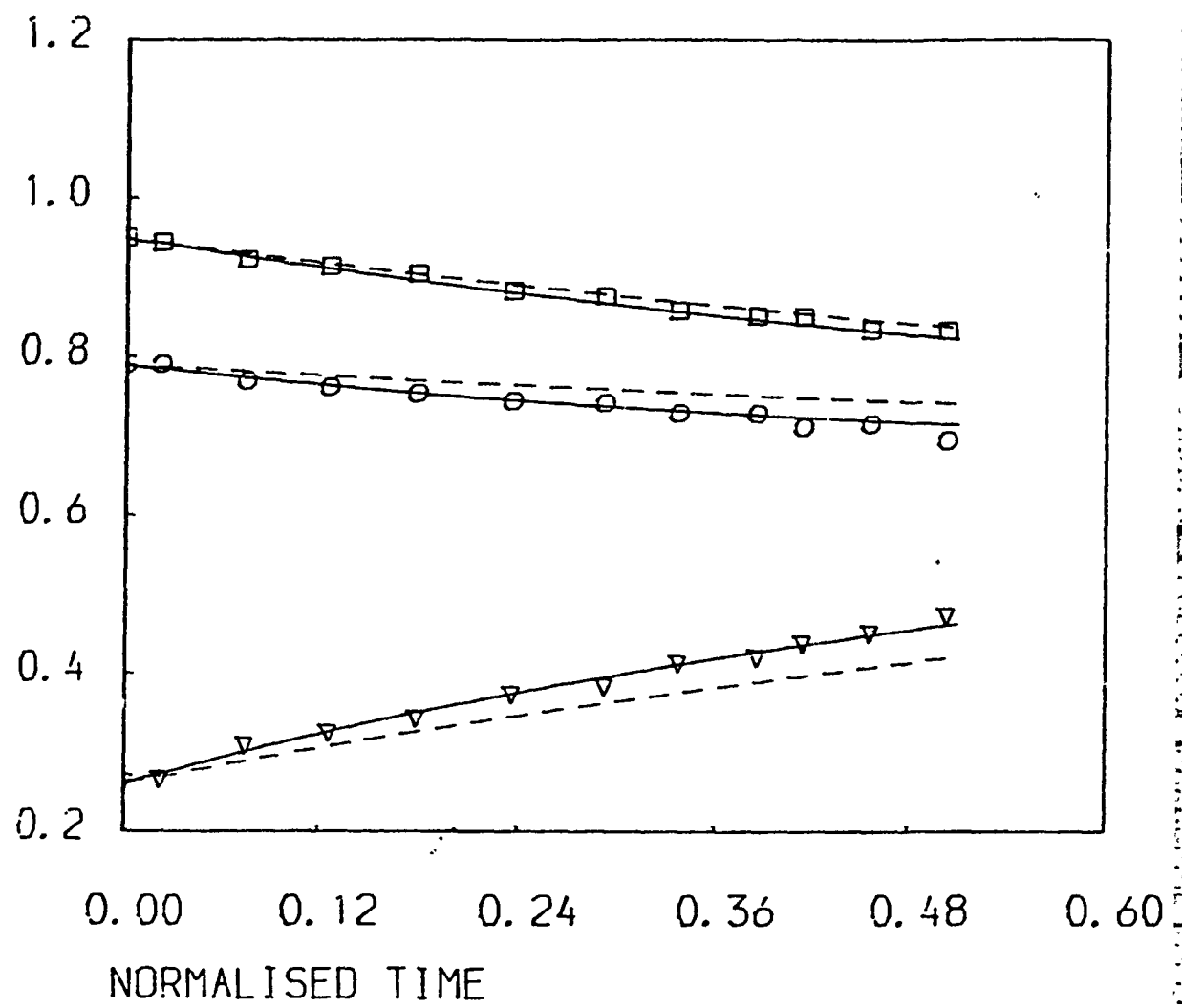


FIGURE 13(a) COMPARISON OF THE EVOLUTION OF THE REYNOLDS STRESS TENSOR AGAINST THE NORMALISED TIME IN THE LE PENVEN ET AL. EXPERIMENT (1984), WITH PREDICTIONS OBTAINED FROM THE LINEAR AND PERTURBATION SOLUTIONS (III < 0, LINEAR - - -, NON-LINEAR ——),
 DATA: \bar{u}^2/k ; \bar{v}^2/k ; \bar{w}^2/k .

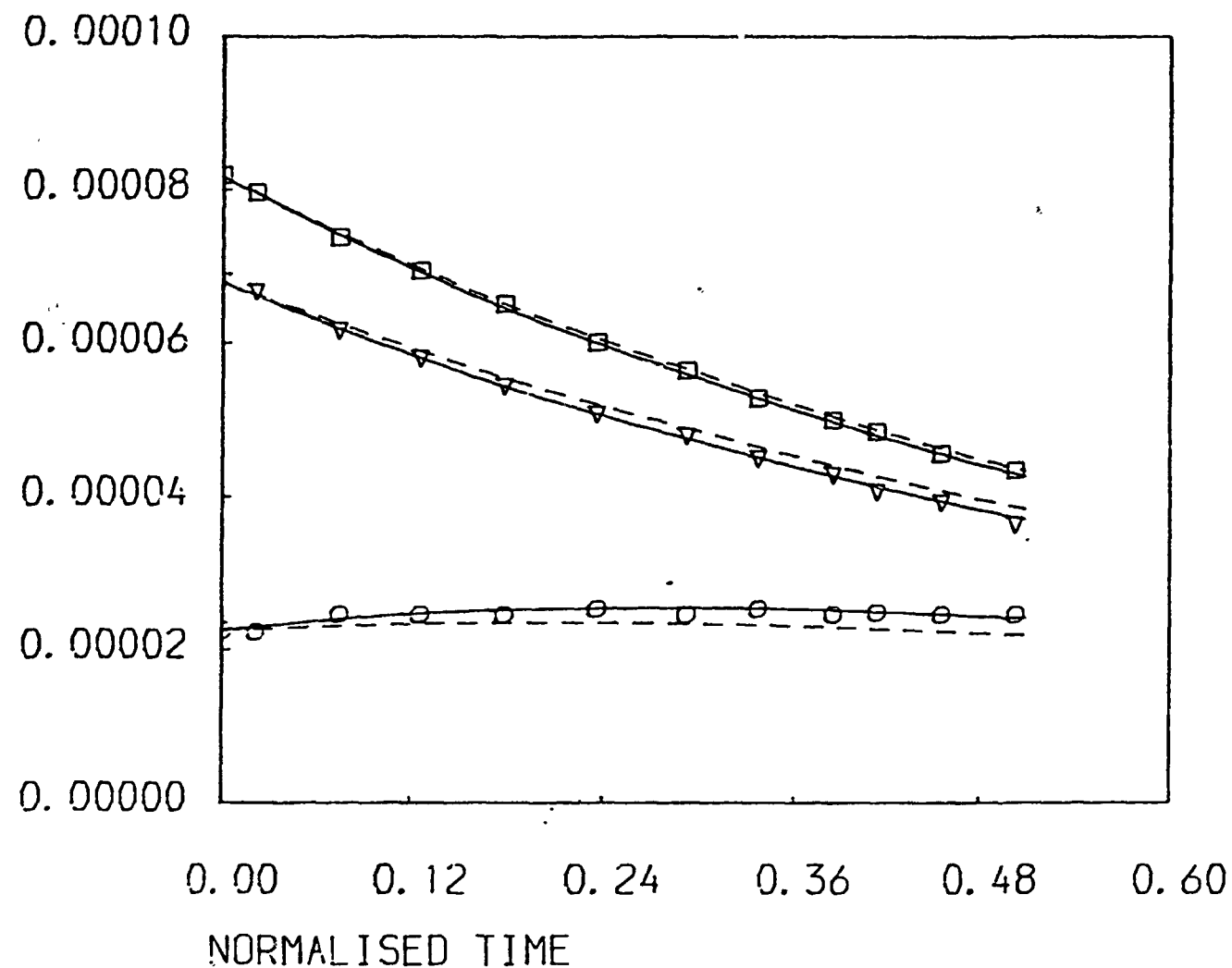


FIGURE 13(b) COMPARISON OF THE EVOLUTION OF THE REYNOLDS STRESS TENSOR AGAINST THE NORMALISED TIME IN THE LE PENVEN ET AL. EXPERIMENT (1984), WITH PREDICTIONS OBTAINED FROM THE LINEAR AND PERTURBATION SOLUTIONS.
($\bar{u}^2 < 0$, LINEAR- - -, NON-LINEAR—) ,

DATA: $\circ \frac{\bar{u}^2}{U^2}$; $\nabla \frac{\bar{v}^2}{U^2}$; $\square \frac{\bar{w}^2}{U^2}$).

CLOSING THE GAP BETWEEN FINITE DIFFERENCE
AND STIRRED REACTOR COMBUSTOR MODELLING PROCEDURES

B.C.R. Ewan, F. Boysan and J. Swithenbank

Department of Chemical Engineering and
Fuel Technology, University of Sheffield.

SUMMARY

The objective of this study is to extend the scope of finite difference modelling of gas turbine combustors so that the maximum air loading (and also the rich and lean limits) can be predicted. Since the finite difference procedure is not suitable for the direct computation of blow off limits, it has been adapted to calculate the residence time distribution from which the equivalent stirred reactor of the primary stabilisation zone can be deduced. Well established stirred reactor modelling can then be used to compute the combustion stability loop and other features such as pollutant production and combustion efficiency. In this paper, a pulsed mercury tracer, which was detected optically, is used to measure the residence time distribution and this result is compared to that computed from our finite difference code. In the computation the turbulent trajectories of a large number of neutrally buoyant particles are used to represent the tracer pulse. Good agreement is found between the measured and the computed response, and the subsequently deduced maximum air loading of the combustor is consistent with the measured value for a variety of fuel nozzles.

INTRODUCTION

Gas turbine combustors involve the highly complex simultaneous processes of three-dimensional flow, droplet evaporation, gas phase mixing, radiation and chemical kinetics. The complexity of these interacting processes is such that most current gas turbine combustor designs depend largely on empirical correlations. In recent years, thanks to the rapid development of computers and concurrent research into the fundamentals of the various aspects of combustion and turbulent flow, mathematical models of a fundamental nature have started to emerge. Although not yet sufficiently reliable design tools, these models have proven to be very effective in analysing existing designs and it is likely that they will progressively replace the cut-and-try approach to combustor design.

This paper addresses the problem of closing the gap between two different approaches to mathematically modelling the behaviour of practical gas turbines and ramjet combustion systems. These approaches are:-

- a) the finite difference method of evaluating the governing differential equations¹, and
- b) the stirred reactor network method which evaluates the simultaneous governing equations for the combustor represented by an interconnected set of individual reactors².

In recent times the finite difference approach has gained rapidly in popularity since it can resolve details of the flow and temperature fields which are important to the turbine designer. Nevertheless there are significant features of combustor operation, such as the prediction of the rich and weak combustion stability limits as a function of pressure, temperature and flow, which are both difficult and expensive to compute via the finite difference procedure. Fortunately, the reactor network approach is well suited to this latter task and the two approaches should be regarded as complementary rather than as competing alternatives.

For any given combustor input pressure and temperature, a maximum combustor throughput is obtained when the rich and lean limits narrow until they close the stability loop. This maximum attainable combustion intensity for the whole chamber is an important design parameter since it determines the maximum operational altitude of the engine. Similarly, since the operation of almost any kind of combustor at mixtures richer than stoichiometric results in severe losses in efficiency, we are particularly interested in the lean limit of combustion since this affects the turn down range of the gas turbine or ramjet engine. The difficulty in using finite difference modelling procedures for calculating the stability limits arises partly from the form of the differential equations. These are stiff non-linear equations and their use in searching for the flame blow-off loop conditions not only involves long computation times but is also complicated by the need to distinguish against numerical instabilities when computing close to a real flame instability. The stirred reactor model is therefore potentially more suitable for the accurate prediction of chemical kinetic effects on combustion efficiency and pollution, maximum throughput and stability limits.

APPROACH

To be able to set up the reactor network, knowledge of the various reactor volumes and their sequence is necessary. It is the object of this study to demonstrate that one can define these volumes by finite difference

modelling which involves the solution of a large set of coupled partial differential equations for the transport of mass, momentum, energy and species, supplemented by appropriate models of turbulence, turbulence-chemistry interactions, droplet combustion and evaporation and radiation.

The field distribution of turbulent dissipation obtained by the solution of a partial differential transport equation can also be utilized to define the stirred and plug flow regions with the degree of stirring or mixing rate being determined from the total dissipation rate within the reactor.

To be able to achieve these ends, experimental information on the residence time distributions (RTD) in actual combustors is extremely helpful in not only determining the reactor volumes directly, but also to validate the more fundamental finite-difference models if these are to be used with confidence in the future. A natural experimental monitor for the predicted residence time distribution is the measured residence time distribution function which is a function of both the input and the output statistics and which for a selected input position of tracer, can be expected to provide the details of the history of fluid parcels.

In general, the RTD consists of a dead time corresponding to the plug flow component and an exponential response corresponding to the stirred component. Unfortunately, if the combustor flow field is modelled by a network of PSR-PFR elements, the overall RTD does not necessarily confirm the uniqueness of the model configuration. However, this problem can be overcome by determining the RTD between various locations within the chamber.

In this study, an effort has been made to measure the RTD functions in a cold flow combustor using mercury vapour as a tracer. Concurrently a predicted three-dimensional velocity field and the associated turbulence quantities have been utilized to simulate the experiments numerically on a digital computer. Detailed description of the experimental method and the theoretical approach is provided in the following sections.

EXPERIMENT

The geometry used for the study was a research Lycoming gas turbine combustion can on which much experience has been gained over a number of years. This is as shown in Fig. 1 and consists of an upstream tangential air entry (7.8%) around the axial fuel inlet and thereafter three groups of six circumferentially distributed holes at positions downstream representing primary (25.5%), secondary (29.9%) and dilution (36.8%) air inlet ports.

In all experiments the total air flow through the can was adjusted to 0.10 Kg/sec.

Most tracer injection methods of the past have employed solenoid operated valves to obtain steps or pulses in the gas or dye concentration³ and suffer the disadvantage of rather long rise times when compared with the residence times typically found in high intensity combustors. The tracer injection employed here however was based on the design by Topps⁴ and consisted of a 70 mm length of 3 mm diameter twin bore refractory tubing into each bore of which was packed conventional dental amalgam. This was caused to spark across the two exposed faces of amalgam using a 0.1 μ f capacitor charged to 500 V from an EHT power supply, and was aided by bridging the gap initially with a smear of graphite from a pencil lead. This could then be sparked 50-70 times before a further graphite replenishment was required and after several such repeats, the diminished performance could be restored by grinding down to a new surface with an abrasive wheel for 1-2 seconds.

When the electrode sparks, a small pulse of mercury vapour is generated and this acts as tracer input localised in space and time. The duration of the vapour pulse in this study was determined optically and was found to be around 1.2 msec. The pulse duration is sufficiently small for the present study where residence times are around 10 times larger, and there is a strong possibility of reducing this further by shaping the sparking pulse, thus making the device suitable for higher throughput gas turbines and ramjet dump combustors.

The arrival of tracer was monitored at the exit plane of the can using a low pressure mercury vapour lamp, transmitting at 253.7 nm, and a photomultiplier whose entrance aperture was 2 mm diameter. A cylinder across the exit face was thus monitored and the presence of mercury vapour was revealed by its strong absorption at 253.7 nm, which in this case gave rise to around 10% absorption. The received photomultiplier signal was analogue/digital converted and stored on a microcomputer.

MODELLING

The main interest in carrying out the experimental work described above was to provide some information to compare with a novel stochastic particle tracking algorithm which has been developed for use in conjunction with our finite difference combustion modelling work to predict droplet trajectories

and fuel evaporation patterns. In this procedure, individual droplets with initial size and velocity are tracked through the combustion chamber as they experience the predicted local flow velocities. At each location a turbulent contribution is also included whose magnitude is based on the random choice of a normally distributed variable simulating Gaussian turbulence, and whose duration is based on an eddy decay model. For a statistically large number of droplets, this has yielded useful information on evaporation, droplet escape and choice of fuel nozzle for particular geometries.

In a similar manner, such a procedure may be used for the converged flowfields with a neutrally buoyant fluid tracer element and if sufficient elements are tracked from the fixed input position to the exit plane, the resulting number versus time is the residence time distribution function, which fully embodies the effects of broadening due to turbulence and recirculation.

SIMULATION

The kinematic relations which describe the motion of a neutrally buoyant particle in a random turbulent flow field can be written in a cylindrical polar system of co-ordinates as

$$\frac{dz}{dt} = \tilde{u}, \frac{dr}{dt} = \tilde{v} \text{ and } r \frac{d\theta}{dt} = \tilde{w} \quad (1)$$

where, t is the time, \tilde{u} , \tilde{v} and \tilde{w} are the instantaneous velocity components in the Z , r and θ directions respectively. The solution of the above stochastic ordinary differential equations requires knowledge of the turbulence field in a Lagrangian frame of reference. Unfortunately, such information is not directly available. However, it is possible to work out the simulation using Eulerian information. The instantaneous velocities in the above equations can be decomposed into a mean and a fluctuating part as

$$\tilde{u}_i = u_i + u_i'$$

where, u_i is the time averaged velocity component and u_i' is the instantaneous fluctuation. The time averaged part of the velocity field can either be measured or obtained from the solution of the governing equations of the conservation of mass and momentum supplemented by a suitable turbulence model. The instantaneous fluctuations, on the other hand, can be related to the local kinetic energy of turbulence K , under the assumption of isotropy and Gaussian probability density, as

$$u_i' = \pm (\frac{2}{3} K)^{\frac{1}{2}} \quad (2)$$

where \pm is a normally distributed random variable. For isotropic homogeneous turbulence the fluctuating velocities persist, on the average, for a time period equal to the Lagrangian integral time scale τ_L , which is related to the kinetic energy of the fluctuating motion K and its dissipation rate ϵ by⁶

$$\tau_L \approx 0.16 \frac{K}{\epsilon} \quad (3)$$

The flow field is obtained in this study from a finite difference solution of the equations of mass and momentum conservation in 3-dimensions. The turbulence is modelled by the widely used $k-\epsilon$ model, which entails the solution of transport equations for the kinetic energy of turbulence and its dissipation rate. Full details of these calculations can be found in Ref. (1).

The random trajectory of each particle is calculated in the following manner.

1. Given the location of the particle at $t=t_0$ the values of the instantaneous velocity fluctuations and the time during which these exist are obtained from eqns (2) and (3). It is assumed that the mean velocity components remain constant within each finite difference cell that the particle is traversing and change abruptly from cell to cell. No effort is made to obtain a local value by interpolation as this would be inconsistent with the approximate nature of the simulation.
2. The kinematic relations (1) are solved for a time step which is the smaller of τ_L and the time required for the particle to cross the current finite difference cell.
3. At each cell crossing the appropriate values of the mean velocities are inserted into eqns (1). New instantaneous fluctuations are obtained from eqn (2) and τ_L from Eq. 3 when the particle has travelled for a time interval equal to τ_L .
4. Steps (1) to (3) are repeated until the particle leaves the combustion chamber.

The simulation technique is equivalent to solving the time dependent transport equation of a passive scalar, which would require considerable computing effort especially in 3-D environments.

RESULTS AND DISCUSSION

Using the experimental technique described above a set of measurements of the RTD were recorded. Individual absorption traces exhibit variation due to background noise and variation of the mixing history for each pulse of tracer. Although these can be very useful for obtaining gross mixing properties or for extracting empirical constants for mixing models³ their average effects have particular significance when comparing with results from fundamental flow and turbulence modelling. Each experiment thus consisted of an average of 50 such individual pulse measurements and as a guard against absolute pulse to pulse variation, each signal was normalised to a predetermined area.

The resulting trace approximated to the smoothed pulse response of the system for the particular input position considered and an example is given in Fig. 3.

Five trace input positions were investigated both experimentally and computationally. All tracer output measurements were made at the exit from the chamber and moving progressively upstream, the input positions were:-

- a) through the secondary port,
- b) on the axis between the primary and secondary ports,
- c) on the axis at the primary port position,
- d) through the primary port,
- e) on the axis at the fuel nozzle position.

For the computation results, about 6000 'particles' were tracked for each inlet location to obtain an adequate statistical sample.

The residence time distribution functions both measured and simulated are shown in Fig.4,5. The agreement between the experimental and simulated residence time distributions are remarkably good for the three shorter distances, however the discrepancy increases for the two longer distances.

Errors are likely to be due to

- i) the use of a computed flow field instead of a measured one,
- ii) to the use of the k- ϵ model results to approximate the Lagrangian information,
- iii) to neglect of the finite duration of the input pulse, and
- iv) the possible existence of some computational dead time on the small axial finite difference cell.

Nevertheless, the agreement is generally satisfactory and confirms the validity of this method of extracting residence time distribution information from the finite difference modelling.

The next step is to convert the tracer information to dead time (plug flow) and stirred reactor time constant components. In particular we wish to characterize the primary zone since this controls the combustion stability. As pointed out above, the stirred reactor regions can be identified readily from the computed regions of recirculating flow and high turbulence intensity or dissipation¹.

In the cases of tracer injection through the secondary port, or on the axis between the primary and secondary ports, inspection of the responses of Figure 4 shows very similar residence time functions. These locations represent the exit from the primary zone, therefore to characterize the primary zone from the overall response function, we must first analyse the response function from either of these locations.

The integrated output signals for tracer injection through the secondary zone and primary zone are plotted on semi-log co-ordinates in Fig. 6. From this figure it is clear that the response for the injection into either zone consists of a dead time followed by an exponential decay. The response of the primary zone alone can be obtained by difference. The values are as follows:-

	Dead time (ms)	Stirred reactor time const.(ms)
Injection into secondary zone	5.1	9.8
Injection into primary zone	9.3	16.8
Primary zone alone	4.2	7.0

The primary zone transfer function is thus:

$$G(s) = \exp(-0.0042s)/(0.007s+1)$$

The effective volume of the primary zone PSR can be deduced directly from this time constant since the volumetric flow rate into the primary zone is known to be $0.03\text{m}^3/\text{s}$. Hence the effective primary zone volume is 0.00021 m^3 . This result is consistent with the value estimated by inspection of the volume of the chamber and the computed size of the recirculation zone. It therefore confirms that the whole of this zone behaves as a single stirred reactor and this supports the use of the PSR model for predicting combustor

behaviour. In order to calculate the lean limit of the combustor at any particular input pressure and temperature, and fuel spray size distribution, we would have to know the local equivalence ratio. Fortunately, this information is available from the finite difference model, and due account can be taken of the important regions where the mixture is locally stoichiometric. Hence the two modelling procedures have complementary utility to the designer.

The maximum air loading ψ of the combustor is attained when the equivalence ratio of the whole primary zone is unity. The actual overall fuel/air ratio at which this is obtained depends on the droplet size distribution and the operating conditions, however, the assumption of a stoichiometric PSR allows the well established relations for stirred reactors to be used. In the case of kerosene fuel, the appropriate relation is^{7,8,9} :-

$$\psi = \frac{\dot{m}}{VP^{1.75}} = \frac{K \exp(-E/RT_R) (1-\eta_c)^{0.75} (1-\phi\eta_c)}{T_R^{1.25} \phi^{0.25} \eta_c}$$

where the equivalence ratio ϕ should be taken equal to unity, and in SI units, $E/R = 21,000$ and $K \approx 8400$. V = volume, P = pressure, T_R = reactor temperature, η_c = combustion efficiency and \dot{m} = air mass flow. Thus for the case in question, at 10^5 N/m^2 , $\phi = 1$, and $T_o = 350 \text{ K}$, Ref. 7 Fig 5.7 shows that $\eta_c \approx 0.78$ at the point of maximum reaction rate in a stirred reactor. Ref. 7 Fig. 2.20 gives an adiabatic temperature rise of 1850 K at these conditions, hence the primary reactor temperature is $350 + 0.78 \times 1850 \approx 1800$. The maximum air loading is therefore predicted to be:

$$\begin{aligned} \psi_{\max} &= \frac{\dot{m}}{VP^{1.75}} = \frac{8400 \exp(-21,000/1800) 0.78^{1.75}}{1800^{1.25} 0.78} \\ &= 5.6 \times 10^{-7} \\ \therefore \dot{m}_{\max} &= 5.6 \times 10^{-7} \times 0.00021 \times (10^5)^{1.75} \\ &= 0.066 \text{ kg/s.} \end{aligned}$$

Thus the total chamber flow at blow off 0.2 kg/s . The validity of this result is illustrated in Figs 7a) and b) in which measured stability loops for this combustor are plotted for a variety of fuel nozzles (Details of the experiment are given in Ref.10). It is clear that the maximum air loading for all the fueling systems tested occur close to the expected value.

It is also apparent that the technique presented here can be readily extended to the prediction of rich and lean combustion limits, however this analysis is beyond the scope of the present study.

REFERENCES

1. F. Boysan, W.H. Ayers, J. Swithenbank and Z. Pan, "Three-Dimensional Model of Spray Combustion in Gas Turbine Combustors", Journal of Energy, Vol. 6, No. 6, Nov.Dec.1982, p.368-375.
2. D.S. Prior, J. Swithenbank and P.G. Felton, "Stirred Reactor Modelling of a Low Pollution Liquid Fuelled Combustor", Ed. L.A. Kennedy, Progress in Astronautics and Aeronautics, Vol. 58, Turbulent Combustion, 1978, pp. 351-372.
3. J. Swithenbank, A. Turan, P.G. Felton and D.B. Spalding, "Fundamental Modelling of Mixing, Evaporation and Kinetics in Gas Turbine Combustors", NATO/AGARD Conference Preprint No. 275, Combustor Modelling, 1979.
4. J.E.C. Topps, "An Optical Technique for the Investigation of flow in Gas Turbine Combustors", 17th. Symposium (International) on Combustion, The Combustion Institute, 1978.
5. J. Swithenbank, F. Boysan and W.H. Ayers, "Fundamentals of Fuel/Air Mixing in Combustion Reactor Systems", Interflow Conference Proceedings, I.Chem.E., Harrogate, 1981.
6. J.O. Hinze, "Turbulence", McGraw Hill, 1975.
7. A.H. Lefebvre, "Gas Turbine Combustion", McGraw Hill, 1983.
8. E.T. Curran, "An Investigation of Flame Stability in a Co-axial Dump Combustor", Dissertation AFIT/AE/DS79-1, Air Force Institute of Technology, Dayton, Ohio.
9. V.W. Greenhough and A.H. Lefebvre, "Some applications of Combustion Theory to Gas Turbine Development", Sixth Symposium (International) on Combustion, The Combustion Institute, 1956, pp. 858-869.
10. P.G. Felton and J. Swithenbank, "The effect of fuel preparation on Gas Turbine combustor performance", Proceedings of the 2nd. European Symposium on Combustion, France, 1975.

Captions to Figures

- Figure 1. Gas turbine can geometry and dimensions.
- Figure 2. Example of individual tracer pulse response.
- Figure 3. Tracer response signal obtained by averaging 50 individual single shot responses.
- Figure 4. Comparison of observed tracer response signal and calculated residence time functions for tracer input to the primary zone of gas turbine can. — = observed response, ● = calculated values.
- Figure 5. Comparison of observed tracer response signal and calculated residence time functions for tracer input to the secondary zone of gas turbine can. — = observed response, ● = calculated values.
- Figure 6. Log of integrated pulse response (step response) vs time for combined primary zone responses and combined secondary zone responses. ○ = secondary zone response, △ = primary zone response.
- Figure 7. a) Stability loop for pressure jet atomisers - kerosene fuelled.
b) Stability loop for air blast atomisers - kerosene fuelled.

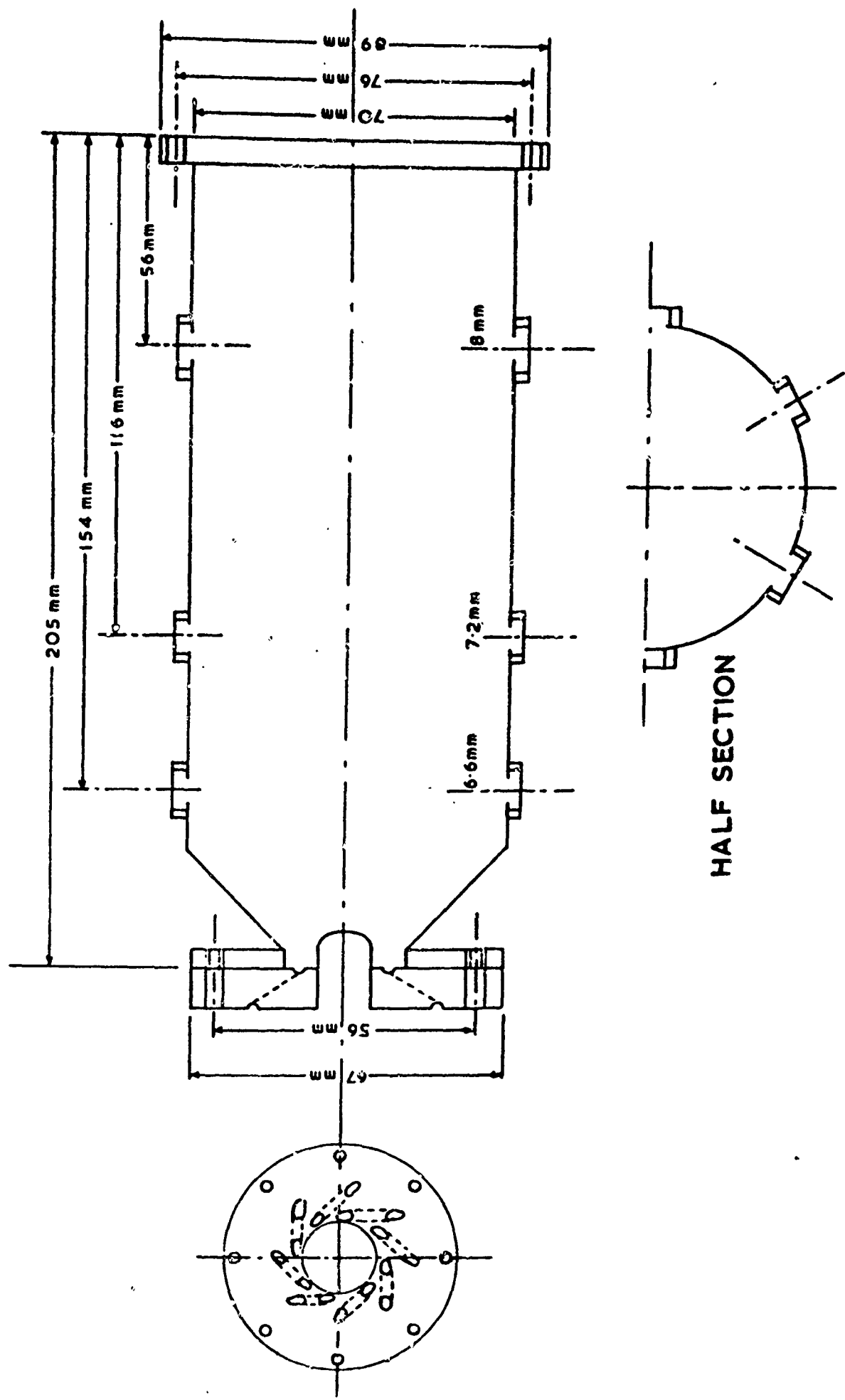
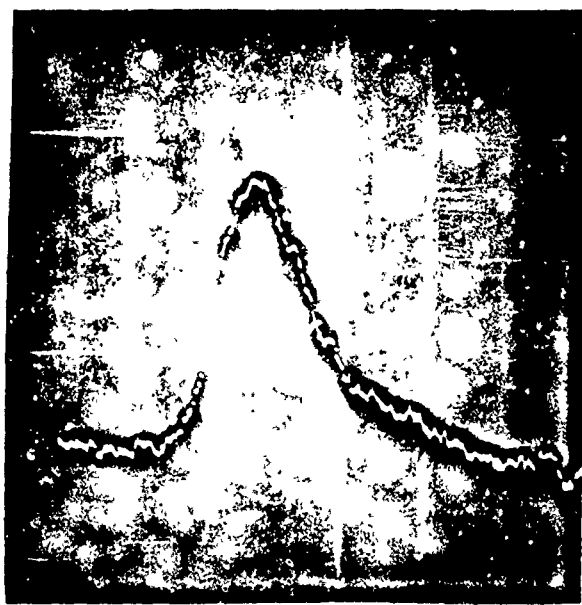


FIGURE 1



—

5 msec

FIGURE 2.

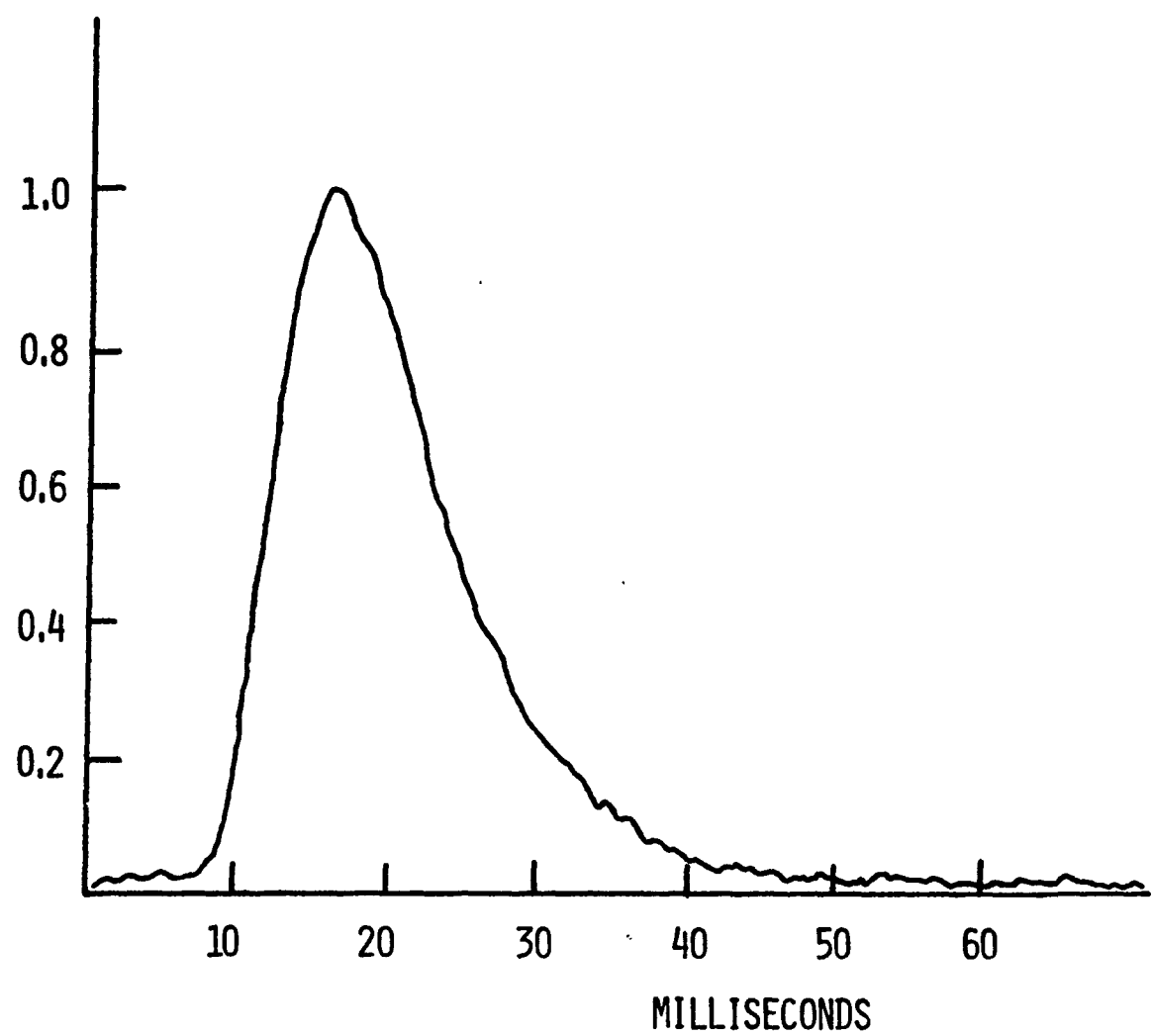
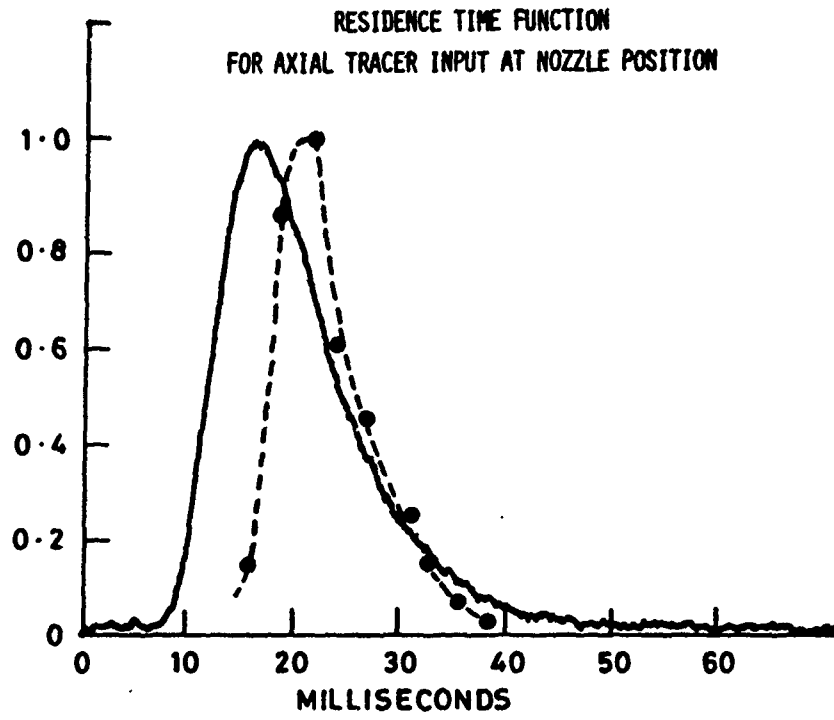
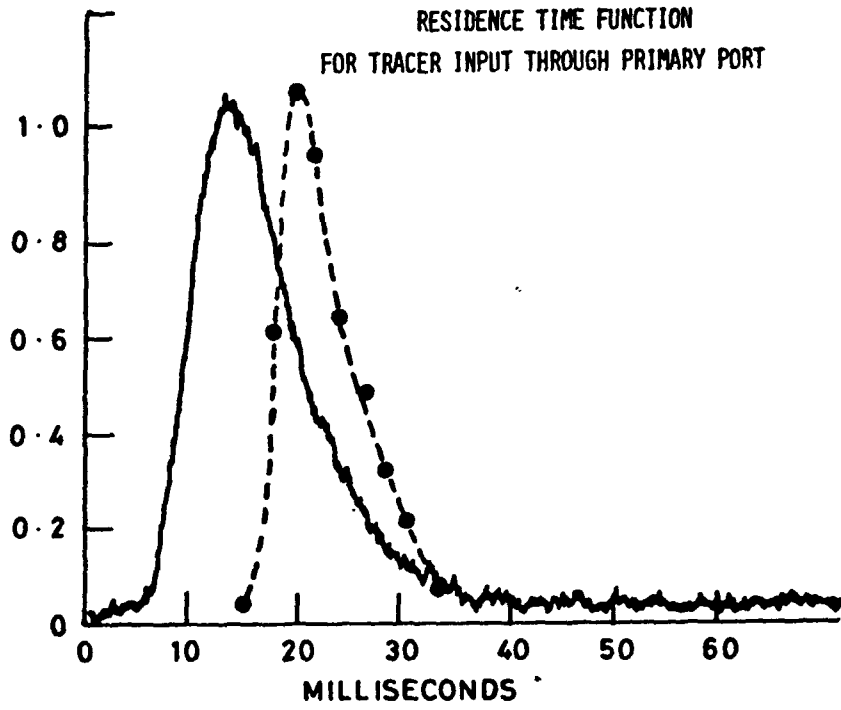


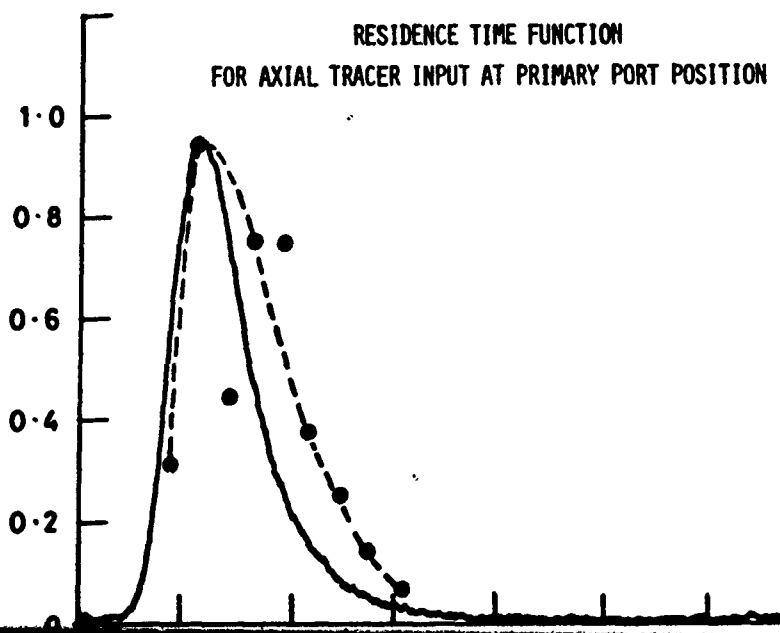
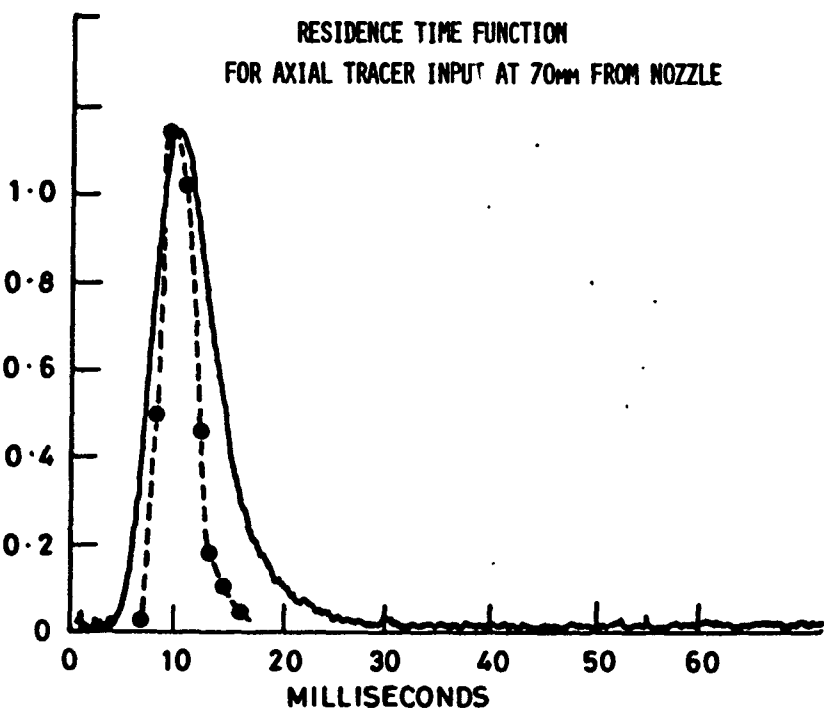
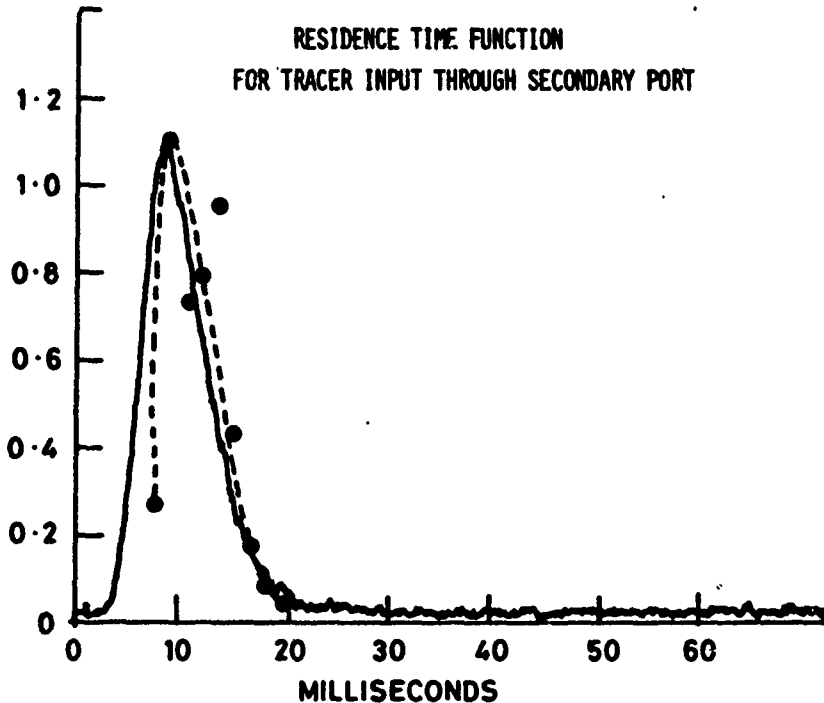
FIGURE 3.

RESIDENCE TIME FUNCTION
FOR AXIAL TRACER INPUT AT NOZZLE POSITION



RESIDENCE TIME FUNCTION
FOR TRACER INPUT THROUGH PRIMARY PORT





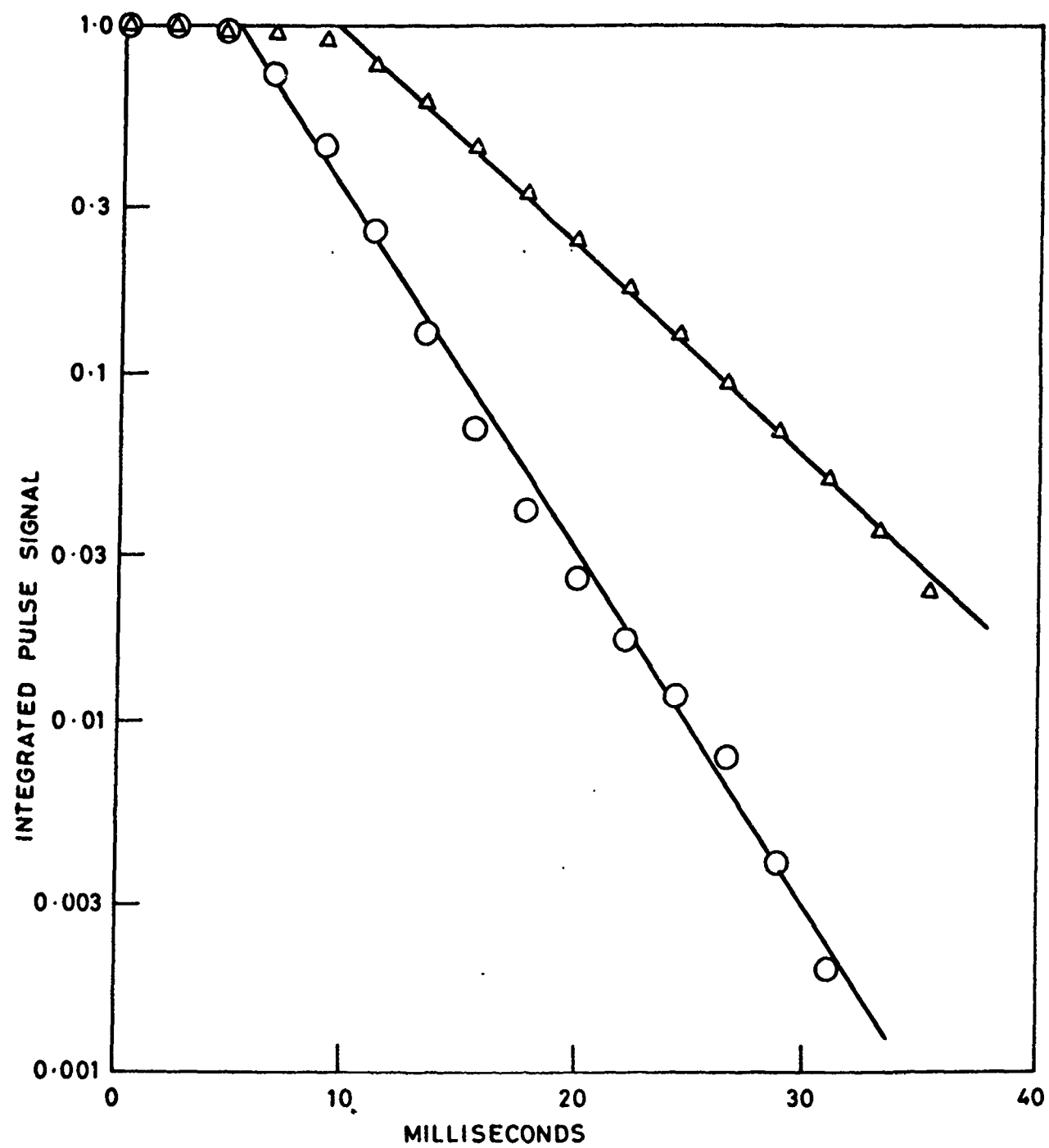
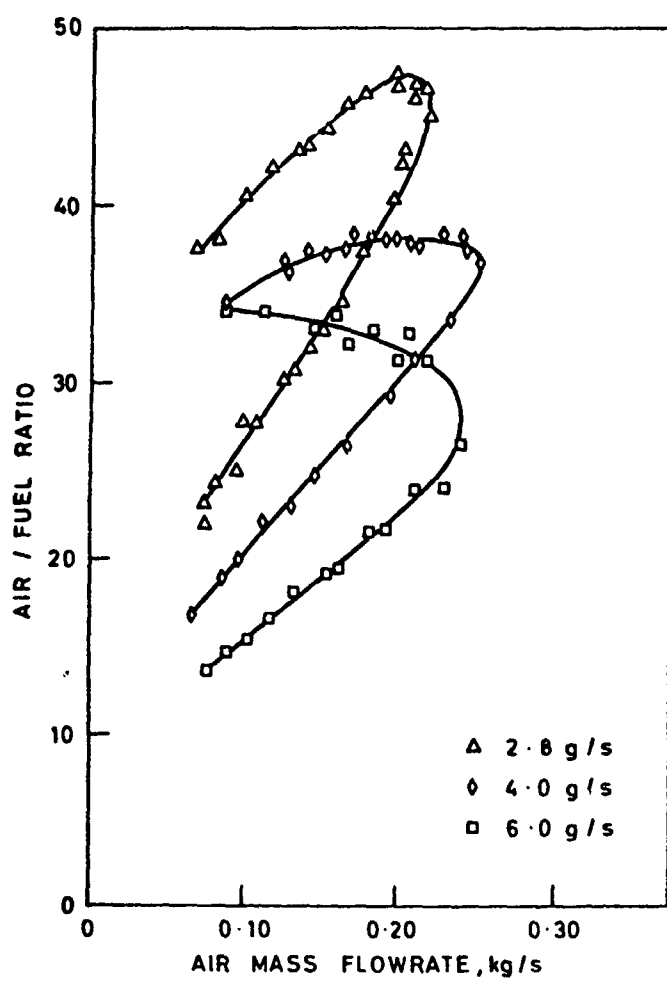
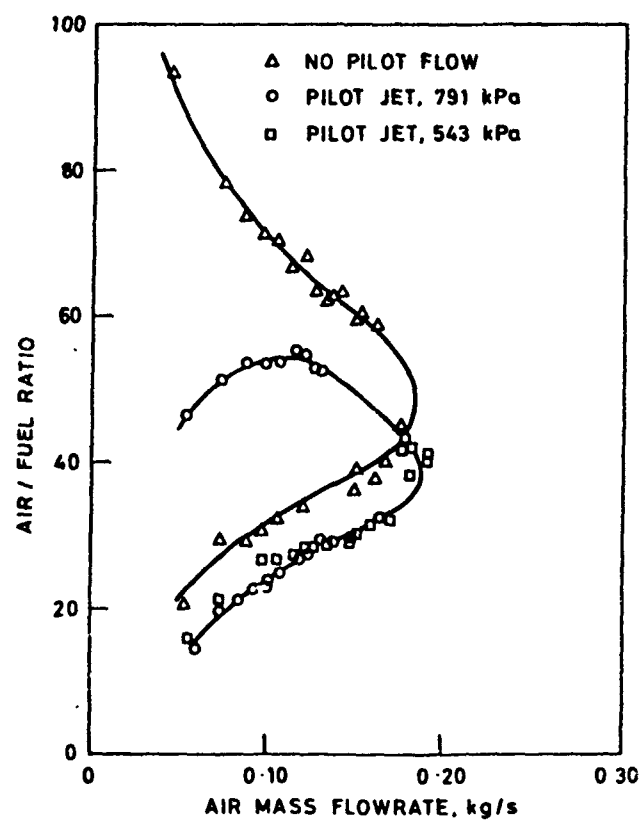


FIGURE 6.



[a]



[b]

FIGURE 7.

Multiple scattering effects on particle sizing by

Laser diffraction

P.G. Felton, A.A. Hamidi and A.K. Aigal

August 1984

431 HIC

CONTENTS

	<u>Page No.</u>
Introduction	1
Theory	2
Results	12
Conclusions	18

Introduction

The measurement of the size distribution of droplets and particles is a common problem in the current technology. In many processes measurement and control of particle size is of great importance. An optical technique initially developed in this department and later in conjunction with Malvern Instruments Ltd, makes on-line particle sizing possible. The technique uses the diffraction pattern formed when particles are illuminated by a parallel beam of monochromatic, coherent light to determine the particle size distribution.

One of the major limitations of this method is that for reliable results not more than fifty percent of the incident light should be scattered by the particle field. It has been speculated that above this limit the effect of multiple scattering of light by the particles will have a great influence on the results.

However in many problems such as those encountered in particle sizing in diesel injectors and heavy fuel oil atomizers this limit is usually exceeded. A technique has been developed which predicts the effect of multiple scattering on the diffraction pattern. For distributions which can be described by simple functions such as Rosin-Rammler and Log-Normal a set of correction equations have been derived to compensate for the effects of multiple scattering. As an illustration of this approach results are presented for a commercial diesel injector which gives up to 90% obscuration.

Theory:

When a spherical particle is illuminated by a parallel beam of monochromatic, coherent light a Fraunhofer diffraction pattern is formed, superimposed on the geometrical image, this pattern is large compared with the image. If the particle field is placed within the focal length of a suitable Fourier transform lens then the undiffracted light is focussed to a point on the axis of the lens and the diffracted light forms a far field Fraunhofer pattern of rings around the central spot(Fig.1). Movement of the particles does not cause movement of the diffraction pattern since light diffracted at an angle, δ , will give the same radial displacement in the focal plane irrespective of the particle position in the illuminating beam.

The theory and analysis of light scattering by single spherical particle can be found in standard texts on optics¹ and has been briefly discussed in a paper by Swithenbank et al².

The diffraction pattern for a single sphere (or a field of monosize spherical particles) is shown in figure(2). The light intensity is maximum at the centre of the diffraction pattern and oscillates with strongly decreasing amplitude as the radius increases.

The diameter of the diffraction pattern is inversely proportional to the particle diameter and the smallest

particle that can be measured is of the order of one micron since the particle size must be greater than the wavelength of the illuminating laser light (wavelength = 0.6328 μm).

As the diffraction pattern is unique for a given particle size or a given mixture of particles then the light energy pattern can be used to deduce the size (or size distribution) of the particle(s).

For a monosize distribution of particles of size a , the light energy contained within a circle of radius s in the focal plane of a lens is given by:-

$$L = 1 - J_0^2 \left[\frac{2\pi a s}{\lambda f} \right] - J_1^2 \left[\frac{2\pi a s}{\lambda f} \right] \quad \dots \dots (1)$$

Thus the light energy within any ring in the focal plane, bounded by radii s_1 and s_2 , is given by:-

$$L_{s_1, s_2} = E \left\{ J_0^2 (Kas_2/f) + J_1^2 (Kas_2/f) - J_0^2 (Kas_1/f) - J_1^2 (Kas_1/f) \right\} \quad \dots \dots (2)$$

Where E is the energy falling on the particle which is proportional to the cross-sectional area of the particle, therefore:-

$$E = C' \pi a^2 \cdot N \quad \dots \dots (3)$$

And N is given:-

$$N = 3w / 4\pi a_p^3 \quad \dots \dots (4)$$

Thus:-

$$E = C'' \frac{w}{a} \quad \dots \dots (5)$$

Where w is the weight fraction of particles of radius a . C'

and C'' are constants which depend on the power of the laser used, ρ is the density of the particle. Figures (3) and (4) are plots of equations (1) and (2). If instead of a single particle a collection of particles of different size is considered then the light energy falling on any ring in the focal plane is the sum of the contribution from individual particles:-

$$L_{s_1, s_2} = C_2 \sum_{i=1}^m \frac{w_i}{a_i} \left[J_0^2 \left(\frac{Ka_i}{f} s_1 \right) + J_1^2 \left(\frac{Ka_i}{f} s_1 \right) - J_0^2 \left(\frac{Ka_i}{f} s_2 \right) - J_1^2 \left(\frac{Ka_i}{f} s_2 \right) \right] \dots \dots (6)$$

Where:

$$K = 2\pi/\lambda \dots \dots (7)$$

If a particle size distribution is classified into a number of size ranges then it is preferable to make measurements at radii where the first maximum of the diffracted energy distribution occurs. This location is given by:-

$$2\pi a_s / \lambda_f = 1.375 \dots \dots (8)$$

If a detector is used which is divided into a set of circular rings then each of these rings will define a characteristic particle size range. The total light energy distribution is the sum of the product of the energy distribution for each size range and the weight fraction in that range. This can be expressed in the form of a matrix equation:-

$$L(I) = W(J) T(I, J) \dots \dots (9)$$

Where $L(I)$ and $W(J)$ are the light energy and weight

distribution respectively and $T(I,J)$ contains the coefficients which define the light energy distribution for each particle size range. The weight distribution is deduced in such a way that:-

$$\sum (L(J) - W(J) T(I,J))^2 \text{ is a minimum}$$

The ratio of the light intensity measured at the centre diode, before and after the particle field is placed in the laser beam, gives the fraction of the light transmitted by the particles. The transmission is related to the total projected area of the particles by the Beer-Lambert law:-

$$\ln \left(\frac{I}{I_0} \right) = - \tau l \quad \dots \dots (10)$$

Where I and I_0 are the light intensities with and without the sample respectively, l is the optical path length and τ is given by:-

$$\tau = 2 \sum_{i=1}^m N_i A_i \quad \dots \dots (11)$$

In deducing the size distribution from the light energy distribution several distribution functions have been used. Normal, Log-Normal, Rosin-Rammller and Model Independent are some examples. The distributions employed in this study are mainly Rosin-Rammller and Log-normal which are both two parameter forms.

The Rosin-Rammller distribution which is of particular interest in spray studies is defined by³:-

$$Y = 100(1 - \text{Exp}(-x/\bar{x}))^N \quad \dots \dots (12)$$

Where Y is the percentage of particles with diameter less than X, \bar{X} is the Rosin-Rammller mean diameter and N is the Rosin-Rammller exponent, which is a measure of the spread of the particles about the mean size \bar{X} .

The log-Normal distribution is defined by:-

$$L_d = \frac{1}{\sqrt{2 \ln(N)}} \exp\left[\frac{(\ln(d) - \ln(\bar{X}))^2}{2 \ln(N)}\right] \quad \dots\dots (13)$$

Where L_d is the weight frequency at size d, \bar{X} is the geometric mean of the distribution and N the geometric standard deviation.

The calculated size distribution, whichever model is used, is reliable only if the light obscuration is in the range 5-50%. The lower limit is the limit of measuring a representative sample of particles and the upper limit is the onset of significant of multiple scattering. Within this range the sample measured is taken to be representative of the particle field and the light scattered by particles is not further scattered by others.

Since the angle of the scattered light varies proportionally with the inverse of the particle diameter, the effect of multiple scattering is to represent a bigger proportion of smaller particles than the particle field actually contains.

The model developed in this study predicts the effect of multiple scattering on the parameters of the distributions defined by equations (13) and (14).

In the development of the model the particle field is

divided into slices. The following assumptions were made:

- A) The light path is divided into a series of slices of equal obscuration each slice scatters 10% of the incident light.
- B) Only half of this scattered light is forward scattered light (the scattered light as seen by the detector plane-Babinet's principle).
- C) There is no multiple scattering within a slice.
- D) The scattered light pattern leaving one slice is the incident light for the next.

The model enables the determination of the overall scattered light energy distribution for each slice. As the number of slices is increased the fraction of the primary laser beam that has been scattered increases and hence higher obscurations can be simulated.

Determination of the light energy distribution for the first slice is straight forward since the only illuminating light is the primary undiffracted beam. Equation(6) is used directly to calculate this data. For the second and all other slices there is the full spectrum of the scattered light at all angles as well as the undiffracted light to be considered.

A numerical integration method is needed to calculate these data. The integration procedure requires the division of the rings into segments. By considering each segment as a 'point scatterer' which scatters the light that would have been incident on this segment according to equation(6) and assumptions (A) and (B), thus determining the light scattered

to all other segments. Figure(5) shows a typical integration step. Ring I is the 'scattering ring' and ring J is the 'receiving ring'. The segment on ring I is the point scatterer, all the light within this segment is represented by point S. The receiving segment R is treated as an area.

Distances OS, OA and OB are known. the angle α is incremented from 0 to π depending on how the rings are divided into segments. Distances SB and SA can be calculated using the Cosine equation:-

$$(SA)^2 = (OA)^2 + (OS)^2 - 2(OA)(OS)\cos\alpha \quad \dots \dots (14a)$$

$$(SB)^2 = (OB)^2 + (OS)^2 - 2(OB)(OS)\cos\alpha \quad \dots \dots (14b)$$

In order to simplify the geometry the point S is transferred to S' a point along the axis OAB so that:-

$$SR=S'R=(SA+SB)/2 \quad \dots \dots (15)$$

Now using S'A and S'B in equation(6) the scattered light energy due to S within these radii can be calculated. Knowing the area of the receiving segment and area of the ring bounded by S'A and S'B the fraction of the scattered light from S to R is determined. This procedure is carried out taking two segments at a time until the detector is fully covered.

The total light energy on any ring after each slice is the sum of all the contributions made from other rings (secondary scattered components) plus the scattered light from the primary beam (primary scattered component) that falls on that ring.

There are a number of points that need to be mentioned at this stage.

1) The rings on the detector are not of equal width. The width of the 31 rings increases from 0.094mm to 1.565mm. This led to problems with the integration as will be shown later.

2) As a first attempt the rings were divided into equal area segments so that the first ring and the last ring had 4 and 6972 segments respectively. At this stage the detector was assumed continuous and the gaps between the rings were not considered. This arrangement was found to be totally impractical due to the very long computer time needed and was abandoned in favour of dividing the rings into equal angles (fig.5). This led to a vast improvement in computer time.

At this stage a new method for determining the amount of scattered light within a ring was developed which made the use of equation(6) and hence Bessel functions redundant and this also greatly reduced computer time. The method required the primary scattered light energy distribution for a given sample of particles for twice the diode dimension. This was found either using equation(6) or by using Malvern software,

the latter option being preferred. A cubic spline fit was made to this data and interpolation was used to find the energy between any two radii S'A and S'B. All the rest of the calculation procedure remained the same.

The reason that this technique saves computer time is due to the large number of times which the Bessel function is called and that this function is calculated via a ten term polynomial* as opposed to the four terms of the cubic spline. In addition the Bessel function is called four times per diode ring and fifteen times per size class whereas the cubic spline is only called twice per diode ring.

As mentioned earlier the rings on the detector are not of equal width, Figure(6) shows the detector. It was found that due to the comparatively 'big' and 'long' segments in the outer rings the energy on the inner ring was grossly overestimated resulting in unrealistic energy distribution curves(fig.7).

Realising the cause of the problem it was found that it was drastically reduced by dividing the bigger rings into smaller sub-rings. This procedure was followed for increasing numbers of subrings until no further appreciable change in the energy distribution curve was observed. The final arrangement consisted of having 109 sub-rings of comparable width so that the innermost ring had one ring(sub-ring) and the outer ring was divided into ten sub-rings. Table(1) gives the dimensions of the detector. This arrangement of equal angle segments and 109 sub-rings is the one used to derive all the results

mentioned in the next section.

The energies calculated for all 109 sub-rings at the end of each slice were reduced to 31 according as how each ring had been divided into sub-rings. The gaps between the detector rings are all of width 0.036mm which is comparable with the inner ring widths but negligible compared with the outer ring widths. Hence the effect of the gaps was taken into consideration which further reduced the energy on the inner rings in comparison to the outer ones.

Figure(8) shows the final theoretical light distribution for a given size distribution at several obscurations. The peak of the curve moves to the right ie the outer rings which represent smaller size classes. These curves clearly indicate the effect of multiple scattering.

Results:

Theoretical and experimental results for a number of different fine particulate samples are explained and shown in the first part of this section. Having justified the accuracy and applicability of the model a number of different distributions are treated theoretically and correlation equations are derived.

A) four reference samples were available for experiments:

DVN latex-E19	monosize 13.8 μ
DVs latex-G7	monosize 40.8 μ
NBS SRM 1003	range 5.0-30.0 μ
NBS SRM 1004	range 37.-105. μ

The apparatus is shown schematically in figure (9) and the cell used for suspension of the samples is shown in figure (10). A very dense suspension of the sample was made and the stirrer speed was controlled and adjusted so that all the particles were in suspension, while not so fast as to cause cavitation and hence formation of bubbles. A reading was taken and by removing one ml of the suspension and replacing it by one ml of fresh water the concentration was reduced, another reading taken and this procedure repeated until the

obscuration reading was less than 40%. The water used to make up the suspension had been previously filtered to remove particles greater than approximately one micron. A drop of Nonidet-P42 was added as a dispersant. Several runs for each of the four samples were carried out to ensure that representative sample had been considered.

The model independent option was used to process the data acquired for the monosize samples. The theoretical model was used to generate the light energy distribution for one of the monosize samples(latex-E19). The theoretical and experimental results are plotted in figures (11) and (12). The two plots show the same trend as the obscuration is increased. This clearly shows the applicability of the model to monosize as well as polysize particle fields.

The Rosin-Rammler distribution was used to process the light energy data and deduce \bar{X} and N for the two SRM samples. Two correction parameters are defined as follows:

$$C_x = (\text{Actual } \bar{X}) / (\text{Apparent } \bar{X}) \quad \dots \dots \quad (16a)$$

$$C_n = (\text{Actual } N) / (\text{Apparent } N) \quad \dots \dots \quad (16b)$$

As the obscuration is decreased \bar{X} and N increase until, at about 60% obscuration, these values remain unchanged for any further reduction in obscuration.

Figures (13) and (14) show plots of C_x and C_n .vs.

obscuration for one of the samples used(SRM 1003). The values of \bar{X} and N at 50% obscuration were taken to be the true representation of the sample used. The model was used to generate the light energy distribution for fifty slices which corresponds to approximately 99.5% obscuration. These theoretical values are also plotted in figures (13) and (14). As it can be seen there is very good agreement between the two results.

Similar results were obtained for the other sample (SRM-1004) but for a given obscuration the correction factors C_x and C_n are different from the results for the first sample (SRM-1003). This indicated that the correction factors are not only a function of obscuration but also a function of \bar{X} and/or N for the sample considered. This point was further investigated and is discussed in the second part of this section.

B) As mentioned, the results indicate that the correction factors for \bar{X} and N are functions of actual \bar{X} and N as well as the obscuration. Five size distributions of approximately equal N(2.3) and different \bar{X} (27.-85. micron) were considered. For each of these the light energy distributions for up to fifty slices(99.5% obscuration) were generated and using the Malvern software these energy distributions were used to generate apparent size distributions. For each size distribution the factors C_x and C_n were calculated and plotted in figures (15) and (16). Since the variation of C_x and C_n for

a given obscuration show no consistant trend for different samples and that all the correction factors for a given obscuration are very close to each other, it was concluded that C_x and C_n are independent of the actual, and hence apparent, \bar{X} . The slight variation is within the range of convergence errors when calculating the size distribution from light energy distribution.

Six size distributions of approximately equal \bar{X} (35. micron) and different N (1.4-3.8), the range of interest for sprays, were considered in the same way as the previous investigation. the results are plotted in figures (17) and (18). In this case a clear and consistant dependence of C_x and C_n for a given obscuration on actual or apparent N is illustrated.

It was decided to deduce the correction equations in terms of obscuration and the apparent N , since this is the information that is known when a sample is measured and the resulting light energy distribution processed. Figures (19) and (20) show these results plotted as C_x or C_n against the apparent N for four different obscurations. Using multiple linear regression the following correction equations were found to fit the theoretical data well. These equations apply to Rosin-Rammller distribution only:-

$$C_x = 1.0 + (0.036 + .4947(\text{OB}))^{8.997} N_{\text{app}}^{(1.9 - 3.437(\text{OB}))} \pm 2.2\% \quad \dots \dots (17)$$

$$C_n = 1.0 + (0.035 + .1099(\text{OB}))^{8.6501} N_{\text{app}}^{(0.35 + 1.45(\text{OB}))} \pm 1.8\% \quad \dots \dots (18)$$

These equations apply for obscurations in the range 65-98% and

for apparent N in the range 1.2-3.8 with the given uncertainty limits. For obscurations less than 65% the correction factor is comparable with experimental and convergence uncertainty.

The same analysis was carried out for the Log-Normal distribution. The results are shown in figures (21) and (22), again the representative size \bar{X} decrease with increasing obscuration (C_x increasing). On the other hand the correction factor for N decreases, since as the obscuration increases the distribution becomes broader and the geometrical standard deviation increases.

Figures (23) and (24) are plots of C_x and C_n against the apparent N for different obscuration. The Log-Normal results were not as consistent and smooth as those for Rosin-Rammler, this is possibly due to the definition of the distribution and its applicability to the problem since the Log-Normal distribution shows a long tail at large sizes.

Again multiple linear regression was used to generate equations for C_x and C_n in terms of apparent N and obscuration.

$$C_x = (1.0 + 6.87 \times 10^{-4} e^{7.6371(OB)}) e^{-\frac{0.1395 + 1.7843(OB)}{N_{app}}^{11.3131}} \dots\dots (19)$$

$$C_n = (0.96 + 7.3965 \times 10^{-4} e^{5.6798(OB)}) - (0.0129 + 0.1415(OB))^{7.1516} N_{app} \dots\dots (20)$$

These equations have uncertainty limits of $\pm 15\%$, for better results the following five equations for C_x and C_n can be used. These equations apply to obscuration in the range 65-98% and apparent N values of 1.6-3.0. The general form of the

equations are given below and the particular coefficients are listed in Table(2).

$$C_x = A \left(\text{Exp}(-B/N_{app}) \right) \dots\dots (21)$$

$$C_n = C - D(N_{app}) \dots\dots (22)$$

For intermediate obscurations, linear interpolation should be used.

As this work was carried out with reference to diesel sprays an example for illustration purposes is given here. Figures (25) and (26) show the actual and apparent results for a diesel injector. The operating and experimental conditions are listed in Table(3). Figure(27) is the time-obscuraction plot indicating the duration of the spray.

Conclusion:

A mathematical model has been developed to predict the effect of multiple forward scattering in a dense particle field on the measured Rosin-Rammller and Log-Normal distribution parameters.

The theoretical results from the model were tested against experimental results for equivalent size distributions. Good agreement was observed as a justification of the accuracy of the model. Two correction factors have been defined and the dependency of these factors on obscuration and distribution parameters (\bar{X} and N) have been examined. Consequently a number of correction equations have been derived which allow the applicability of this method of particle sizing be extended twenty five fold from an obscuration of 50% to that of 98%. The uncertainty limits of using these correction factors, especially for the Rosin-Rammller distribution, is comparable with experimental and solution convergence uncertainties.

References:

- 1a. M.V.Kelvin, 'Optics', Wiley, New York, 1970.
- 1b. H.C.Van De Hulst, 'Light Scattering By Small Particles', Wiley, New York, 1957.
2. J.Swithenbank, J.M.Beer, D.S.Taylor, D.Abbot and C.G.McCreadh, 'A Laser Diagnostic Technique for the Measurment of Droplet and Particle Size Distribution'. Presented as paper 76-69 at the AIAA Aerospace Science meeting, Jan.1976, Published in 'Experimental Diagnostics In Gas Phase Combustion Systems', Progress in Astronautics and Aeronautics, vol 53, ed. B.T.Zinn 1977.
3. R.A.Mugele and H.D.Evans 'Droplet Size Distribution in Sprays'. Indust. and Engng Chem., vol.43, Pl317.
4. Handbook of Mathematical Functions, edited by M.Abramowitz and I.A.Stegun. National Bureau of Standards 1964.

Acknowledgments:

Financial support towards this work by the Science and Engineering Research Council, and the Ministry of Defence is gratefully acknowledged. One of us(A.K.A) would like to thank the British Council for the opportunity to work on this project.

Ring No.	Inner Radius mm	Outer Radius mm	Width mm	No. of Subrings
1	.124	.218	.094	1
2	.254	.318	.064	1
3	.353	.417	.064	1
4	.452	.518	.066	1
5	.554	.625	.071	1
6	.660	.737	.076	1
7	.772	.856	.084	1
8	.892	.986	.094	1
9	1.021	1.128	.107	1
10	1.163	1.285	.122	1
11	1.321	1.461	.140	2
12	1.496	1.656	.160	2
13	1.692	1.880	.188	2
14	1.915	2.131	.216	2
15	2.167	2.416	.249	2
16	2.451	2.738	.287	2
17	2.774	3.101	.328	3
18	3.137	3.513	.376	3
19	3.549	3.978	.429	3
20	4.013	4.501	.488	4
21	4.536	5.085	.549	4
22	5.121	5.738	.617	4
23	5.773	6.469	.696	5
24	6.505	7.282	.777	5
25	7.318	8.184	.866	6
26	8.219	9.185	.965	6
27	9.220	10.287	1.067	7
28	10.323	11.501	1.179	8
29	11.537	12.837	1.300	9
30	12.873	14.300	1.427	10
31	14.336	15.900	1.565	10

Table 1 - Photodetector diode dimensions

% obscuration	A	B	C	D
65.0	1.1370	0.1479	0.9925	0.0188
79.4	1.2597	0.3005	1.0250	0.0425
87.8	1.4425	0.4855	1.0575	0.0640
92.5	1.7094	0.7433	1.1010	0.0833
97.5	2.7160	1.5244	1.1850	0.1330

Table 2 Correction equation coefficients for the Log-Normal model.

Liquid volume per injection	594.6 mm ³
Injection pump speed	170 R.P.M.
Peak injection pressure	312 bars
Nozzle orifice diameter	0.38 mm
Distance downstream of the Nozzle	6.0 cm
Horizontal distance from spray axis	0.8 cm

Table 3 Operating and experimental conditions for the diesel injector.

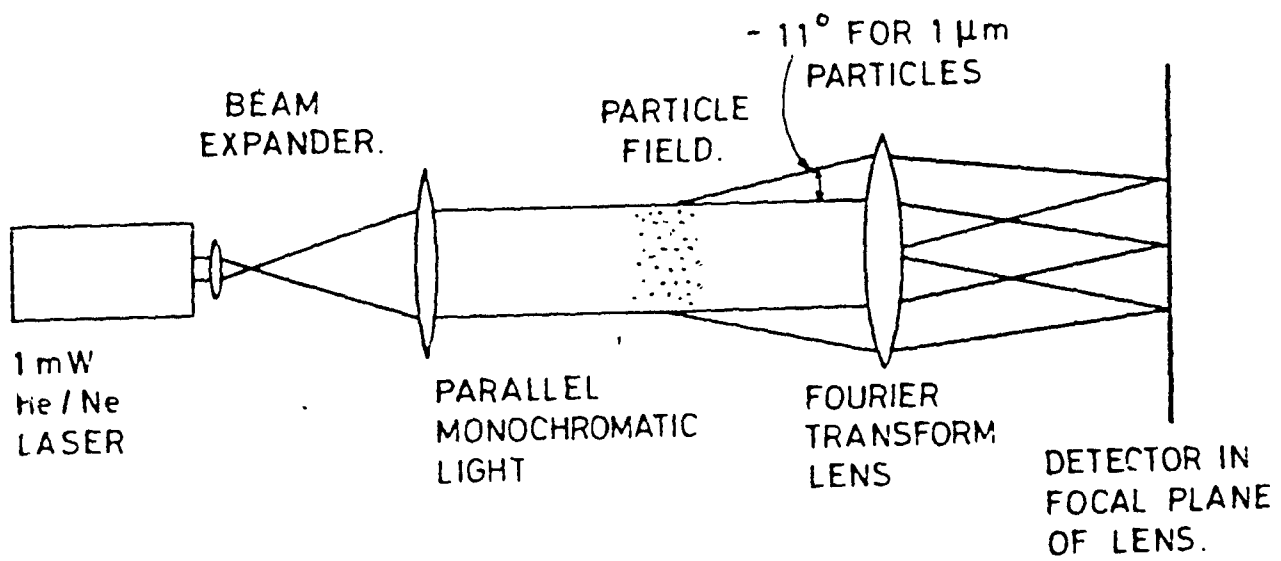


FIGURE 1. OPTICAL ARRANGEMENT OF FOURIER TRANSFORM LENS TO OBTAIN THE SIZE DISTRIBUTION OF SOLID OR LIQUID PARTICLES.

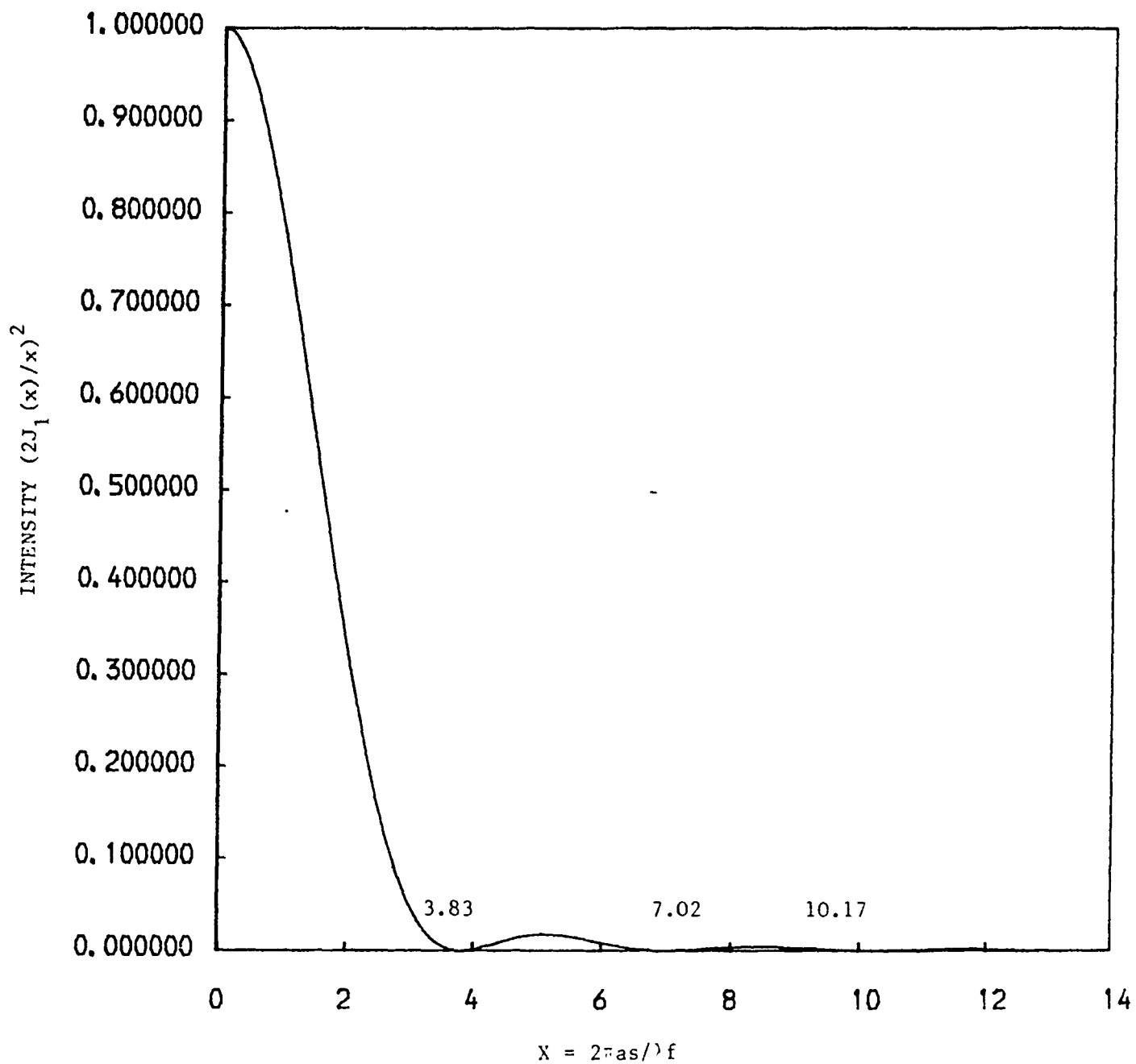


Fig. 2. Intensity distribution in the diffraction pattern of a circular disc or aperture.

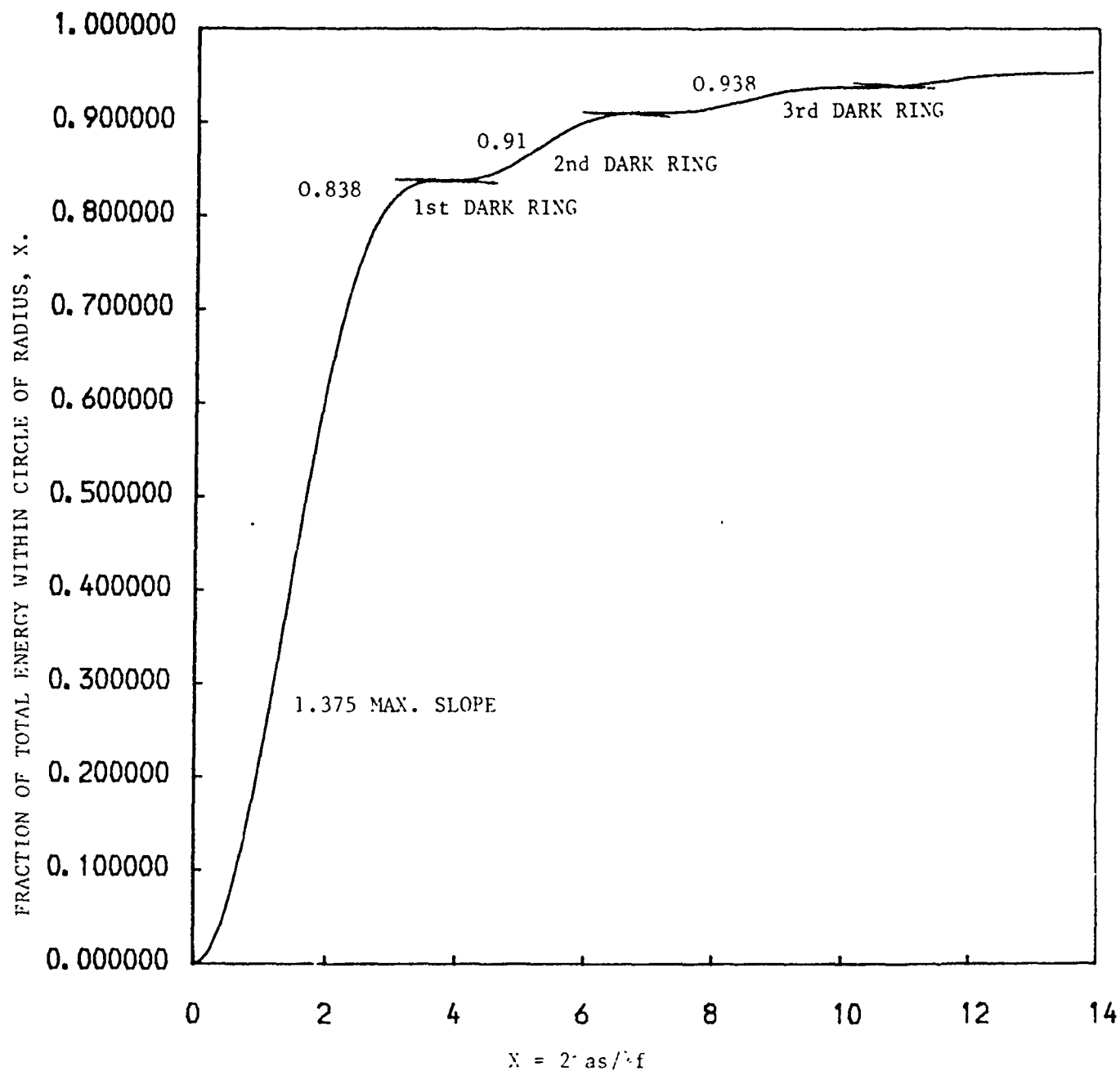


Fig. 3. Fraction of the diffracted energy contained within a circle of radius X . $1 - J_0^2(x) - J_1^2(x)$

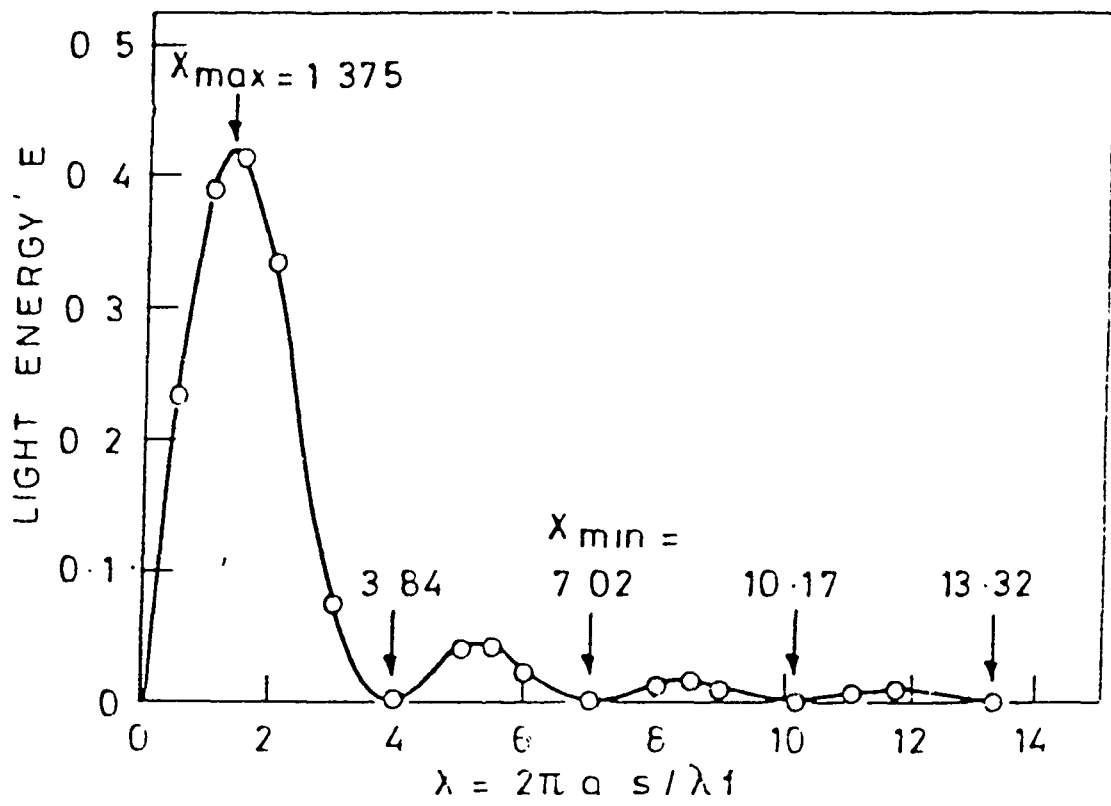


Fig. 4 Dimensionless diffracted light energy distribution.

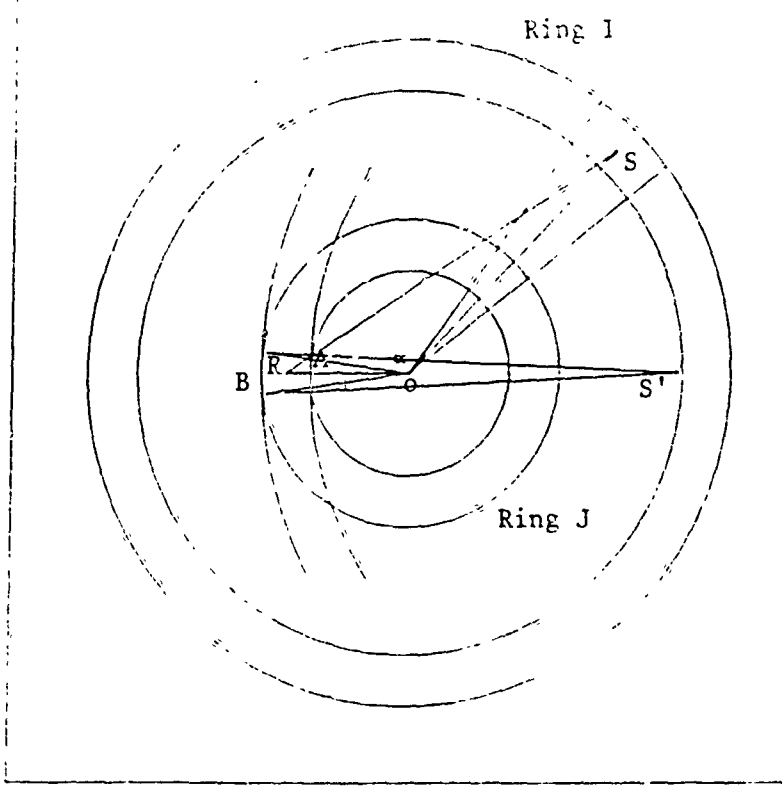


Fig. 5 A Typical integration step in the calculation procedure.

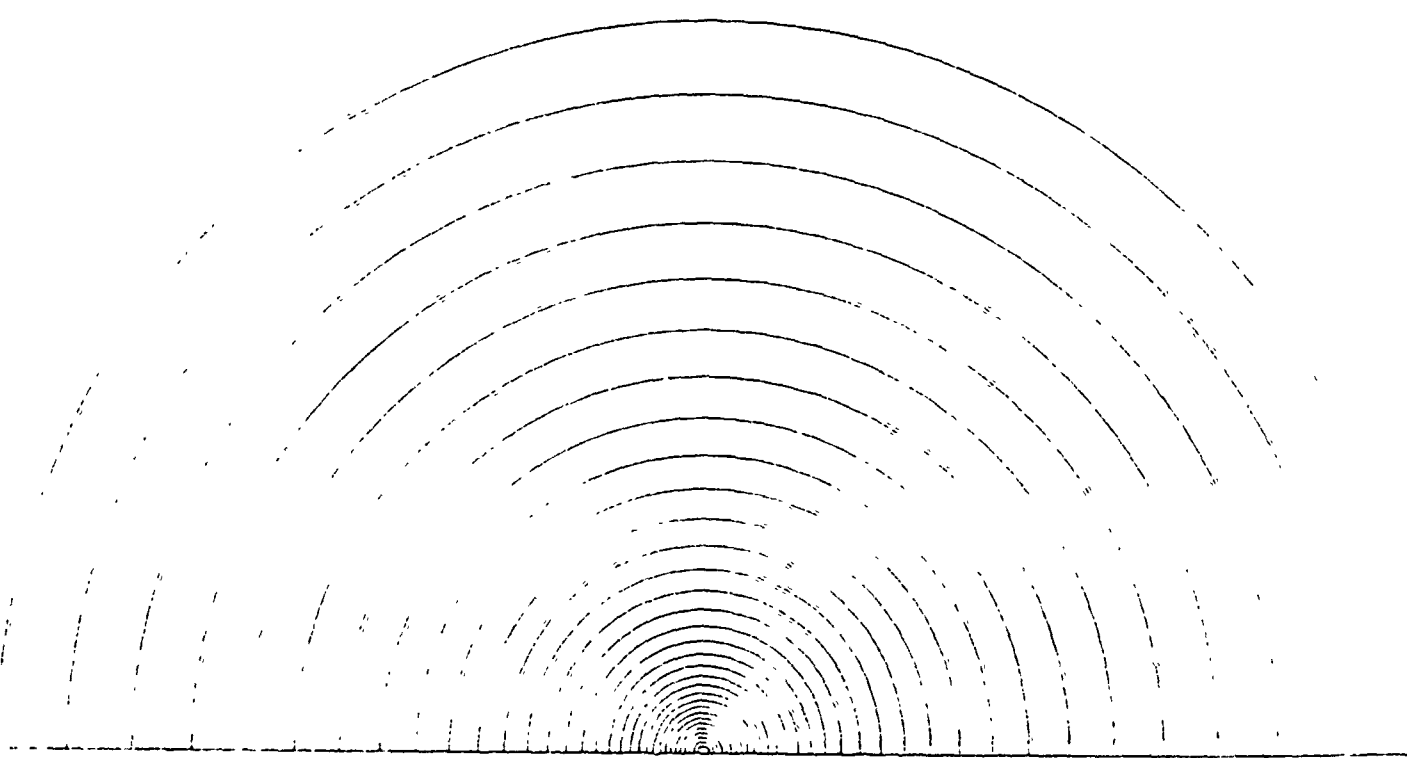
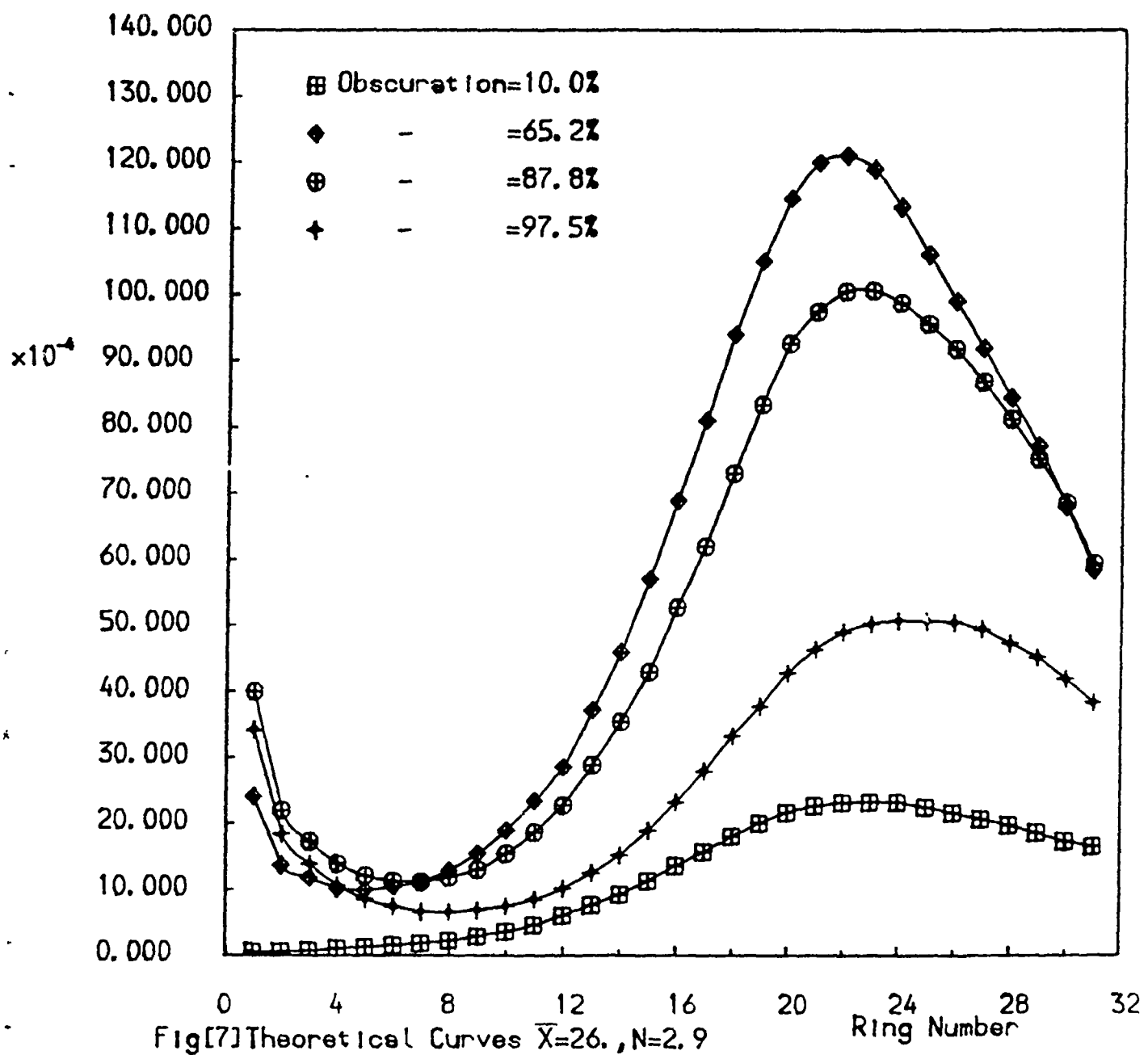
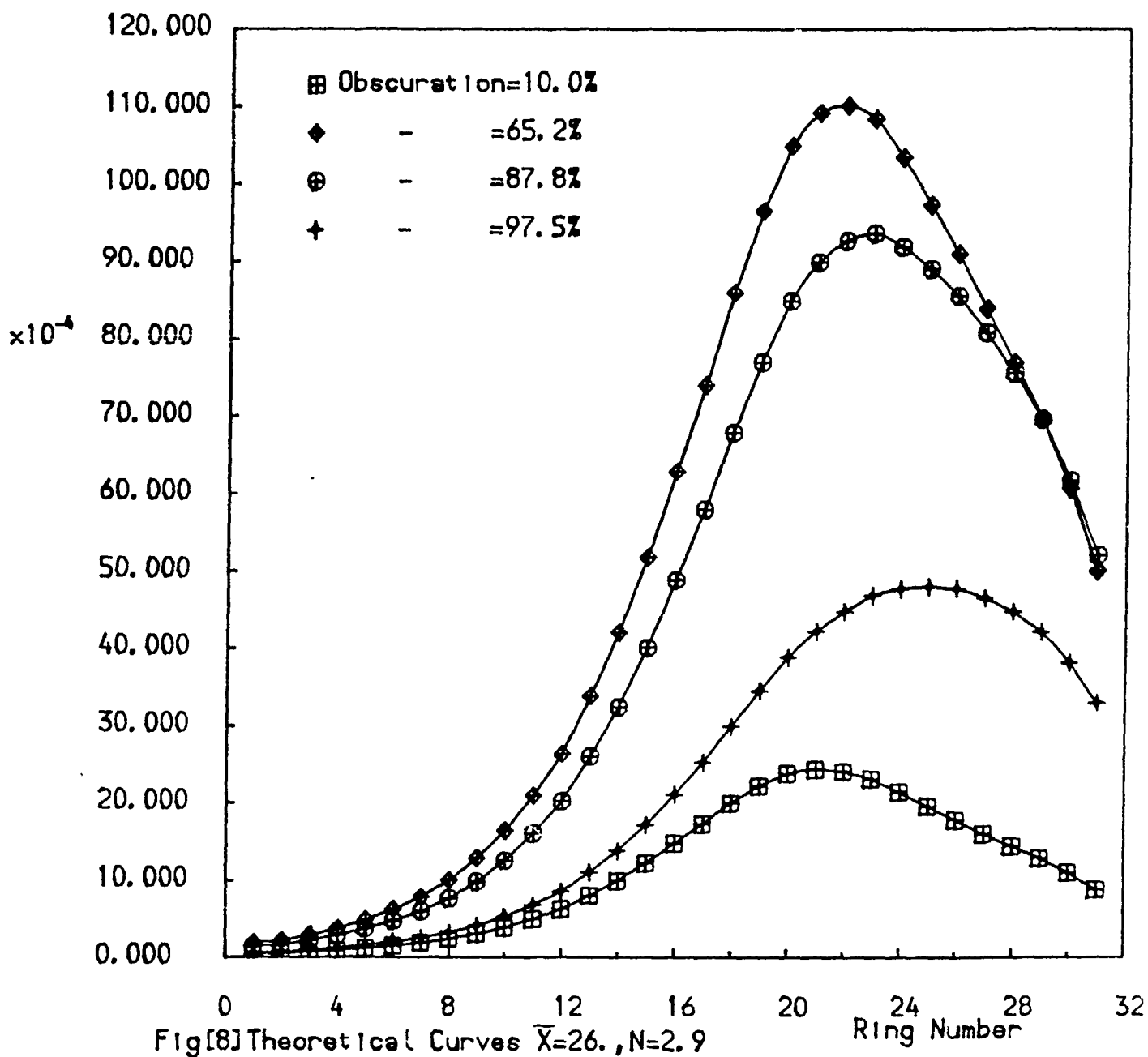


Fig. 6 Photodetector diode; Drawn to Scale

Energy Distributions



Energy Distributions



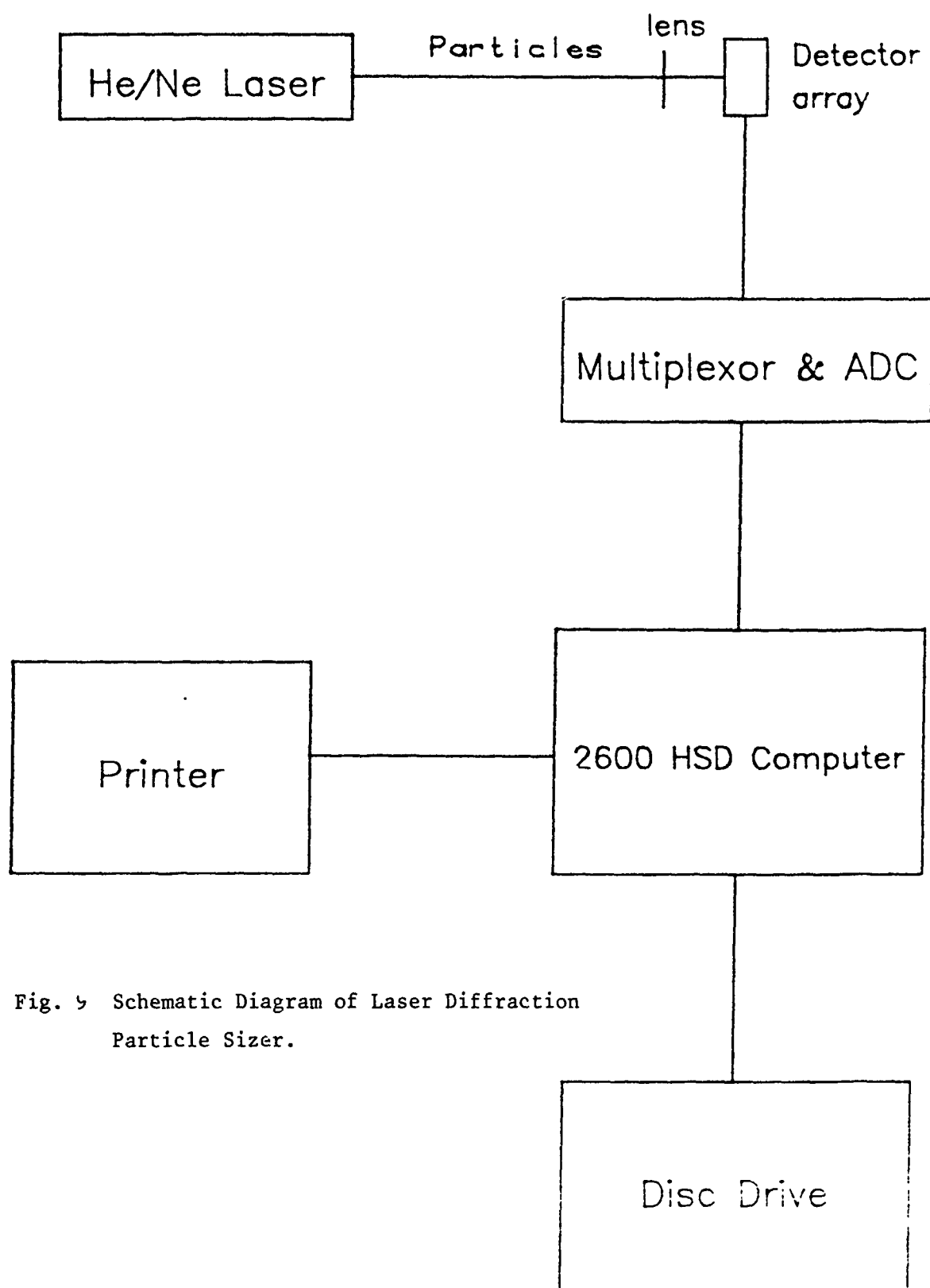


Fig. 5 Schematic Diagram of Laser Diffraction
Particle Sizer.

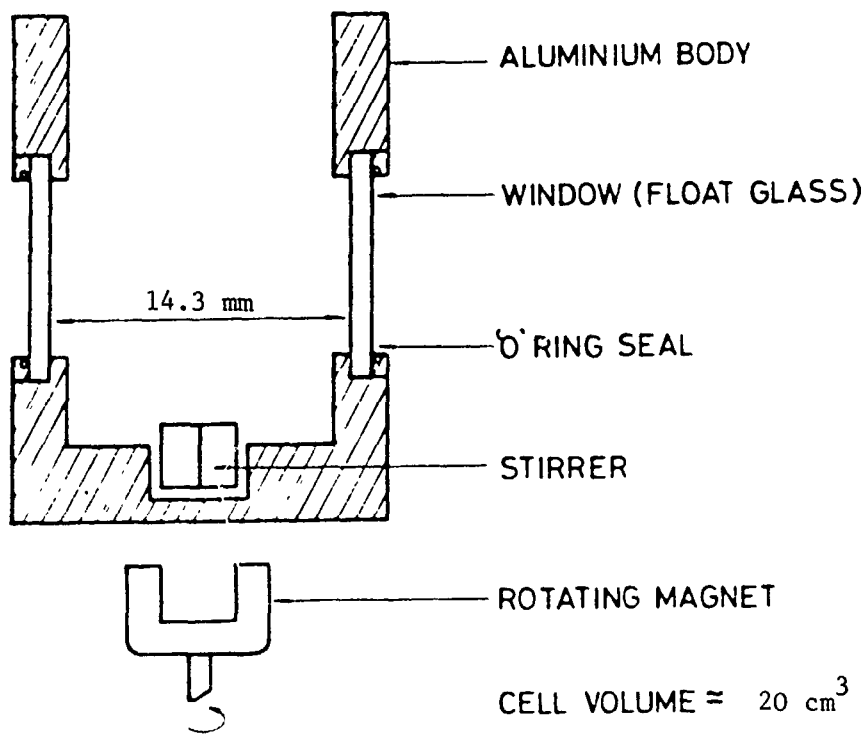
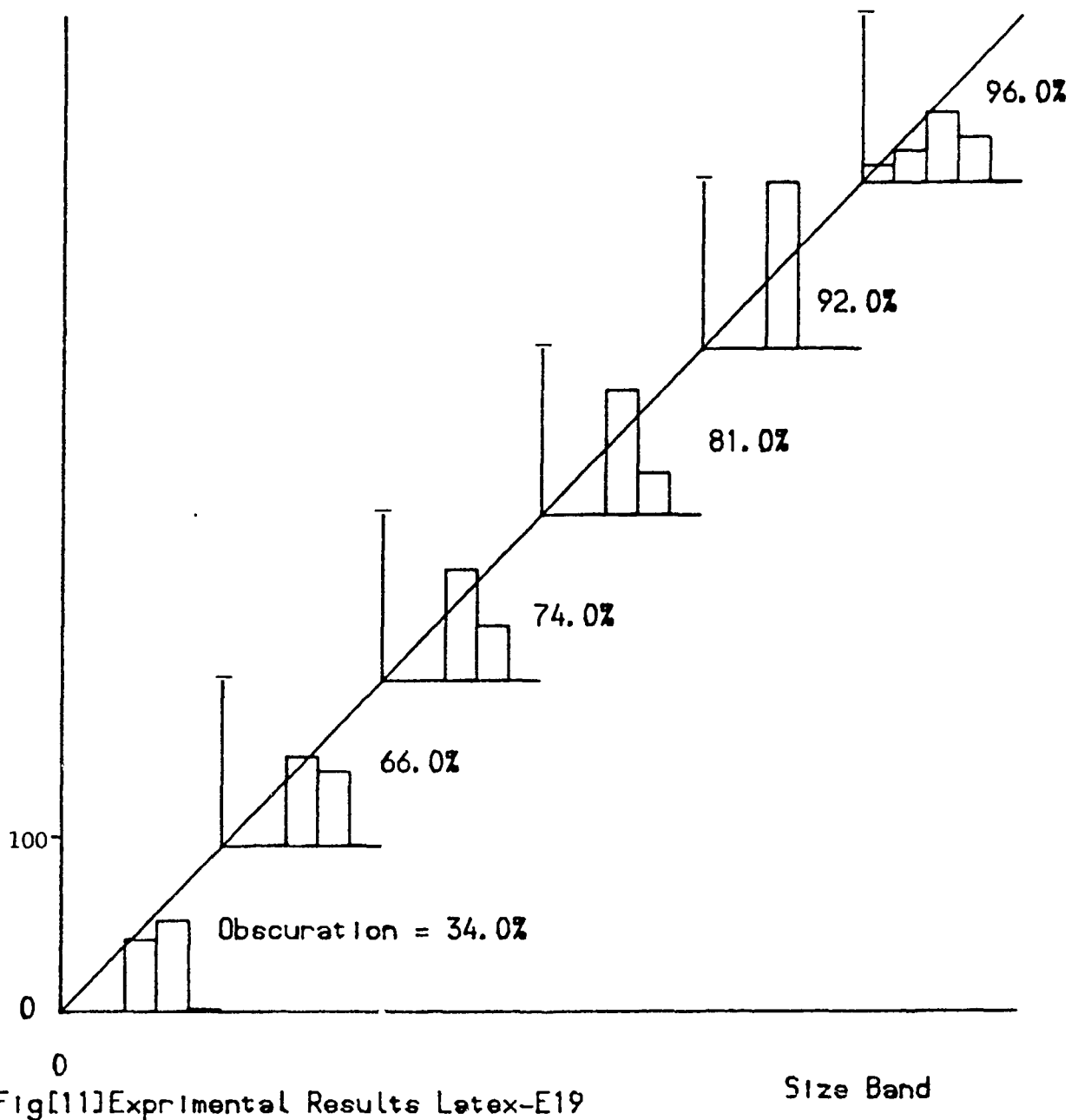


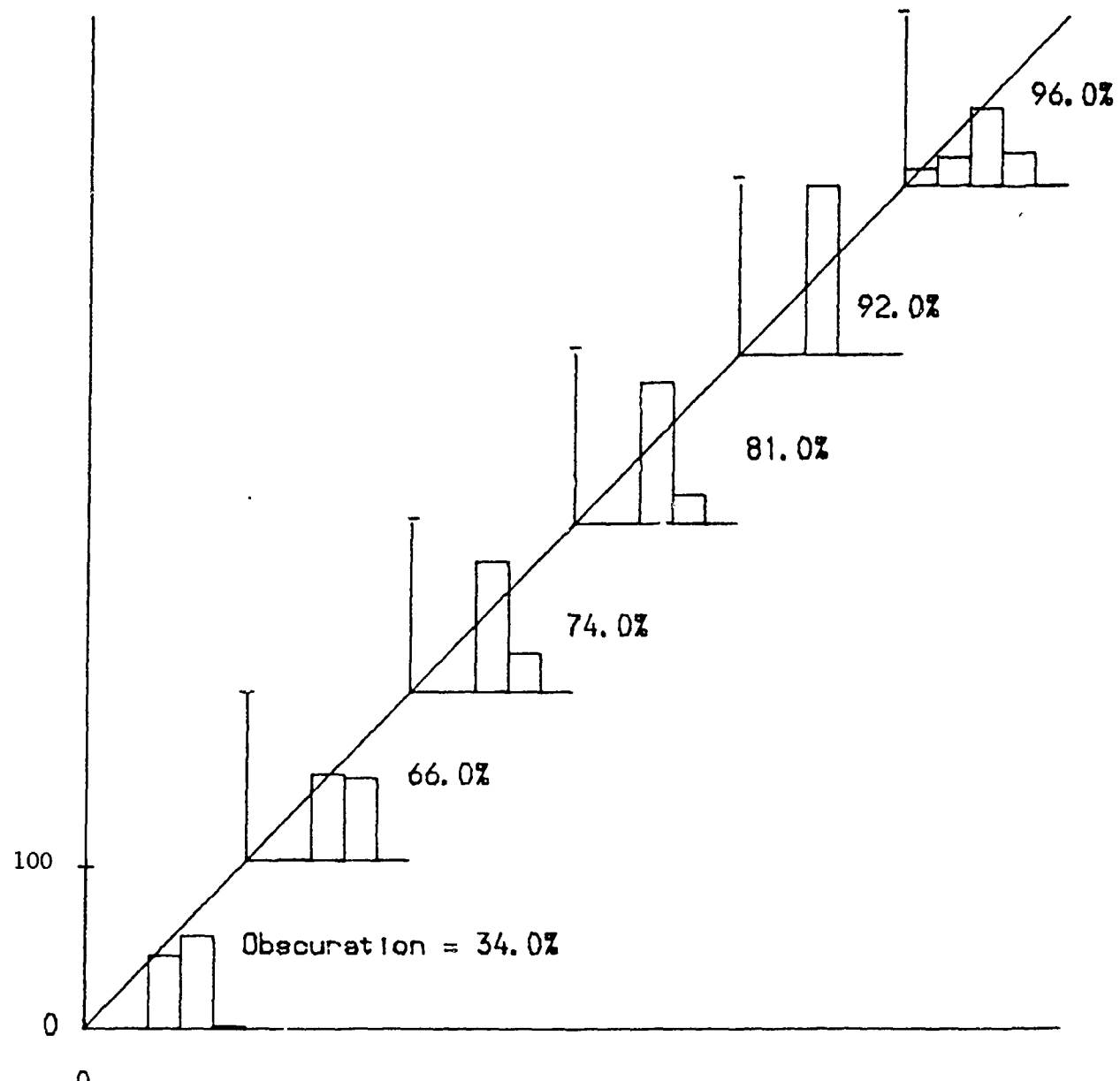
Fig. 10 Diagram of the cell used for solid particle size determination.

Percentage Particles In Size Band.



Fig[11] Experimental Results Latex-E19

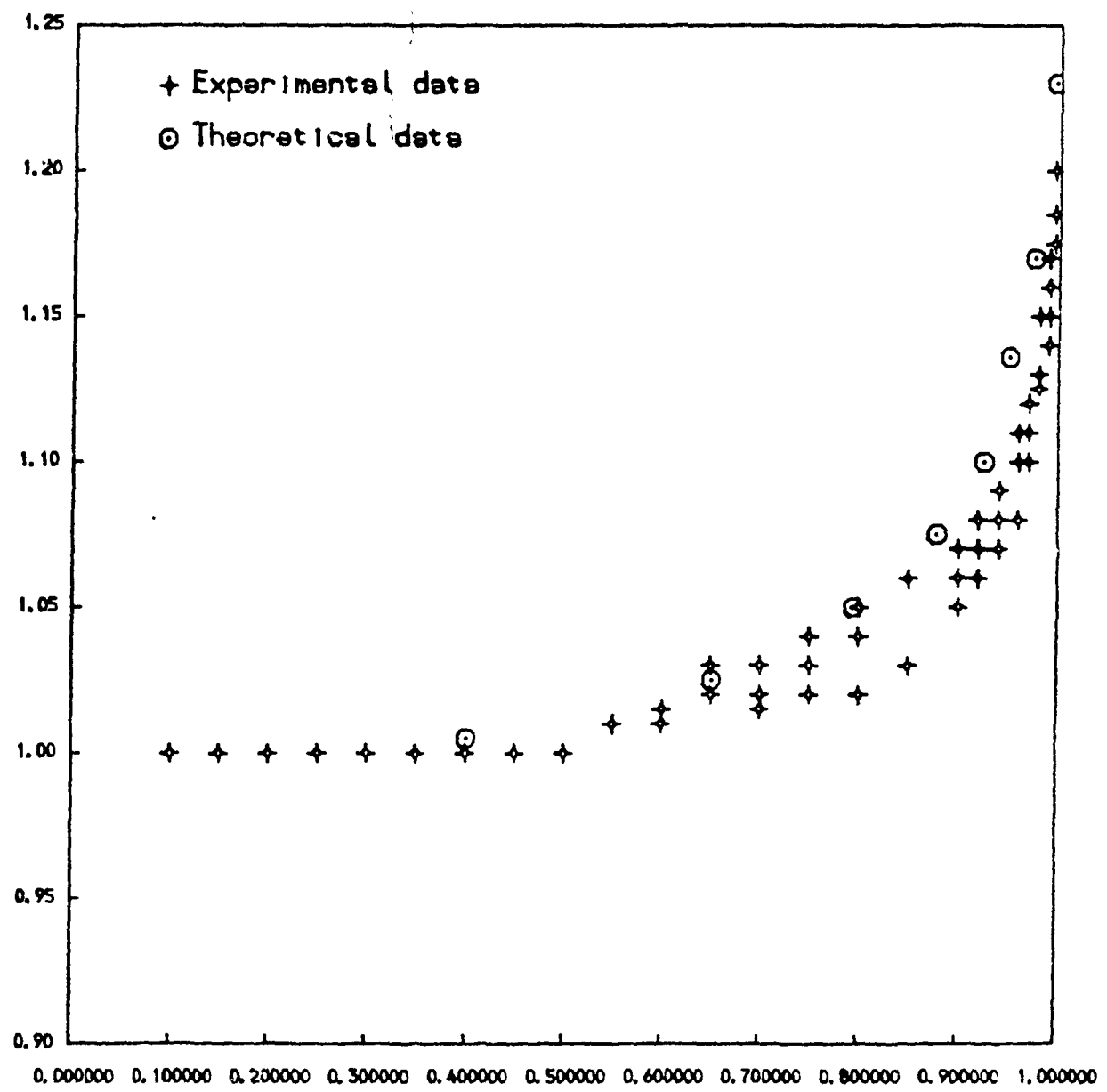
Percentage Particles In Size Band.



Fig[12] Theoretical Results Latex-E19

Size Band

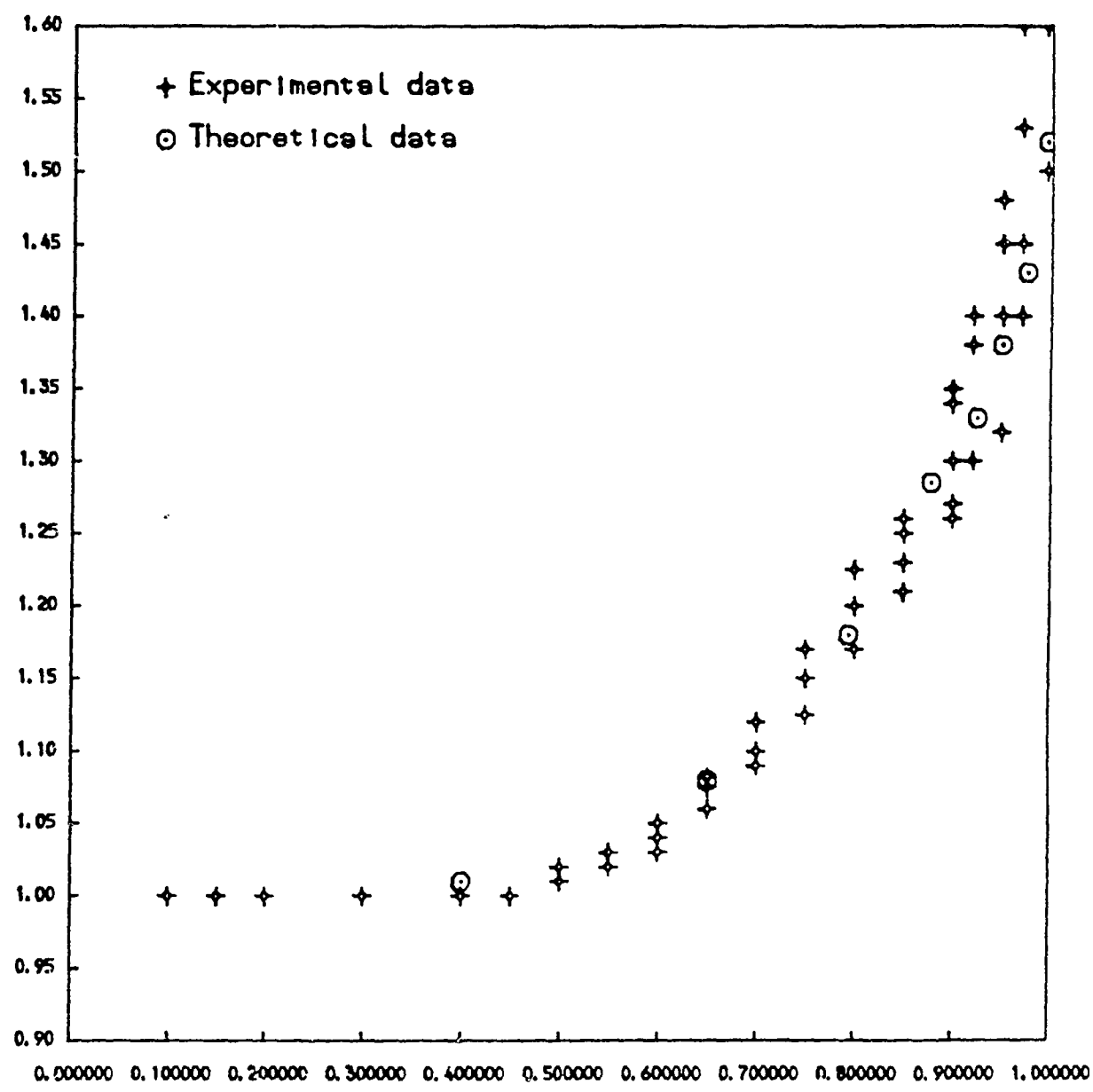
Correction Factor For \bar{X}



Fig[13]Cx Results for $\bar{X}=21.$, $N=2.9$

Obscuration

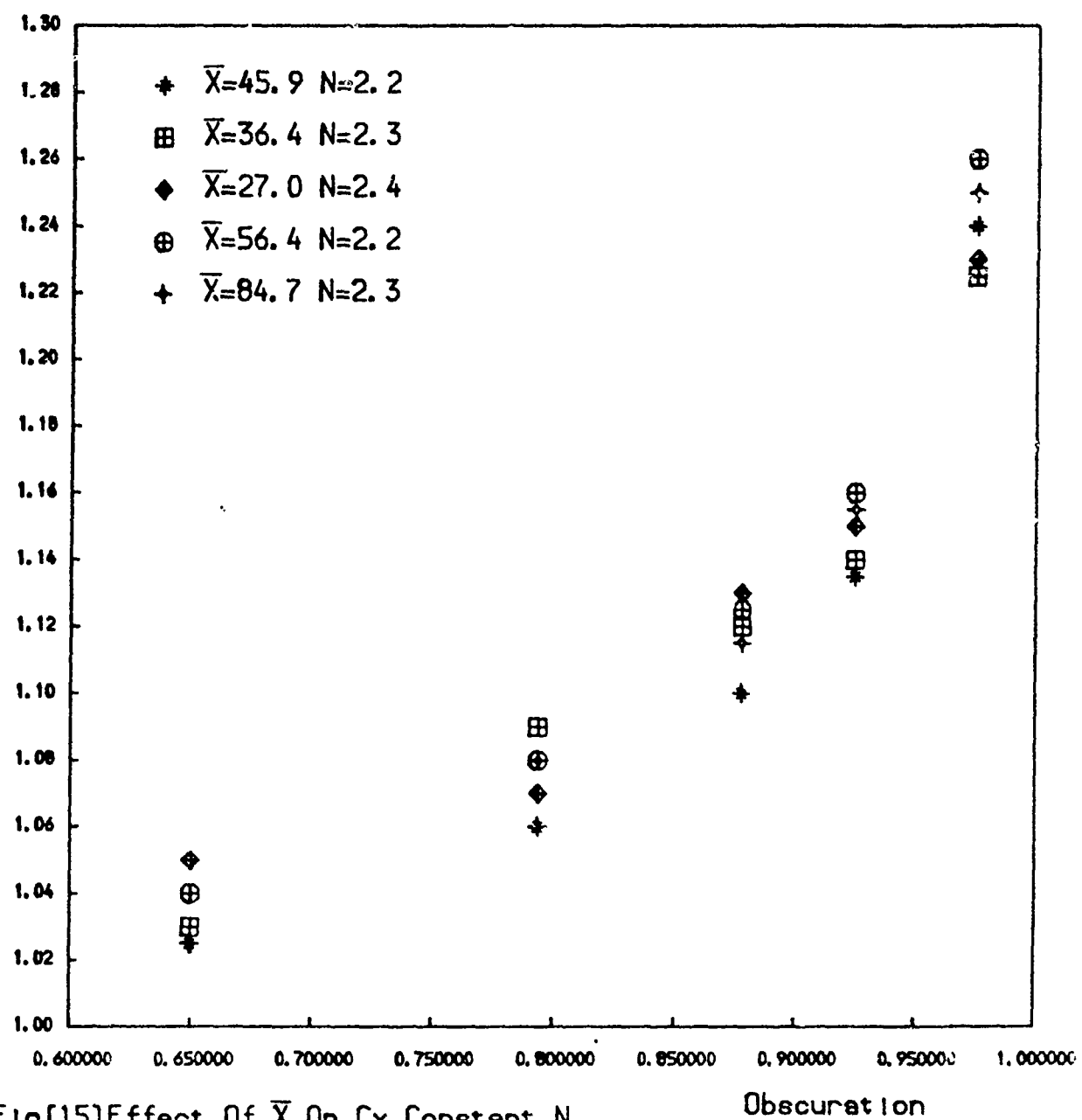
Correction Factor For N



Fig[14]Cn Results for $\bar{X}=21.$, $N=2.9$

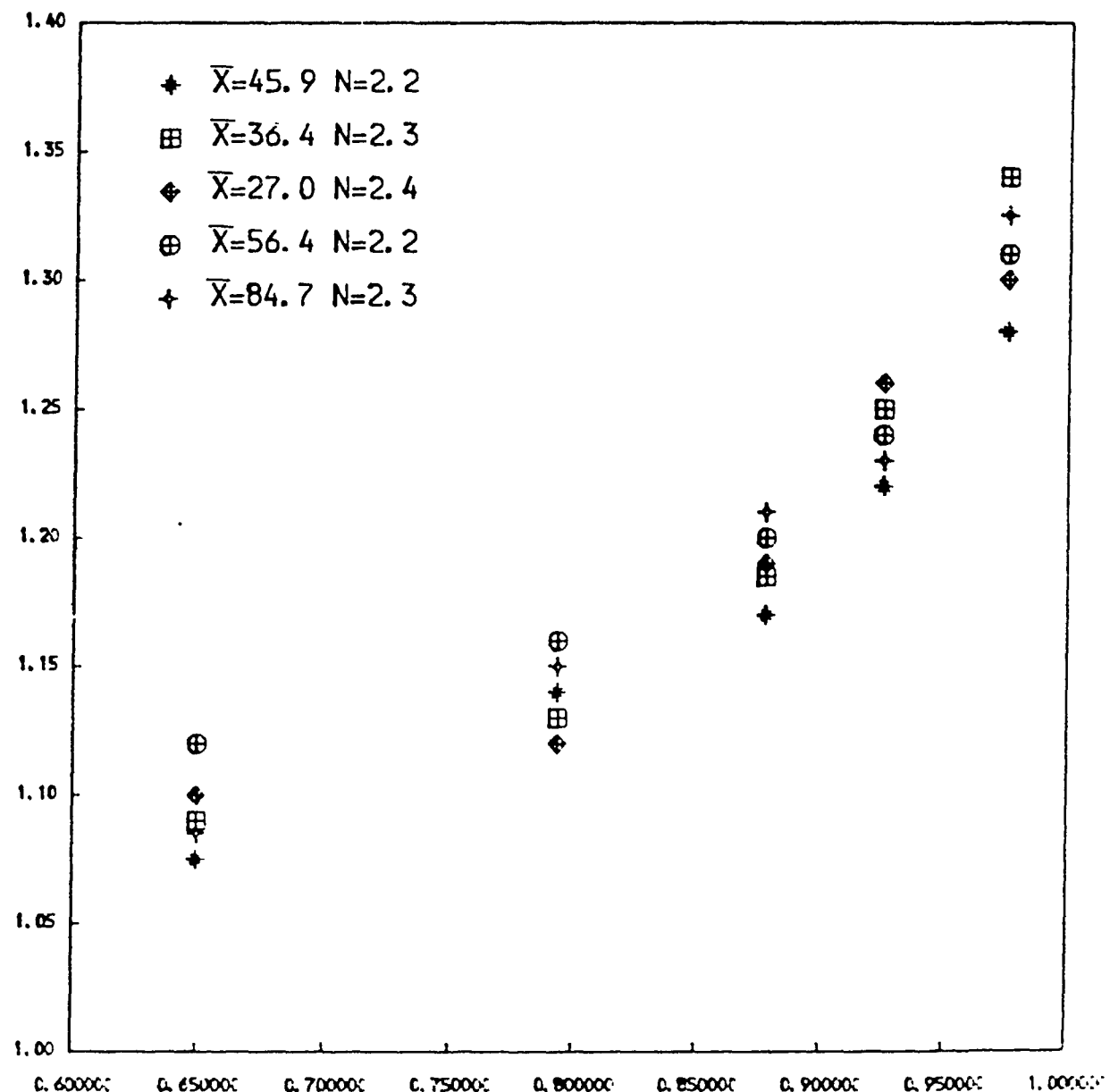
Obscuration

Correction Factor For \bar{X}



Fig[15] Effect Of \bar{X} On C_x , Constant N

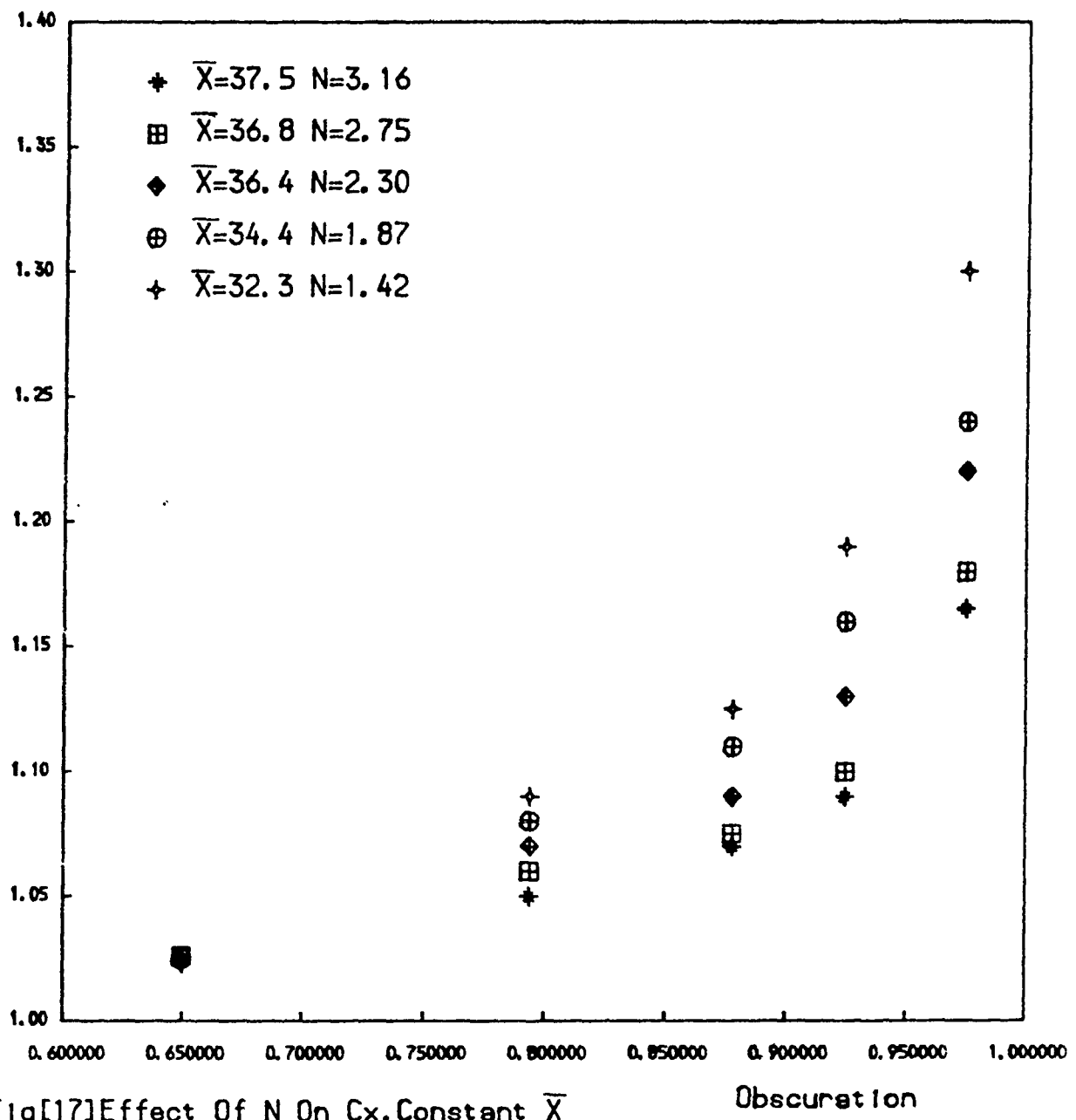
Correction Factor For N



Fig[16]Effect Of \bar{X} On C_n ,Constant N

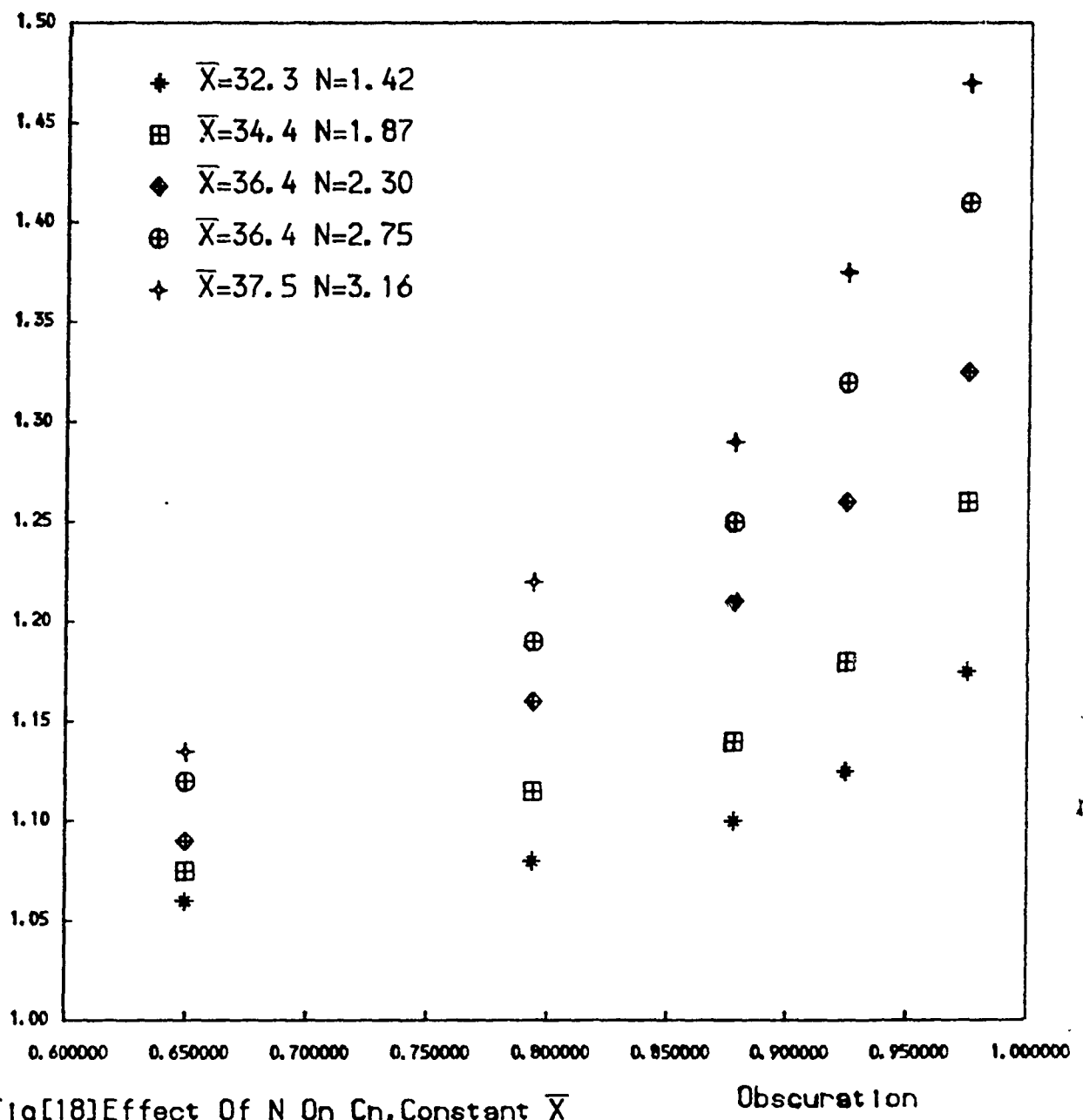
Obscuration

Correction Factor For \bar{X}



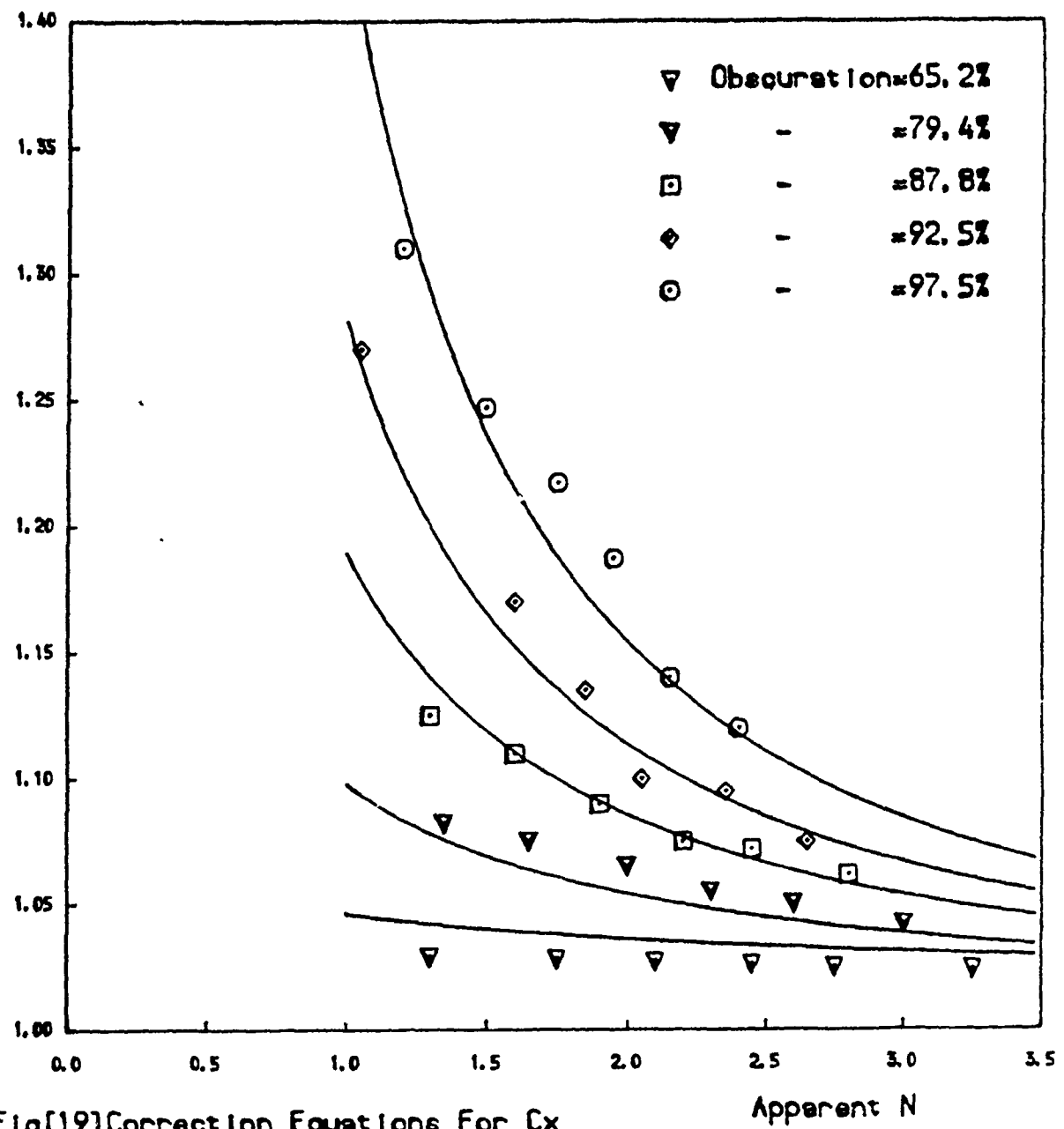
Fig[17]Effect Of N On Cx, Constant \bar{X}

Correction Factor For N



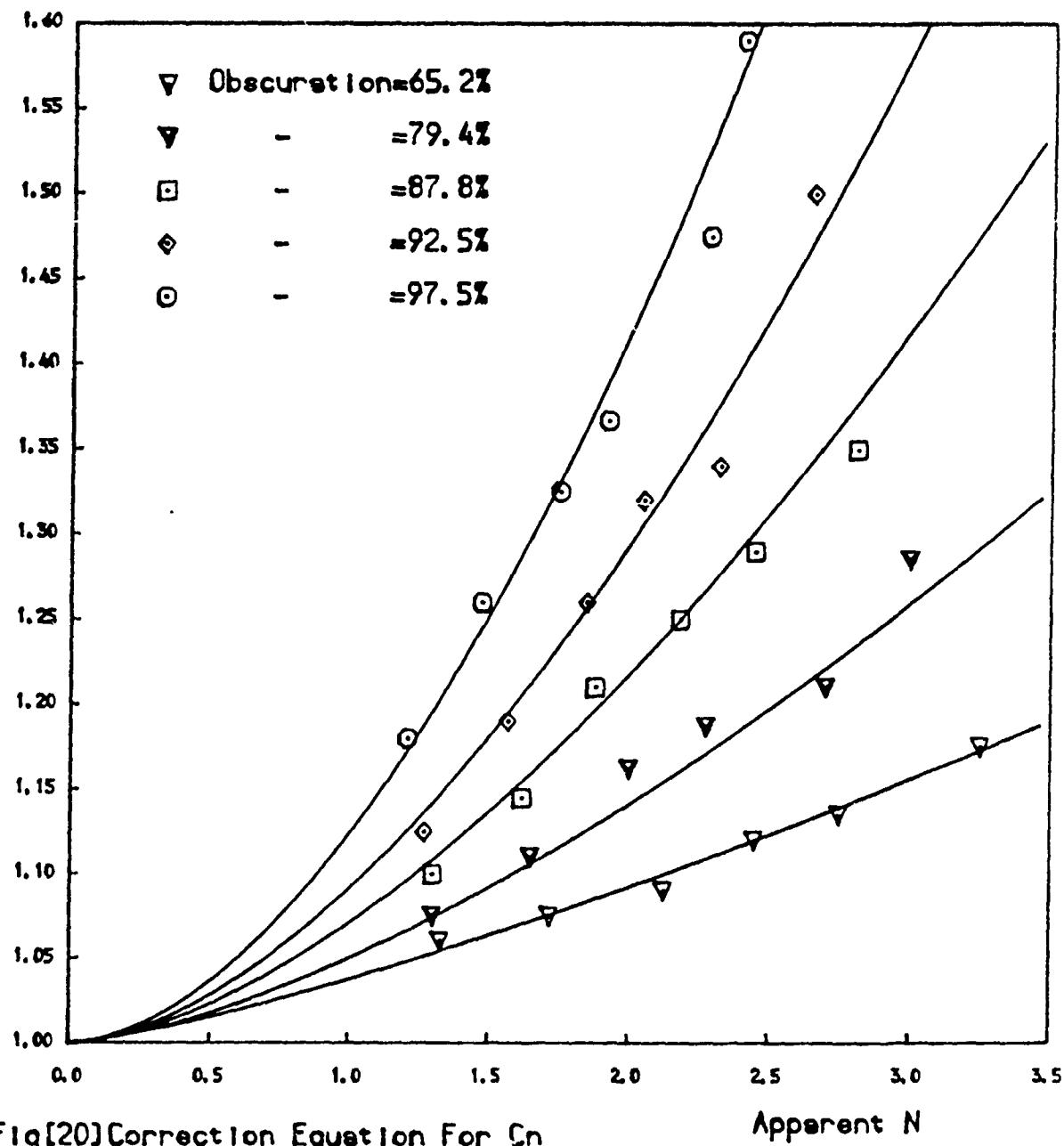
Fig[18] Effect Of N On C_n , Constant \bar{X}

Correction Factor For \bar{X}



Fig[19] Correction Equations For C_x

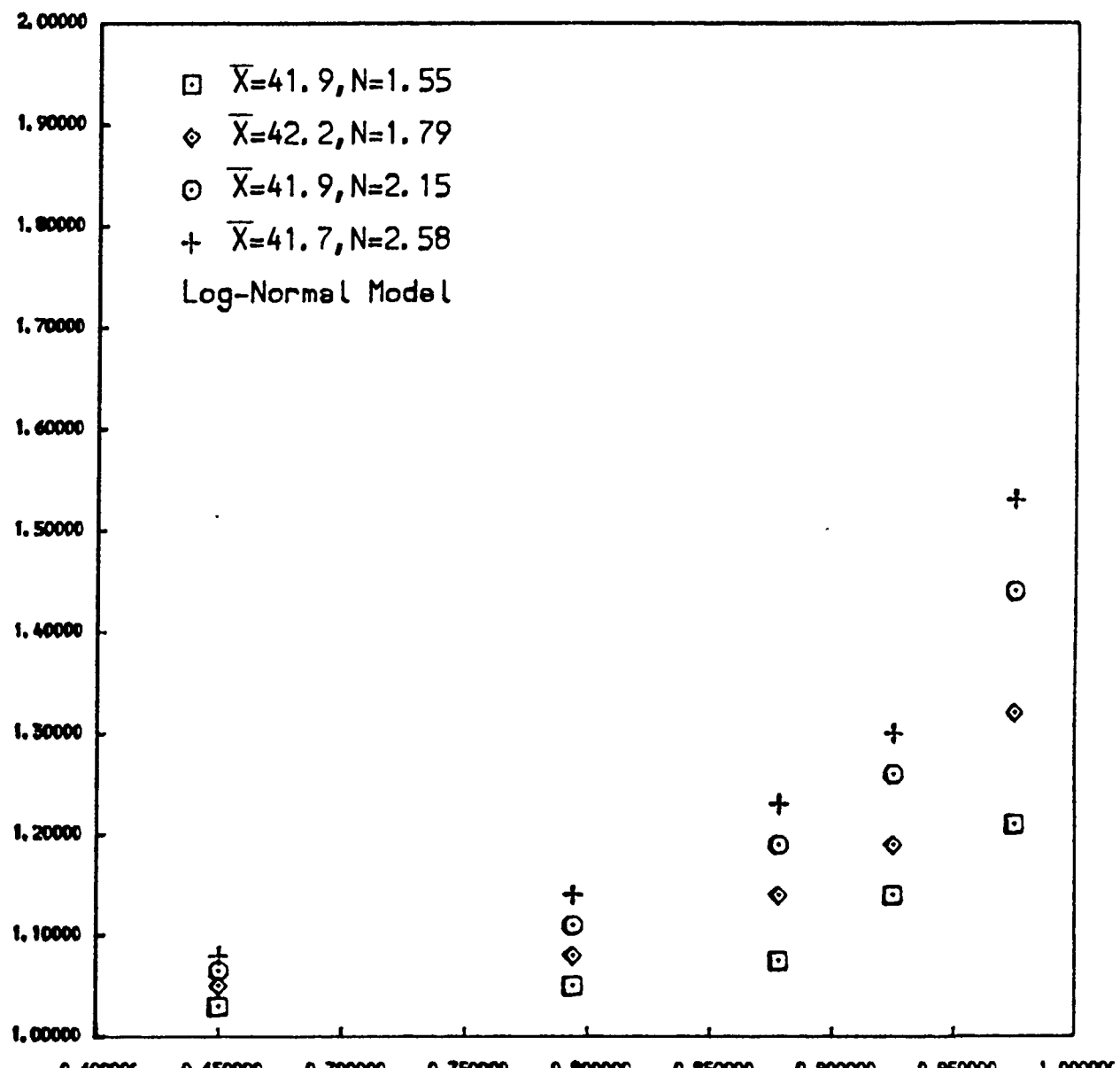
Correction Factor For N



Fig[20] Correction Equation For C_N

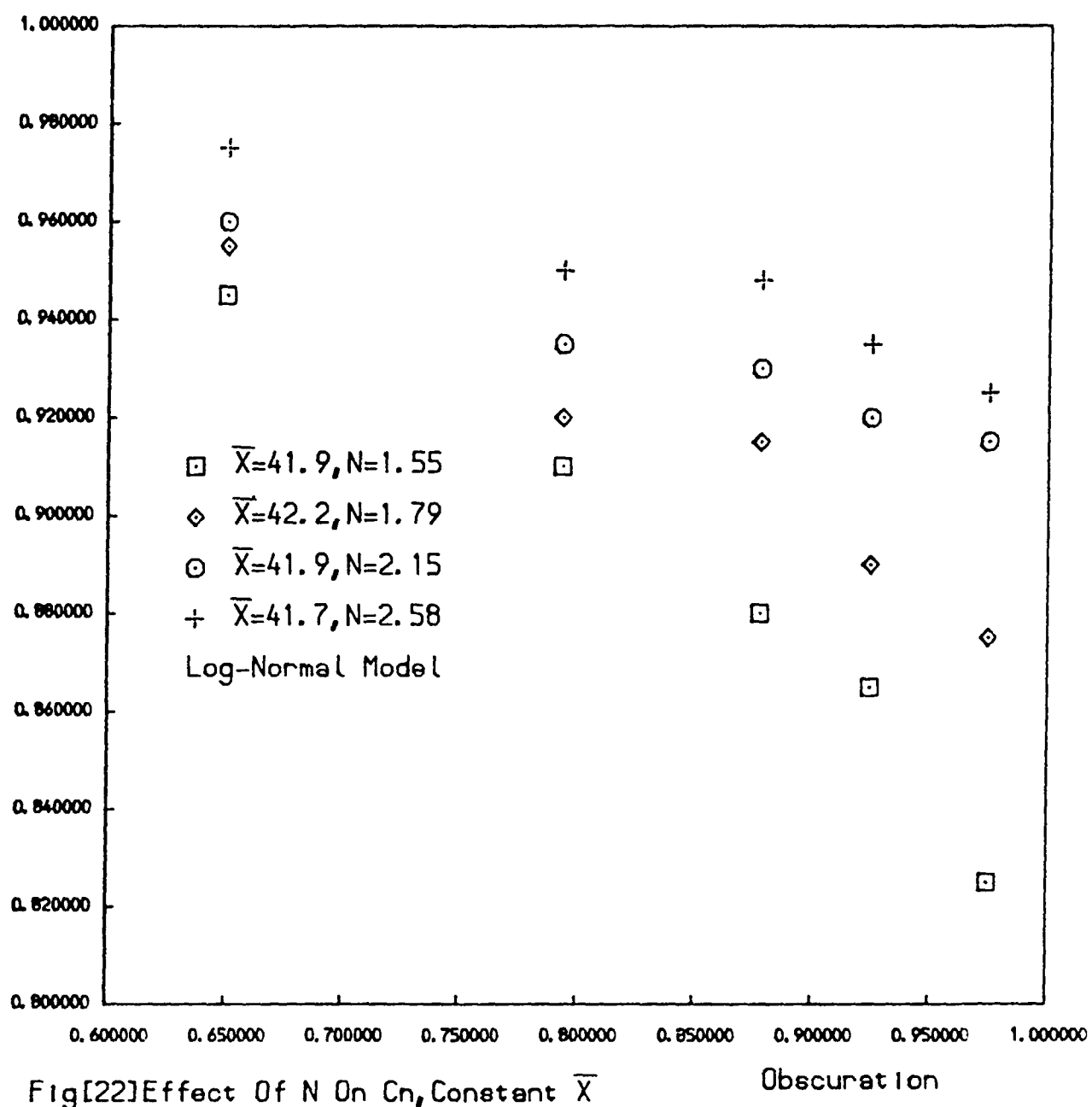
Apparent N

Correction Factor For \bar{X}



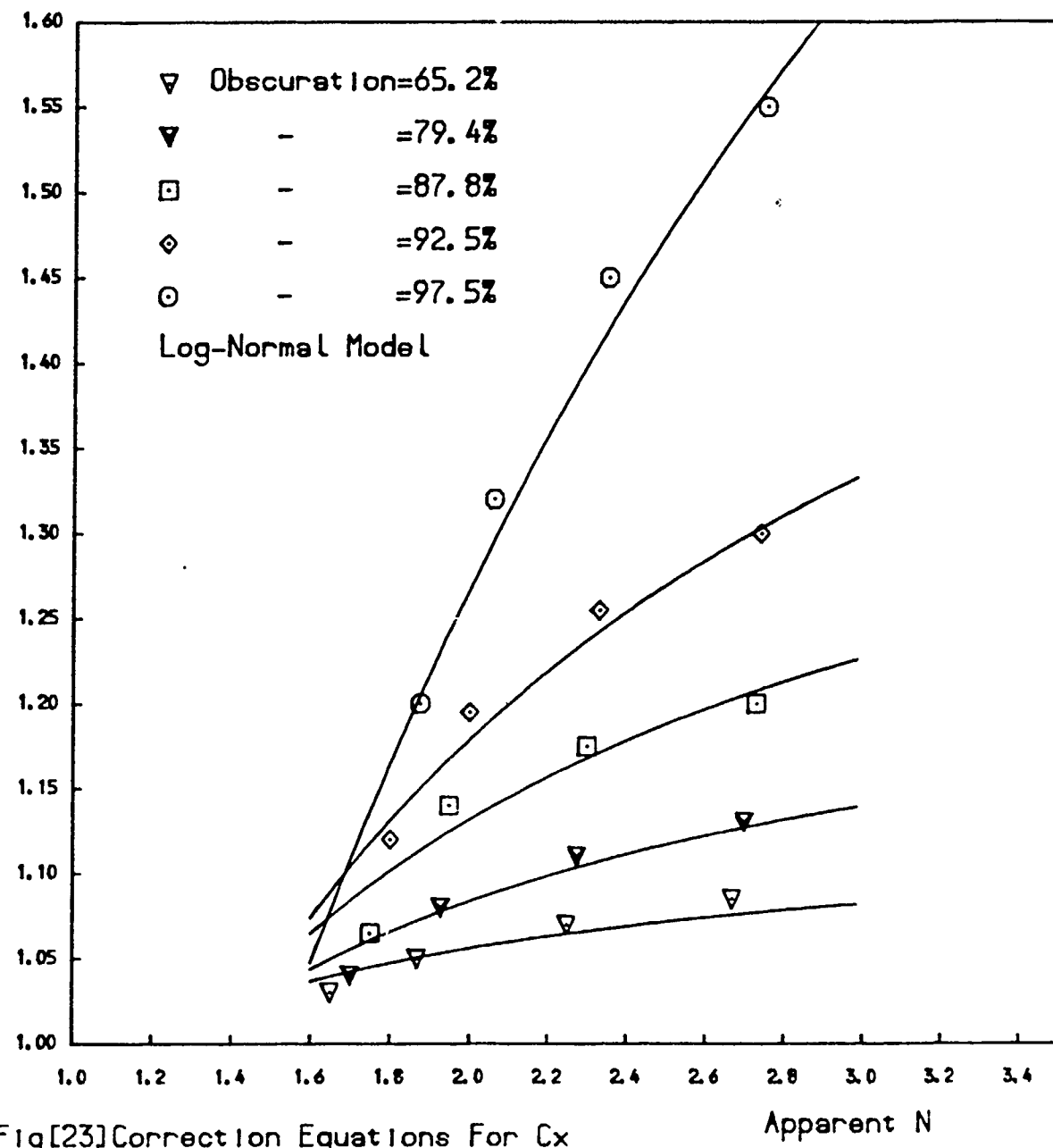
Fig[21] Effect Of N On C_x , Constant \bar{X}

Correction Factor For N



Fig[22] Effect Of N On Cn, Constant \bar{X}

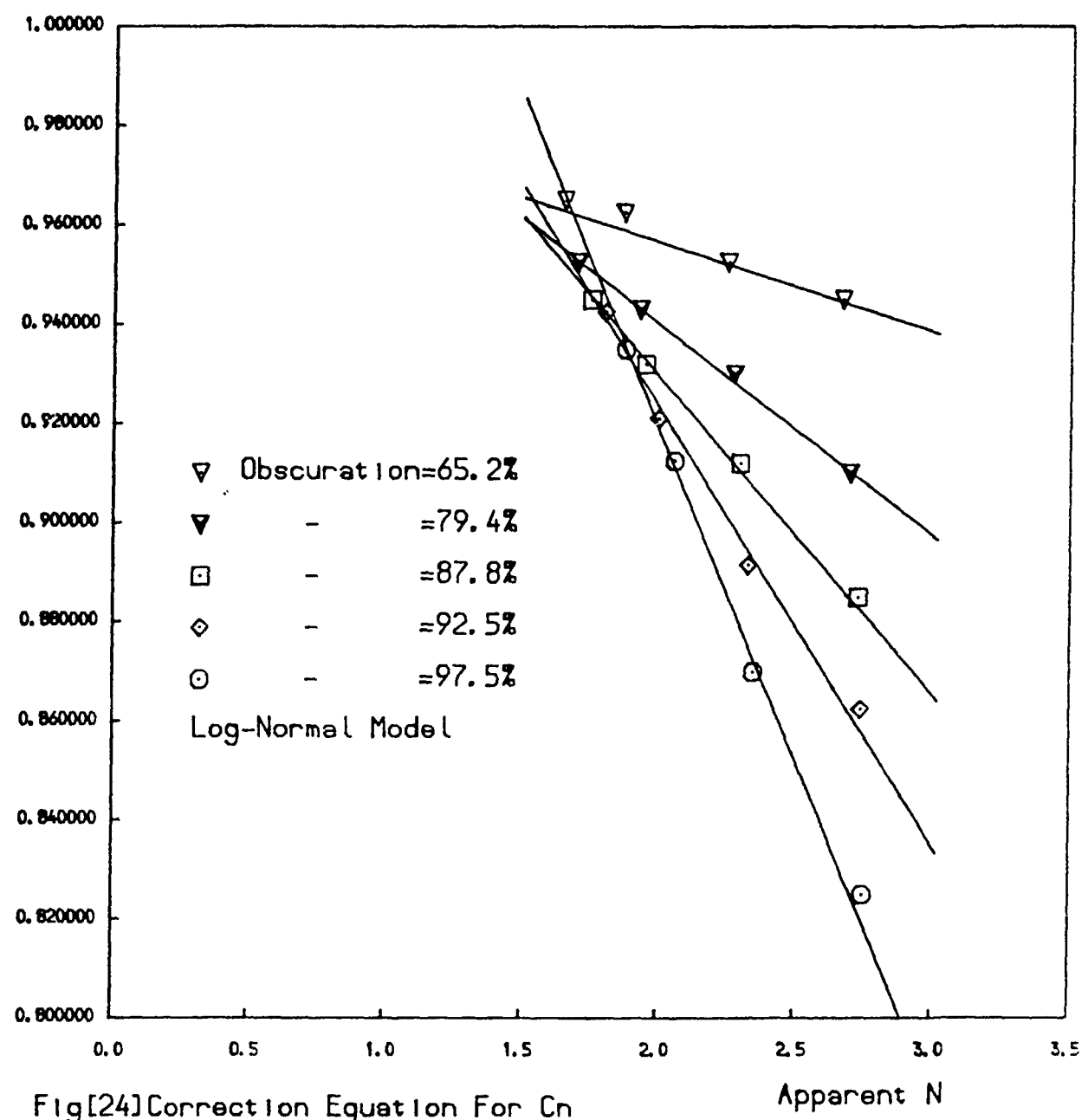
Correction Factor For \bar{X}



Fig[23] Correction Equations For \bar{X}

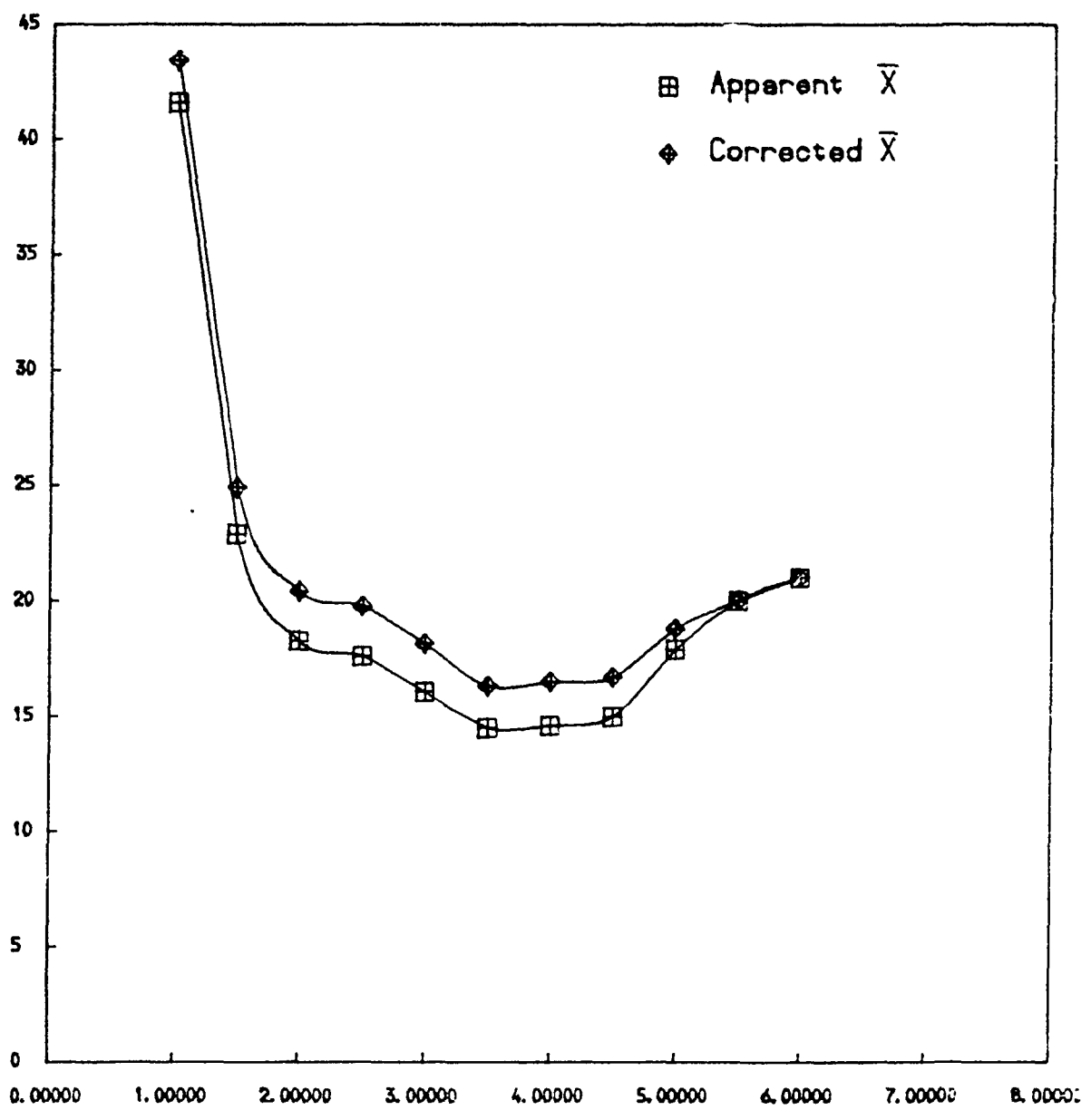
Apparent N

Correction Factor For N



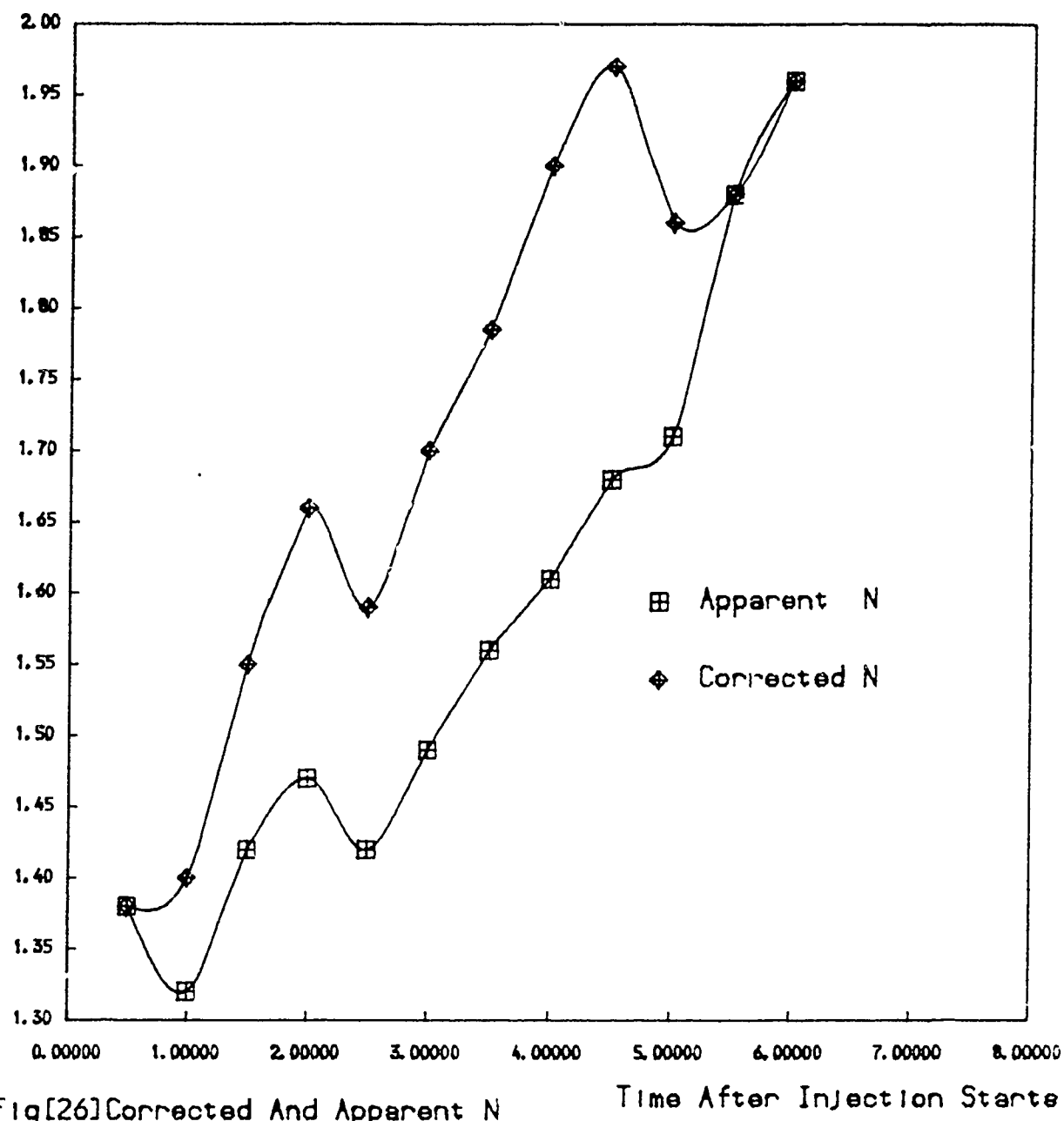
Fig[24] Correction Equation For C_n

Rosin-Rammler Mean Size



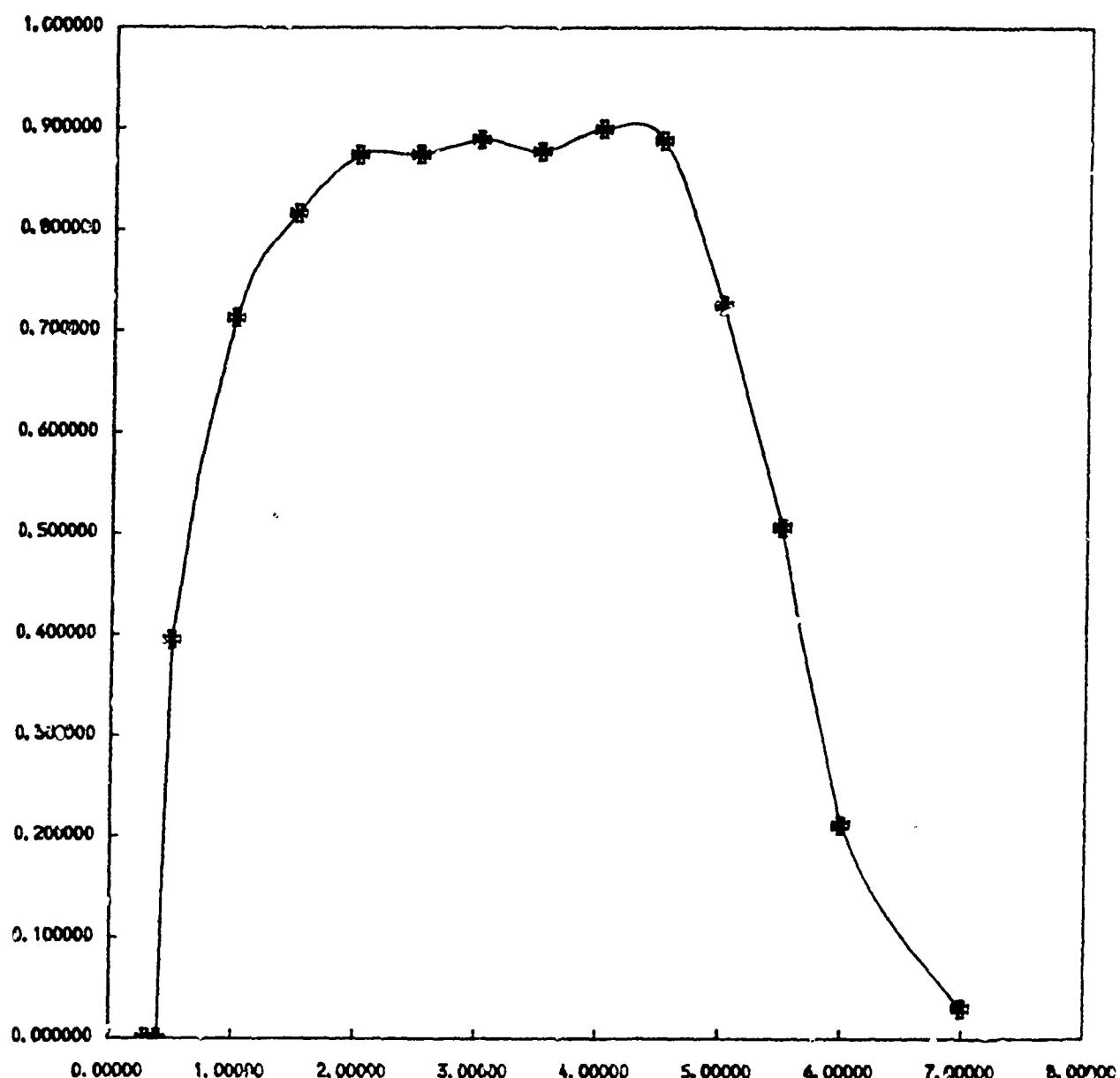
Fig[25] Corrected And Apparent \bar{X} Time After Injection Starts ms

Rosin-Rammler Exponent



Fig[26] Corrected And Apparent N

Fraction Of Light Obscured



Fig[27] Time-Obscuration Plot

Time After Injection Starts ms